UNIVERSITY OF RIJEKA
FACULTY OF ENGINEERING

Toni Holjević

Experimental-numerical analysis of microplastic particle transport in water

DOCTORAL THESIS

Rijeka, 2025.

UNIVERSITY OF RIJEKA
FACULTY OF ENGINEERING

Toni Holjević

Experimental-numerical analysis of microplastic particle transport in water

DOCTORAL THESIS

Supervisor: Prof. dr. sc. Siniša Družeta
Co-supervisor: Prof. dr. sc. Vanja Travaš

Rijeka, 2025.

SVEUČILIŠTE U RIJECI
TEHNIČKI FAKULTET

Toni Holjević

Eksperimentalno-numerička analiza pronosa čestica mikroplastike u vodi

DOKTORSKA DISERTACIJA

Mentor: prof. dr. sc. Siniša Družeta
Komentor: prof. dr. sc. Vanja Travaš

Rijeka, 2025.

Doctoral dissertation Supervisor: prof. dr. sc. Siniša Družeta

Co-supervisor: prof. dr. sc. Vanja Travaš

The doctoral dissertation was defended on _____ at the University of Rijeka, Faculty of Engineering, Croatia, in front of the following Evaluation Committee:

ABSTRACT

Plastic pollution poses a growing threat to aquatic environments, with microplastic (MP) particles representing a significant challenge due to their endurance and potential ecological impact. This dissertation focuses on the experimental and numerical analysis of MP particle transport in water to complement our understanding of their behavior under varying hydrodynamic conditions.

This study combines experimental methods with numerical modeling to analyze the drag coefficients and transport mechanisms of MP particles of various shapes and sizes. Experiments were conducted using an experimental hydraulic channel to simulate steady and uniform water flow conditions. This setup enabled controlled conditions over hydrodynamic parameters, ensuring reproducibility of MP transport analysis. MP particles were fabricated using a high-accuracy 3D printer to ensure consistent geometry, while their trajectories were recorded using high-resolution video equipment. Custom Python scripts were used to process the captured video material, enabling detailed analysis of particle motion, velocity, and acceleration. Bézier curves were used to approximate MP trajectories, providing a mathematical method for smoothing and analyzing paths based on control points. This method offers high precision in representing complex motion patterns and accurate characterization of particle behavior. A new shape parameterization method was also proposed, utilizing geometric factors such as sphericity and circularity to characterize MP particles. Based on these findings, a new drag coefficient model was developed, presenting improved accuracy in quantifying the resistance of MP particles in a fluid stream under varying Reynolds numbers.

The experimental results were used for validation of numerical model that was created in OpenFOAM software. Numerical model was developed to match experimental conditions, specifically hydraulic channel geometry, flow characteristics, and particle motion recorded during experiments. Boundary conditions, including inlet velocity and outlet pressure, were defined to ensure consistency with experimental parameters, and a structured numerical mesh was created

to optimize computational efficiency. Particle motion was simulated in the numerical model and compared with experimental results. A correction to the numerical model was proposed, which accounted for deviations observed in initial simulations in comparison with recorded data.

Key scientific contributions include the development of a calibrated drag coefficient model, a hybrid experimental-numerical methodology for analyzing MP transport, and advancements in the use of photogrammetry, Python-based algorithms, and numerical model corrections for capturing and analyzing particle trajectories. This research presents new findings and methods in MP transport dynamics and behaviour predictions in aquatic systems. Final results aim to support mitigation strategies for MP pollution and contribute to the broader effort to preserve aquatic ecosystems.

Keywords: microplastics, drag coefficient, hydrodynamics, experimental analysis, numerical modeling, shape parameterization, drag model, hydraulic channel, boundary conditions, particle motion simulation

Sažetak

Zagađenje plastikom predstavlja sve veći problem za vodene ekosustave, pri čemu čestice mikroplastike (MP) predstavljaju značajan izazov zbog svoje otpornosti i potencijalnog ekološkog utjecaja. Ova disertacija usredotočuje se na eksperimentalnu i numeričku analizu prijenosa čestica MP u vodi kako bi se dopunilo naše razumijevanje njihovog ponašanja u različitim hidrodinamičkim uvjetima.

Studija kombinira eksperimentalne metode s numeričkim modeliranjem za analizu koeficijenta otpora i mehanizama prijenosa čestica MP različitih oblika i veličina. Eksperimenti su provedeni u eksperimentalnom hidrauličkom kanalu koji simulira laminaran protok vode. Ovaj sustav omogućio je preciznu kontrolu hidrodinamičkih parametara, osiguravajući ponovljive uvjete za analizu prijenosa MP. Čestice MP su izrađene visoko preciznim 3D printerom kako bi se osigurala konzistentna geometrija, dok su njihove putanje snimljene visokorezolucijskom videoopremom. Prilagođena Python skripta korištena je za obradu snimljenih materijala, omogućujući detaljnu analizu gibanja čestica, brzine i ubrzanja. Bézierove krivulje korištene su za aproksimaciju putanja MP, pružajući matematičku metodu za analizu putanja na temelju kontrolnih točaka. Ova metoda nudi visoku preciznost u prikazu složenih obrazaca gibanja i točno karakteriziranje ponašanja čestica. Također je predložen novi način parametrijske analize oblika, koristeći geometrijske indekse kao što su sferičnosti i cirkularnost za parametrizaciju čestica MP. Na temelju ovih rezultata razvijen je novi model koeficijenta otpora oblika, koji omogućuje veću preciznost u kvantificiranju otpora čestica MP u struji tekućine pri različitim Reynoldsovim brojevima.

Eksperimentalni rezultati korišteni su za validaciju numeričkog modela izrađenog u OpenFOAM softveru. Numerički model razvijen je u skladu s eksperimentalnim uvjetima, uključujući geometriju hidrauličkog kanala, karakteristike protoka i gibanje čestica zabilježeno tijekom eksperimenata. Definirani su rubni uvjeti, uključujući ulaznu brzinu i izlazni tlak, kako bi se osigurala konzistencija s eksperimentalnim parametrima, a konstruirana je strukturirana numer-

ička mreža radi optimizacije računalne učinkovitosti. Gibanje čestica simulirano je u numeričkom modelu i uspoređeno s eksperimentalnim rezultatima. Predložena je korekcija numeričkog modela koja je uzela u obzir odstupanja uočenih u početnim simulacijama u usporedbi s prikupljenim podacima. To je rezultiralo boljim usklađivanjem s eksperimentalnim podacima.

Ključni znanstveni doprinosi uključuju razvoj kalibriranog modela koeficijenta otpora, hibridnu eksperimentalno-numeričku metodologiju za analizu prijenosa MP, te napredak u primjeni fotogrametrije, Python algoritama i korekcija numeričkog modela za bilježenje i analizu putanja čestica. Ovo istraživanje predstavlja nove rezultate i metode u dinamici prijenosa MP i predviđanju njihovog ponašanja u vodenim sustavima. Konačni rezultati imaju za cilj podržati strategije ublažavanja onečišćenja MP i pridonijeti širem naporu očuvanja vodenih ekosustava.

Ključne riječi: mikroplastika, koeficijent otpora, hidrodinamika, eksperimentalna analiza, numeričko modeliranje, parametrijska analiza oblika, model koeficijenta otpora, hidraulički kanal, rubni uvjeti, simulacija gibanja čestica

Contents

1 Introduction

1.1 Motivation

Plastic production has become an fundamental component of modern society, with a wide range of different applications in various industries such as retail, construction, health care, automotive and packaging. Some of the key plastics advantages are their versatility, durability and affordability. Polymers, which are big molecules made up of repeated subunits, are the building blocks for synthetic materials like plastics. These components are primarily derived from crude oil and natural gas, which are petrochemical sources. The majority of plastics are therefore quite resilient and can last for hundreds of years in the environment. Due of its endurance, plastic waste has the potential to build up in natural ecosystems and cause long-term issues. According to the Organization for Economic Co-operation and Development report, by the year 2060, the amount of plastic waste produced worldwide is expected to nearly triple [2]. Plastic pollution will rise along with an almost threefold increase in plastic use brought on by rising populations and incomes unless drastic measures are taken to reduce demand, lengthen product lifespans, improve waste management, and increase recyclability. According to the report, in 2060, nearly two-thirds of plastic waste will come from disposable items like packaging, inexpensive goods, and textiles. Globally, plastic waste is expected to increase from 353 Mt in 2019 to 1,014 Mt in 2060, more than tripling the amount of plastic waste that leaks into the environment each year to 44 Mt. Poor social practice and/or unregulated waste disposal cause plastic pollution to enter the environment.

Understanding the transport mechanisms of MP particles in water is crucial step in developing effective strategies to mitigate their impact. Despite extensive research efforts, there remains a significant knowledge gap regarding the behavior and fate of MP in different aquatic settings. This is largely due to the complex coaction of variables such as particle size, shape, density, and the hydrodynamic conditions in the water bodies they inhabit. Therefore, comprehensive studies that combine both experimental and numerical approaches are essential to further understand this complex interaction. This thesis is motivated by the need to upgrade the existing knowledge gaps in MP transport dynamics. By conducting a series of experiments to determine the drag coefficient of MP particles using a hydraulic channel, and by developing a corresponding numerical model, this research aims to provide a detailed analysis of MP particle behavior

in flowing water. The experimental results offer empirical data that further enhance understanding of MP drag characteristics, while the numerical model allows for the simulation of various scenarios and the prediction of particle trajectories under different flow conditions. Integration of experimental and numerical methods in this study is particularly significant. Experimental data provides the necessary validation for the numerical model, ensuring its accuracy and reliability. Conversely, the numerical model extends the applicability of the experimental results by allowing the analysis of a wider range of conditions that may be challenging to replicate experimentally.

In conclusion, the motivation for this research comes from the need to address the environmental challenges posed by MP pollution. By combining both experimental and numerical methodologies, this study aims to enhance the capabilities of a comprehensive analysis of MP particle transport in water, thereby contributing valuable knowledge to the field and supporting efforts to protect and preserve our aquatic environments.

1.2 Scientific contributions

The primary hypothesis of this study is that for MP particles ranging from 1 to 5 mm in a parallel water flow with velocities between 0 to 1 m/s, a generalized model for quantifying the resistance function in the form of drag coefficient (c_d) and Reynolds number (Re) can be established, accounting for the diverse shapes of MP particles. To test this hypothesis, a comprehensive database of kinematic functions for MP particles was developed using experimental methods. This database facilitated the definition of the functional relationship between the measured flow parameters, geometric characteristics and drag of the MP particles. To integrate all collected results into a single constitutive model for the c_d(Re) function, a parametrization model for MP particle shapes was proposed.

In the second phase of the research, a numerical model based on the experimental conditions was constructed. Numerical analysis validated the initial hypothesis by comparing the results obtained from the numerical model with the subject model c_d(Re) and experimental data. For validation purposes, a comparison of the kinematic functions of MP particles with arbitrary shapes was provided. The main scientific contribution lies in producing a calibrated drag coefficient model for a test range of flow parameters and geometric parameters of the MP particles. Additionally, the study elaborates on the use of photogrammetry technology, offering further

contributions to the methodology for collecting data on MP particle trajectories. Additionally, the further development of the experimental methodology for investigating the transfer of particles in a water using hybrid modeling, i.e., the use of a numerical model defined by the boundary and geometric conditions achieved in the experimental channel, to determine the velocity field in the experimental analysis, can be mentioned.

1.3 Research methodology

Research activities are based on the application of experimental methods of fluid mechanics and methods of numerical modeling of fluid flow. The application of experimental technology is necessary for the purpose of collecting a relevant database for the approximation of kinematic functions of MP particle transport in the considered range of hydrodynamic conditions. This step is important for testing the working hypothesis but also demanding in terms of ensuring controlled flow conditions. Test samples of MP particle trajectories are particularly sensitive to local changes in the fluid flow, and therefore the application of the measurement technique is not trivial. In order to reduce the interaction between the measuring equipment and the measuring object (MP particle), the possibility of using video equipment during the collection of experimental data was tested. For the implementation of laboratory research, an experimental channel was used in the Hydraulic Laboratory of the Faculty of Civil Engineering in Rijeka, which with its technical specifications meets all the conditions set by the experimental research plan. Steady flow conditions can be established inside the channel with different kinematic flow characteristics. The experimental channel was constructed in such a way that it offers the possibility of changing the water depth at the upstream end and the possibility of changing the flow at the downstream end. With this, all the necessary prerequisites for carrying out tests in a range of flow parameters have been met. In order to reduce the input of the amount of motion to MP particles (linear and angular), a launching ramp was built within which the amount of motion of MP particles will be transferred only from the moving water.

To ensure controlled flow conditions, the velocity field inside the channel was measured. This is necessary to define the local Reynolds number, i.e. for the purpose of defining the difference between the speed of MP particles and the speed of water. For this purpose, an ultrasonic flow velocity meter was used, and its results were compared with a calibrated numerical model of the same flow scenario. In other words, for the purpose of measuring the flow velocity, a hybrid

experimental-numerical model was defined. The numerical model defines the same geometry of the channel within which the measured water flow will be set. The MP particles were prepared using a 3D printer that can reach an accuracy significantly higher than the range of dimensions of the MP particles included in this research. It is reasonable to expect that deviations in the kinematic functions of MP particles occur as a result of perturbations in the initial conditions of the amount of motion, local fluctuations of the flow velocity, and potential imperfections in the MP particle samples. For this reason, it was necessary to form conclusions for a particular grouping of tested samples on the basis of previously performed statistical analysis, which imposed the need to test a larger number of samples. The kinematic functions of the MP particles inside the experimental channel were determined using the video technique in such a way that the movement of the MP particles within the space of the experimental channel was continuously recorded. For this purpose, a planar flow of water is ensured, i.e. a flow of water due to which MP particles move principally in a plane perpendicular to the orientation of the video camera lens. The position of MP particles within the analyzed area was monitored using algorithms for object movement detection, according to which prerequisites were created for determining the time change of coordinates of MP particles within the flow domain. By derivation of these functions, the velocity of the MP particles was obtained, and by re-derivation, the acceleration of the particles was obtained. With the known field of water velocities determined by the hybrid model and the known velocities and accelerations of MP particles, the c_d (Re) function is determined for a tested Reynolds number range. In order to examine the justification of the proposed research protocol, validation tests were carried out for spherical MP particles and the function c_d (Re) was determined for them. The obtained results were compared with the results of previous research from the literature. After the validity of the research procedure has been confirmed, the same methodology was applied to other shapes of MP particles

1.4 Organization of the thesis

In the first part of the thesis, a brief overview of the known characteristics of MP particles is given. Starting with general properties of commonly used MP and parameterization methods applied so far in the field of particle characterization. This chapter also presents parameterization methods used in thesis.

Third chapter gives an overview of experimental and numerical research in this field and the known methods used to quantify the influence of shape on the motion of irregular particles. In chapter 4, a discussion is presented about acting forces on the body in fluid stream, following with analysis of drag models under steady and unsteady flow conditions. Finally, a newly proposed drag model for particles in fluid flow is presented in this chapter.

In chapter 5, experimental setup is explained in detail together with the methods used for the capture of particle motion. Here, manufacturing process and geometric characteristics of MP particles used are also presented. Furthermore, this chapter describes how velocity field in the experimental flume was measured together with methods employed. In the final part of chapter, experimental results are presented together with shape based drag coefficient approximation. Finally, regression models are proposed that can be used to quantify the drag coefficient within the achieved Reynolds number ranges.

Chapter 6 presents numerical model employed to reconstruct results from conducted experiment. Comparison of the trajectories obtained by the numerical model and experimental measurements is given. Furthermore, a correction of the numerical procedure in terms of quantifying the influence of shape on particle motion is proposed.

Final chapter gives brief overview of the conducted experimental and numerical research, together with model results. Finally, established scientific contributions and conclusions as well as possible directions for further research are presented.

2 Overview of previous research

Research related to the presence of MP particles in the environment is rapidly increasing because of the threat that this poorly degradable substance poses to all organisms. The activities that are undertaken for the purpose of reducing all undesirable consequences can be classified into a group of those that prevent their further introduction into the environment (measures to prevent and reduce the genesis of MP) and those related to understanding their movement. Studying the transport of particles in a fluid is a demanding scientific challenge. Scientific consensus has been reached that the density, shape and size of particles represent the most important parameters that affect the transport of all types of sediments, including MP particles. Recent knowledge on the omnipresence of MP particles in aquatic environments requires the intensification of research in the field of transport and deposition of MP using both experimental and numerical approaches. While numerical modeling offers predictive capabilities and can be particularly helpful for comprehending complex, large-scale systems, experiments offer direct, quantitative data and allow for controlled investigations.

2.1 Experimental research

Experimental research on the motion of solid particles in fluids includes a wide range of disciplines and applications. Key areas of focus include sediment transport, particle-fluid interactions, and industrial particle-laden flows. Experiments from sediment transport often focus on understanding the mechanics of sediment movement under different flow conditions [60, 28]. Understanding particle-fluid interactions can be important step in order to optimize industrial processes such as mixing, separation, and chemical reactions. Experimental research focuses on measuring drag forces, lift forces, and particle trajectories [57].

The transport and behavior of spherical particles in fluids is in general a well-researched field due to its fundamental importance in various scientific and engineering disciplines, including environmental science, chemical engineering, and fluid dynamics. Understanding how particles move and interact within a fluid medium is critical for applications ranging from pollution control to drug delivery systems. The settling behaviour of a single particle at low Reynolds numbers (Re<1) was first examined by Stokes [59]. In transitional regime characterized by $0.1 < Re < 1000$, drag force and settling velocity is predicted using empirical correlations [31]. For high

Reynolds numbers (Re > 1000) drag coefficient becomes relatively constant [25].

Experimental studies on non-spherical particles in fluid flow have shown greater complexity when compared to spherical particles. These complexity emerge from the various shapes and orientations of non-spherical particles, which influence their drag, settling velocity, and rotational behavior [16, 33]. Non-spherical particles experience different drag forces depending on their shape and orientation. Terminal settling velocity of non-spherical particles is generally lower than that of spheres with the same volume due to higher drag [69]. Non-spherical particles create more complex flow patterns compared to spherical particles. These patterns influence particle interactions and the overall dynamics in suspensions. Due to complexity of shape effects, developing models that accurately predict the behavior of non-spherical particles still presents scientific challenge.

One of the first experimental studies of MP were conducted by [9], where hydrodynamic behavior of non-bouyant plastic pellets was examined using a combination of numerical modeling and laboratory experiments. Numerical model was built by using settling velocity properties, critical shear stress values and experimental particle density. A series of experimental tests were conducted to establish the average pellet density, settling speed, bed load transport, critical shear stress, and resuspension shear stress thresholds. Average measured density of the MP pellets was $\rho = 1055 \pm 36$ kg/m^3 which compared to laboratory seawater density (1027 kg/m^3) classified them as non-bouyant particles. This experiment concluded that further research is required to determine the amount of MP in the aquatic environments and to comprehend the subsurface behavior of non-buoyant microplastics.

In [44], a series of laboratory experiments were conducted to observe sinking behavior of MP particles with various size, shape and density. Materials used in experiment were: polystyrene (PS, $\rho = 1050$ kg/m^3), polyamide (PA, $\rho = 1140$ kg/m^3), polymethyl methacrylate (PMMA, $\rho = 1190$ kg/m^3), polyethylene terephthalate (PET, $\rho = 1390$ kg/m^3), polyoxymethylene (POM, $\rho = 1420$ kg/m^3) and polyvinyl chloride (PVC, $\rho = 1560$ kg/m^3). MP particles were in the form of pellets of size lower than 5 mm. The sizes of the individual particles were determined using a microscope and a coupled imaging software. Due to the irregular shape of the particles, an equivalent spherical diameter (ESD) was determined for the purpose of shape parameterization. The sinking experiments were conducted in three uniform settling cylinder shape columns (40 cm long and 7.5 cm in diameter) filled with water in a temperature-controlled room. Particles were inserted into the water column by using tweezers and to make sure the particles reached

their terminal velocity, the recording began at 15 cm below the artificial water surface. Validation of the experiment was done by using sphere particles and comparing experimental results with the analytical expression by Dietrich [22].

The analysis of the influence of size and shape on the deposition process was continued in [41]. This study analyzed three groups of manually made MP particles. First particle group were pieces of aged fishing line with different diameters and densities (d_p = 0.15...0.71 mm and ρ = 1130...1168 kg/m^3) cut from the shreds found at the coastline. Second and third particle group consist of spherical and cylinder-shaped granules from Polycaprolactone (PCL, ρ = 1131 kg/m^3). A series of experiments were conducted to measure the settling velocity in a glass column with dimensions of 18 × 18 × 110 mm and wall thickness of 10 mm. For comparison with experimental data for PCL spheres and cylinders, a few different semi-empirical formulae were selected that are typically used for perfect spheres and natural sediment particles in transitional flow regime. Capability of the implemented formulations to predict the settling velocities of experimental particles was evaluated by computing the average relative error E and the coefficient of determination R^2. A total of 600 measurements were conducted for settling velocity of MP particles. The largest PCL sphere (4.9 mm diameter) demonstrated settling velocity of 127 mm/s, while the thinnest and shortest FL cut (0.5 mm length) showed settling velocity of 5 mm/s. Results showed considerable effect of particle shape on settling behavior of particles in the water column. For every set of particles with a characteristic particular shape, the dependence of the settling velocity on the particle size was evident; however, the nature of the relationship between the velocity and size was predetermined by the shape and could not be adequately captured by a single universal dependency.

Wider range of MP shapes were analyzed in [66]. Polymer types used in experiment were: polypropylene (PP) with ρ = 830...920 kg/m^3, polyethylene (PE) with ρ = 890...980 kg/m^3, polystyrene (PS) with ρ = 1040...1100 kg/m^3, expanded polystyrene (EPS) with ρ = 10...40 kg/m^3, polyvinyl chloride (PVC) with ρ = 1160...1580 kg/m^3, Polyethylene terephthalate (PET) with ρ = 960...1450 kg/m^3 and polyamid block copolymers (COPA) with ρ = 1020...1160 kg/m^3. Particle shapes tested were sphere, pellet, fiber and fragment, with sizes between 300 µm and 5 mm. A plexiglass column with a square cross-section of 20 × 20 cm and a length of 1 m was used for settling of MP particles. Since the aim of the experiment was to assess the terminal velocities of the particles, the top and bottom 15 cm of the water column were left out of the measurements in order to allow the particle to accelerate. For precise measurements of

particle sinking and rising, Particle Image Velocimetry (PIV), a non-contact optical technique, was used. This method allowed for detection of secondary movements of the particles as well as vertical movements downward or upward can be assessed. In this research nearly 500 physical experiments were conducted in total. The dimensionless particle diameter D^* was calculated in order to quantify the effects of shape and roundness and separate the corresponding effects from the effects of particle density and size.

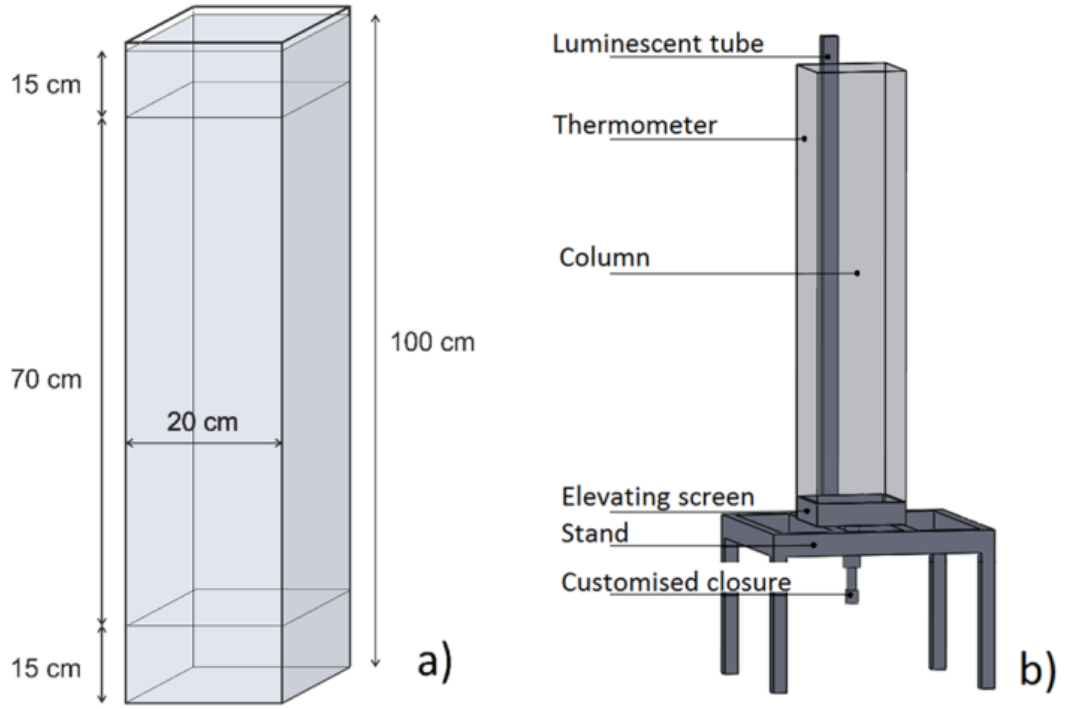

Figure 2.1: Schematic representation of glass column used for settling velocity experiment [66]

The calculated settling velocities of MP particles were compared to sediment transport formulae from existing literature like Stokes law and Dietrich's settling velocity formula. Results showed that experimentally determined velocities differed significantly from theoretical expressions. Authors proposed new empirical formula based on experimental data.

$$w_s = \sqrt{\frac{4}{3} \cdot \frac{d_{equi}}{c_d} \cdot \frac{|\rho_p - \rho_f|}{\rho_f} \cdot g}, \tag{2.1}$$

where w_s is static particle settling velocity (m/s), ρ_p is particle density, ρ_f is fluid density and c_d is drag coefficient for particles settling in water column. Results indicated that MP behavior varies from water sediment and that a use of common sediment transport formulae in observing MP motion should be treated with caution. Therefore new formulae are needed for numerical

simulations of MP transfer process.

Due to the significant variation in shape of found MP particles, a wide range of MP types was needed to be considered. The first study that included film particles was conducted by [64]. Real MP waste samples were used to test different drag models based on experimental data. Additionally, results showed that particle shape is one of the key parameters affecting settling process so there was a need to test different shape descriptors. In this experiment the authors used beverage bottles composed of PET and HDPE, flowerpots composed of PP, food containers composed of PS, PE, PVC and PE shrink wrap. Each MP sample was treated with deionized water and shredded separately. In order to measure the MP particles' terminal sinking velocity, a conventional cylindrical settling column with a height of 45 cm and diameter of 10 cm was employed. The settling process was filmed using HDR Camera at 100 frames per second. Perfectly round spheres were used for the validation of the experiment and compared to expression from [22]. Using experimental dataset, eleven different drag models were assessed and compared by use of average error (AE) and root mean squared error (RMSE). The drag model of [23] is found to have the best fit based on the AE and RMSE values. In terms of shape descriptor, sphericity was found to be a suitable shape descriptor for classification of film shaped MP, and that circularity is a suitable shape descriptor to distinguish between fibrous microplastics from non-fibrous MP. The drag model in question [23] is defined as:

$$c_d = \frac{24}{Re_p} \cdot \left(\frac{1-\Psi}{Re_p} + 1 \right)^{0.25} + \frac{24}{Re_p} \cdot \left(0.1806 Re_p^{0.6459} \right) \cdot \Psi^{-Re_p^{0.08}} + \frac{0.4251}{1 + \frac{6880.95}{Re_p} \cdot \Psi^{5.05}}, \quad (2.2)$$

where Re_p is particle Reynolds number, and Ψ is particle shape factor.

Experimental research of MP particles under both steady and dynamic flow condition was also conducted in [67]. MP types used were polystyrene, polyamide, polyethylene terephthalate, and polyvinyl chloride, all with irregular shapes. Total number of 1270 particles were gathered from suppliers in form of raw plastic material. Sample particles were scraped into the irregular particles smaller than 5 mm. A hydrostatic experiment was conducted in a regular cylindrical water column, 40 cm high and 6.45 cm wide. Salinity of water was varied, with values of 0‰, 15‰, and 36‰. Using tweezers, the MP particles were released about 1 cm below the water's surface in order to eliminate the impact of surface tension. When the particles crossed the upper and lower marking lines, the initial and final times were recorded. The ratio of the settling time to the traveled distance was used to determine the settling velocity. Additionally, a dynamic

test was conducted by placing water container on a shaking instrument and applying constant rotating speed. For dynamic condition, measured settling velocity of particles was reduced in comparison to static experimental condition. Under dynamic water conditions, ellipsoid and near-sphere particles showed linear relationship with MP size, while fragment-shaped particles exhibited non-linear relationship. For the non-buoyant particles with density from 1000 to 1250 kg/m^3 settling velocity increased proportionally to rotation speed, while for particles with density over 1250 kg/m^3 settling velocity was reduced under dynamic conditions. New expressions was proposed based on the obtained experimental data and previous studies:

$$w_s = 1.0434 \cdot \frac{\rho_p - \rho_f}{\rho_f}^{0.495} \cdot \frac{d_p^{0.777} \cdot CSF^{0.710}}{\nu^{0.124}}, \tag{2.3}$$

and

$$w_d = 0.5634 \cdot \frac{\rho_p - \rho_f}{\rho_f}^{0.495} \cdot \frac{d_p^{0.777} \cdot CSF^{0.710}}{\nu^{0.124}}, \tag{2.4}$$

where w_d is the dynamic settling velocity and CSF represents particle Corey Shape Factor (3.2).

Knowledge gaps for settling process of non-spherical MP particles have been further explored by [70]. New formula for calculation of drag coefficient c_d was proposed that contains dimensionless particle diameter and two shape descriptors (CFS and sphericity). Total of 1343 experimental data for MP terminal settling velocity was collected from existing literature. Reported MP shapes were: cylinder, disk, pellet, fiber, fragment and film with nine different types of plastic based on density (PA, PVC, PS, PET, PE, PCL, POM, PMMA, FC). Authors proposed an explicit model for calculation of settling velocity w_s based on drag coefficient and dimensionless particle diameter d_*:

$$w_s = \left(\nu \cdot g \cdot \frac{\rho_p - \rho_f}{\rho_f} \right)^{1/3} \cdot \sqrt{\frac{4 \cdot d_*}{3 \cdot c_d}} \tag{2.5}$$

and a drag model:

$$c_d = \frac{c_{d,s}}{\left(d_*^{\beta_1} \cdot \phi^{d_* \beta_2} \cdot CSF^{d_* \beta_3} \right)^{\beta_4}}. \tag{2.6}$$

where $c_{d,s}$ is drag coefficient calculated for spheres based on [17] model, while β_1, β_2, β_3, and β_4 are experimental constants.

Based on collected data, strong impact of particles shape to c_d was observed. MP particles

with higher values of ϕ have lower c_d values for the same Reynolds number. Same was demonstrated for CSF parameter, particles with lower CSF value have a higher values of c_d in the same Re range. Drag formula proposed in this paper showed relative error of 15.2 % and RMSE of 17.2% which was much lower compared to existing formulae (relative error ranged 42.4...72.8% and RMSE ranged 49.0...105.8%. Model limitations are present in the fact that it can only be applicable in the transitional regime (Re_p = 1...300) and it can only be used for the settling process of single particle.

2.2 Numerical research

Numerical methods for particle transport are important part of modeling and simulating complex physical processes involving the interaction of particles with fluids or other media. These methods allow for the analysis of critical phenomena across a range of industries, from engineering to environmental studies. They are widely used in areas such as fluid dynamics, geotechnical engineering, biomedical research, and energy production. Considering MP, numerical modeling can be used for tracking the movement, accumulation, and behavior of MP particles in natural systems. It enables researchers to simulate complex processes like sedimentation, adsorption onto organic matter, and interactions with marine organisms.

Some of the main applications of numerical models in the field of particle transport are used for simulation of sediment behaviour. Wu et al. [68] developed a 3D numerical model to simulate flow and sediment transport in open channels. The model uses the full Reynolds-averaged Navier-Stokes equations to predict fluid flow, combined with sediment transport mechanisms to analyze sediment movement and deposition. This study addressed some challenges in turbulence modeling and particle-fluid interactions, presenting significant improvements in capturing sediment transport dynamics. Henniger et al. [34] conducted direct numerical simulations (DNS) to model particle transport in an estuarine environment. This research aimed to reduce the reliance on empirical adjustments by using high-resolution simulations to capture interactions between fluid flows and suspended particles. This approach provided insights on how particles behave under the influence of turbulent flows within the estuary. Abascal-Zorrilla et al.[3] investigated the exchange of sediment between a coastal mud bank and its neighboring estuary using numerical simulations. Their study focused on modeling current and salinity patterns with a coupled hydrodynamic-sediment model. By tackling the challenges of sediment resuspension

and deposition, they were able to improve predictions of sediment transport dynamics, which are important for understanding the interactions between coastal mud banks and estuarine systems. Greifzu et al. [29] evaluated particle tracking models implemented in both OpenFOAM and ANSYS Fluent, emphasizing the significance of accurate boundary conditions and time integration schemes, which can greatly affect the prediction of particle-laden flows in CFD simulations. Liu et al. [47] introduced a hybrid approach that combines Fast Fluid Dynamics (FFD) with the Markov Chain method to simulate transient particle transport. Bonamy et al. [14] developed sedFoam, a solver based on OpenFOAM, specifically designed for modeling sediment transport in aquatic environments.

One of the first numerical studies of MP transport in water systems was conducted by Hardesty et al. [32]. Series of numerical simulations were utilized to map MP distribution and pathways in marine environments. This study highlighted numerical methods as a tool for understanding MP behavior from ocean surface to seabed. Koelmans et al. [42] proposed a global modeling approach for tracing MP movement from land to sea. The model quantified MP emissions and transport through wastewater systems, allowing for detailed scenario analyses of MP fluxes. Mountford [50] developed an Eulerian model for three-dimensional MP distribution, focusing on common MP types in global ocean simulations. This research compared present-day findings to historical data and anticipated future trends. Bigdeli et al. [12] reviewed different Lagrangian models used for simulations of the transport of marine MP. Their analysis included advances in modeling frameworks, comparing various numerical techniques. Uzun and Farazande [63] presented an review of mathematical and numerical models developed to analyze and predict the quantity, distribution, and transport dynamics of MP in aquatic environments. This paper examined the validity of various models, comparing their integration into predictive frameworks for environmental management.

Pizzi et al. [54] validated a dataset for analyzing MP dynamics, specifically focusing on MP in turbulent upper-ocean environments. Research incorporated particle direct numerical simulations to model fluid flow around MP particles. Guo and Noori [30] studied MP behavior in freshwater, focusing on the dynamics of settling and transport processes. The research emphasized the limitations of static water models and incorporated dynamic conditions to better predict MP movement in flowing water bodies. Bigdeli and Mohammadian [13] presented a laboratory dataset to validate numerical models for MP transport and deposition. This paper focused on the behavior of spherical and cylindrical MP particles in controlled water bodies. Ji et al. [38]

constructed a numerical model to predict the settling velocity of irregular MP fragments. Their research introduced a novel shape factor to improve the understanding of MP sedimentation in aquatic environments. Chen and Zeng [15] developed a detailed model to describe the transport characteristics of MP in wetland flows. The numerical approach accounted for water density variations and MP interactions.

3 Particle properties and classification of microplastics

Understanding the fundamental properties of particles and the framework for their classification is important to correctly determine their general characteristics and the forces governing it movement. The classification of particles typically involves organizing them into categories based on shared properties, behaviors, and interactions.

3.1 General properties of MP

In order to achieve a simple categorization, plastic particles in aquatic recipients are primarily classified in accordance with their size. The size of a plastic particle is determined by measuring the greatest distance between two material points of the particle (d_p). Although there are different categorizations of plastic according to size, in recent literature [5, 7, 48] the most common is the one according to which the samples are classified into four categories:

- Macroplastics - d_p greater than 200 mm
- Mesoplastics - d_p ranging from 5 to 200 mm
- Microplastics - d_p ranging from 0.001 to 5 mm
- Nanoplastics - d_p ranging from 1 to 100 nm.

This categorization was primarily introduced because different mechanical and biological processes appear to be dominant in the mentioned spatial dimensions. In this work, focus is placed entirely on microplastics (MP) which is significant due to its presence and interaction with the ecosystems of aquatic environments, but also due to the potential of transitioning into nanoplastics through mechanical and degradation processes.

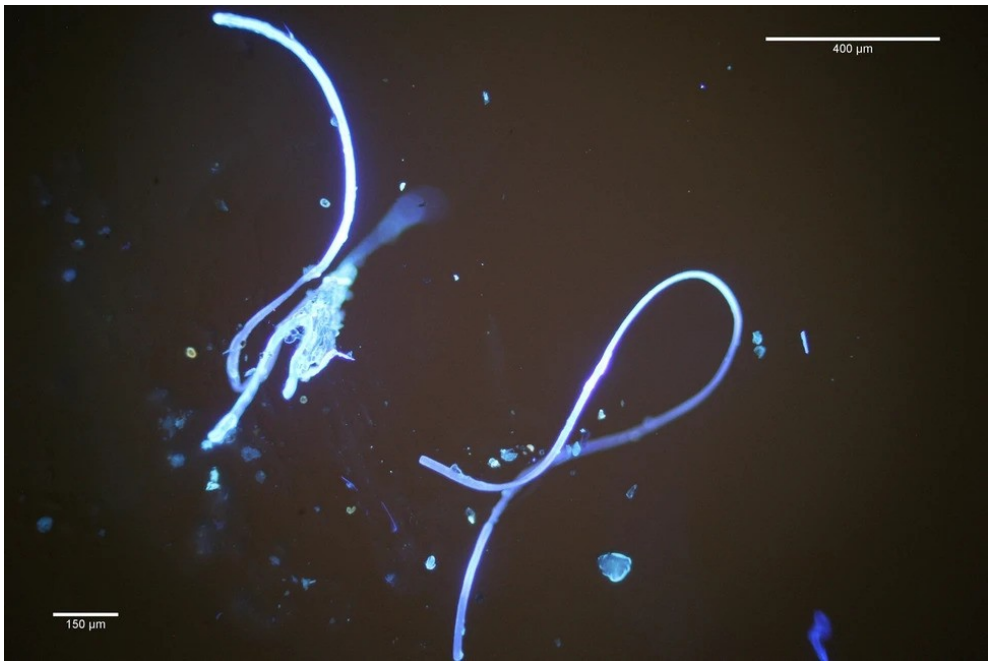

Figure 3.1: MP particles under the microscope [6].

Any particle's behavior in a fluid is governed by its physical characteristics, of which density, size, and shape contribute the most (both quantitatively and qualitatively) to its dynamics [37, 40, 46]. Particle's physical characteristics can influence processes related to the MP itself, such as molecule adhesion to the surface, aggregation with other particles, biofouling, and degradation. Also, particle characteristics significantly affect the acting forces on the surface and resulting physical processes like settling and suspension. The density ρ of MP found in water bodies can vary significantly and depends on the type of polymer and the industrial process of plastic processing. In aquatic recipients, most frequently observed type of plastics are:

- Polyethylene terephthalate (PET), ρ = 1380 kg/m³
- Polypropylene (PP), ρ = 850 ... 950 kg/m³
- Polystyrene (PS), ρ = 950 ... 1100 kg/m³
- Polyethylene (PE), ρ = 900 ... 999 kg/m³

It is important to note that, in the context of the vertical movement of MP particles in a body of water, It can be distinguished between the negatively buoyant plastic (which naturally sinks to the bottom) and positively buoyant plastic (which naturally rises to the top). In addition to the particle density ρ_p, MP particle sinking behavior also depends on the vertical distribution of the recipient density ρ_f. The density of MP can vary significantly, but recent studies show that

more than half of plastic waste produced has a density greater than the density of water, making it predominantly negatively buoyant. For negatively buoyant MP, water transport is dominantly affected by its settling process.

MP in nature comes in a variety of shapes, and their form is often determined by the source and manufacturing processes of the plastic materials. Characteristic shapes of MP are: fibers, fragments, pellets, film and foam-like particles. When categorizing MP, it is important to distinguish between primary and secondary MP. Primary MP are small plastic particles, usually with a diameter of less than 5 mm, that are purposefully created and manufactured at a small size. These can include textile fibers, manufacturing pellets, and microbeads found in personal hygiene products. Conversely, secondary microplastics come from bigger plastic objects disintegrating into smaller pieces as a result of a variety of environmental factors like weathering, abrasion, and UV light. These may result from plastic bottles, bags, or other larger plastic debris breaking down and disintegrating into smaller pieces over time. Physical, chemical, and biological processes can interact to compromise the long-term stability of plastic debris, which can result in disintegration. Plastics may photodegrade if exposed to sunlight for an extended period of time because UV radiation from the sun causes the polymer structure to oxidize and cause depolymerization in polymers. The direct exposure of plastic waste to oxygen and sunlight causes it to degrade quickly, over time becoming brittle and cracking. As the structural stability of most plastics declines, so does their susceptibility to disintegration. Plastic granules eventually contract and become microplastics as a result of this cycle. The various MP size categories raise concerns because a variety of organisms, from small aquatic life to larger animals, can consume them. Consuming MP can have negative environmental and health effects. The easier it is for a wider variety of species, including those lower on the food chain, to ingest a particle, the more likely it is that they will do so, which can result in bioaccumulation of plastic throughout ecosystems.

3.2 Shape parameterization of MP particles

Transport and settling processes of MP particles are significantly governed by particle physical properties like density, shape, and size. In order to qualitatively describe the settling process, a complete quantitative description of the mentioned parameters is required. MP waste in the environment can be the result of direct disposal (primary MP) or result of degradation processes of larger plastic debris (secondary MP). The fomer type is usually characterized by regular shapes like spheres and beads, while the latter can be found in the environment in many different forms. Typical shapes of MP in marine environments are fibers, films, foils, fragments and pellets. Because of all the above, it is especially important to define the appropriate parameterization of the shape as input data for the transport analysis [61, 43].

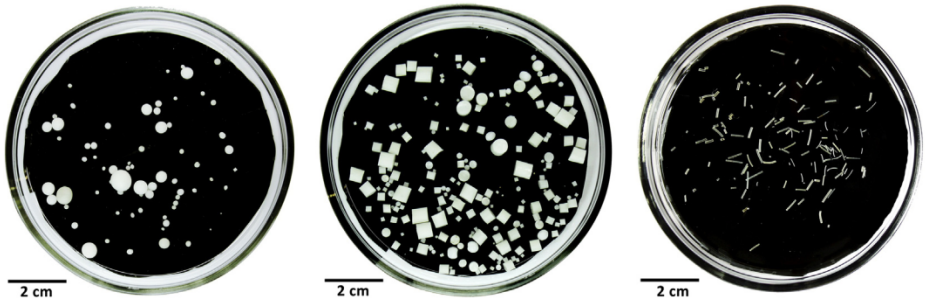

Figure 3.2: Example of some characteristic shapes of MP particles [41].

One of the first steps of particle shape analysis is calculation of the aspect ratio (AR) [53]. It is defined as ratio of the length to the width of the particle. Empirical research has shown that with smaller aspect ratio of a particle, experimental data will agree more with model results for perfect spheres [4]. Coefficient values range between 0 and 1 and are calculated according to the expression:

$$AR = \frac{b + c}{2 \cdot a}, \tag{3.1}$$

where a is the reference dimension, and b and c are the other two orthogonal dimensions of the particle. With a being the longest, b middle and c shortest dimension.

The next important factor in the parameterization of the particle shape is the Corey Shape Factor (CSF). In [41], three different shapes of MP particles were analyzed (sphere, short cylinders and long cylinders cut from fishing lines). In order to quantitative estimate the deviation of spherical particles from the ideal sphere, CSF was used [19]. CSF is a dimensionless parameter used in the context of shape analysis or characterization of particles, particularly in fields like

materials science or particle transport. Values for CFS are usually calculated using the following expression:

$$CSF = \frac{c}{\sqrt{a \cdot b}}, \tag{3.2}$$

CSF values tell us about the ratio between the longest, intermediate and shortest axes of the particle. Ideal sphere has a value of $CSF = 1$, but with more irregular shapes, this value can vary significantly. The smaller the values of the CSF number, the "flatter" the shape of the particle.

Second parameter for the systematization of the particle shape commonly used in research is Power Roundness Coefficient (P) [55, 65]. P values are determined by evaluation based on visual inspection of particles and comparison with a standardized table. There are a total of 6 categories of particles (very angular for $P = 1$, angular for $P = 2$, subangular for $P = 3$, subrounded for $P = 4$, rounded for $P = 5$ and well-rounded for $P = 6$). Roundness of particle is a function of both edge and corner sharpness and in parallel it is independent of the particle shape. In practical research of particle transport, roundness can give us information of distance traveled by particles before discharge.

Experimental results according to [41] showed that the variability in shape that characterizes real life MP significantly affects the transport and deposition rate of particles. This conclusion indicates that it is essential to pay attention to the selection of the shape parameter when constructing a numerical model for transport of different types of MP. In their study [66], researchers examined the feasibility of applying established sediment transport formulas to predict the behavior of MP particles in aquatic environments. Experimental findings revealed that the diverse morphologies of MP particles considerably influence their dynamics. Consequently, the existing sediment transport equations result in substantial discrepancies when compared to the outcomes derived from experimental observations. The shapes analyzed in the experiments included spherical particles, fragments, pellets, and fibers. To characterize the shape, size, and roundness of the particles, both the Corey Shape Factor (CSF) and the Power Roundness Coefficient were utilized. In order to quantify the influence of shape separately from the size and density of particles, the dimensionless particle diameter D^* was calculated [71]:

$$D^* = \left(\frac{\Delta}{\nu}\right)^{1/3} \cdot d_{equi}, \tag{3.3}$$

where ν is kinematic viscosity of the fluid and Δ is a ratio of particle density ρ_p and water density

ρ_f:

$$\Delta = \frac{|\rho_f - \rho_p|}{\rho_f}, \tag{3.4}$$

with d_{equi} being a geometric mean of the principal axis dimensions:

$$d_{equi} = \sqrt[3]{a \cdot b \cdot c}. \tag{3.5}$$

The results from [66] confirmed the assumption that higher values of D^* correspond to faster settling of particles, i.e. higher values of settling velocity. The linear regression analysis showed a significant interdependence of D^* and settling velocity with high statistical significance ($p < 0.001$). Additionally, correlation of settling velocity and CSF was also calculated and values showed that higher values of CSF also correspond with increased settling velocity. Finally, multivariate regression was computed for CSF and D^*. Results showed that the diameter of the particle has a more significant effect on the rising and settling velocity than the shape expressed through the CSF. The correlation of Powers roundness and settling velocity was not observed, i.e. the statistical analysis result of $p > 0.05$ indicates that this relation is not statistically significant. This experimental study further emphasized importance of MP shape on transport processes which also applies to freshwater systems.

Comprehensive analysis was performed by [64] in order to categorize shape influence on the behavior of MP particles in water systems. The authors compared eleven different drag coefficient models using seven different shape descriptors and measured their performance on a real data set. Shape descriptors in question were Powers index (P), Corey Shape Factor (CSF), circularity (λ), sphericity (ϕ), elongation (e) and flatness (F).

Flatness and elongation [8] together with CSF belong in the group of form factors which give us information about 3-dimensional characteristic of the particles. Flatness (F) and elongation (e) are defined as:

$$F = \frac{c}{a}. \tag{3.6}$$

$$e = \frac{b}{a}. \tag{3.7}$$

These form factors are calculated based on form dimensions that are noted as: a - longest, b - intermediate, and c - shortest length of the particle ($a > b > c$). They provide a quantification of

the rate of flatness and elongation of a particle. Particle form factors are easier to measure than factors like sphericity and circularity. They have lower dependency with measurement scale, and can distinguish particles of different shapes. The main limitation of form factors is their reliance on operator judgments which may vary in different studies.

Sphericity Φ [23] is, together with the aforementioned form factors, one of the most common shape descriptors used in literature. Sphericity is a measure of how much an object's actual surface area deviates from the corresponding surface area of a sphere with the equivalent radius. It can be defined as:

$$\Phi = \frac{A_{sph}}{A_p}. \tag{3.8}$$

where A_{sph} is defined as the surface area of the equivalent sphere and A_p represents the particle surface area. A_{sph} can be expressed as:

$$A_{sph} = \sqrt[3]{35 \cdot V_p^2 \cdot \pi}, \tag{3.9}$$

where V_p is particle volume.

Sphericity Φ values range between 0 and 1, where 1 represents an ideal sphere. It quantifies the deviation of the shape of the observed particle from the ideal sphere. Particle sphericity is an especially useful parameter because it is directly correlated with transport behavior of MP particles, and their characteristics in various processes and environments. For particles that do not have a single dominant dimension, sphericity is one of the best parameters for shape description. Sphericity's key disadvantage is its reliance on particle surface area. Although the analytical calculation of surface area for regular particle with a smooth surface is possible, calculation of surface area for irregular particles requires sophisticated tools such as 3D scanners or microscopes. Furthermore, the measured surface area is a function of measurement accuracy, and it is correlated with resolution and accuracy of experimental measurement. As a result, sphericity does not represent an absolute shape descriptor for irregular particles and, in order to be reproducible, should be presented together with measurement accuracy.

Another shape descriptor used in practice that is not solely based on form dimensions is circularity [23]. Circularity quantifies how closely an object referent projection perimeter relates to a projection perimeter of a perfect circle. It is defined as:

$$\lambda = \frac{P_{mp}}{P_c}. \tag{3.10}$$

where P_{mp} represents maximum projection perimeter of the particle and P_c represents perimeter of the circle equivalent to the maximum projection area of the particle A_{mp}. Circularity λ can take values from 1 upwards, where 1 represents an ideal circular contour.

Finally, the combination of these two descriptors can be used in the form of shape factor ψ. It is defined as a ratio between sphericity and circularity and thus takes into account shape properties from both descriptors [21]:

$$\psi = \frac{\Phi}{\lambda}. \tag{3.11}$$

All of the factors mentioned above provide a quantitative way to describe and differentiate particle shapes, capturing various geometric aspects such as roundness, sphericity, and angularity. This allows for a more detailed understanding of particle morphology beyond simple size measurements. Shape parameterization aids in the analysis of processes like particle transport and sedimentation. Furthermore, it helps with design process of more efficient models by understanding how shape influences physical processes. Furthermore, integrating shape factors into computational models improves results of simulations involving real world particle dynamics. Despite their wide application, it can be challenging to measure them accurately, especially for irregular or complex shapes. All the shape factors listed above should be used depending on the type of problem and the level of expected model results.

3.3 Proposed parameterization

As previously discussed, the morphology of MP particles is one of critical factors in modeling their transport within aquatic environments. In practice, MP particles often exhibit irregular shapes, demanding a standardized representation for precise comparison of model results and analyses. In this research, high-precision 3D printer was used for production of particles with well-defined geometries. This approach enables accurate and reproducible numerical analysis by ensuring known geometric characterization of the particles, including important metrics such as characteristic diameter and projected surface area. This improved precision in geometric data significantly improves the accuracy of the modeling approach. In order to connect regular,

laboratory-produced particles and the natural irregular MP shapes, parametric shape analysis was employed.

Given the sensitivity of the experimental procedure and empirical analysis, it was necessary to use relatively simple particle shapes. Employing MP particles with irregular and variable geometries, as found in the environment, would compromise reproducibility and weaken the analysis. Therefore, particles in this experiment were designed and produced in the form of Euclidean solid bodies. Term Euclidean bodies refers to three-dimensional geometric figures that exist in Euclidean space and are characterized by their regularity and symmetry. Specific type of Euclidean bodies are called Platonic solids which are highly symmetrical polyhedra with faces composed of congruent polygonal faces, i.e. the same number of faces meeting at each vertex. There are five Platonic solids in total: tetrahedron (4 triangular faces), cube (6 square faces), octahedron (8 triangular faces), dodecahedron (12 pentagonal faces), and icosahedron (20 triangular faces). Defined exact formulas for calculation of surface areas and volumes, together with a high level of symmetry, enables the use of this shape types for detailed experimental and numerical analysis. Characteristic expressions for calculating areas and volumes are given in Table 3.2.

Platonic Solids	**Faces**	**Edges**	**Vertices**	**Contiguous faces**
Tetrahedron	4 equilateral triangles	6	4	3
Cube	6 squares	12	8	3
Octahedron	8 equilateral triangles	12	6	4
Dodecahedron	12 regular pentagons	30	20	3
Icosahedron	20 equilateral triangles	30	12	5

Table 3.1: Geometric properties of Platonic solids

Shape	Surface Area	Volume
Tetrahedron	$\sqrt{3}\ a^2$	$\frac{\sqrt{2}\ a^3}{12}$
Cube	$6\ a^2$	a^3
Octahedron	$2\sqrt{3}\ a^2$	$\frac{\sqrt{2}\ a^3}{3}$
Dodecahedron	$3\sqrt{25+10\sqrt{5}}\ a^2$	$\frac{1}{4}(15+7\sqrt{5})\ a^3$
Icosahedron	$5\sqrt{3}\ a^2$	$\frac{5}{12}(3+\sqrt{5})\ a^3$

Table 3.2: Surface area and volume for different shapes.

Platonic solids are highly symmetric, which ensures that the particles have uniform properties. This uniformity is important for controlled experiments, as it allows for isolation of the effects of shape on transport behavior without the negative influence of other geometric irregularities. Secondary, each Platonic solid has a unique shape, ranging from the tetrahedron to the more complex dodecahedron and icosahedron. This diversity allows us to study the impact of different shapes on MP transport in a systematic and comprehensive manner. The geometry of Platonic solids is well-defined and mathematically straightforward. This simplifies the modeling and analysis of their behavior in flowing water, as parameters such as surface area, volume, and drag coefficients can be easily calculated. Additionally, Platonic solids can be accurately reproduced using 3D printing. This reproducibility ensures that each particle is identical, which is important for experimental consistency and to make valid comparisons between different shapes.

While natural MP may not be perfect Platonic solids, studying these shapes can provide insights into the transport behaviors of particles with different geometries. The results can help to generalize findings to a broader range of particle shapes found in natural environments. Interaction of Platonic solids with fluid flow can be more easily analyzed due to their regular geometry. This can help in our understanding on how different shapes influence parameters like settling velocity, dispersion rates, and interaction with flow boundaries. By understanding the transport behavior of simple, well-defined shapes, a baseline can be established for comparing more complex, irregularly shaped particles. This benchmark can be useful in future research and in developing theoretical models for MP transport. In summary, the use of Platonic solids provides a controlled, reproducible, and mathematically tractable way to study the effects of particle shape on MP transport in flowing water. This allows for clearer insights and more robust conclusions in presented experimental research.

In the scope of the experimental study, the most common shape parameters were tested and

their applicability to the transport of MP particles was assessed. The factors taken into account are: Corey Shape Factor (CSF), Aspect Ratio (AS), Form Factor (F), Eccentricity (e), sphericity (Φ), circularity (λ), and shape factor (ψ). In the case of a sphere, all three characteristic sizes of the body (a, b, and c) are equal to the sphere diameter. In the case of other bodies, the characteristic quantities can be expressed through the edges of the particles with regard to their symmetry. Furthermore, calculation of the commonly used shape factors can be conducted easily with well defined geometric characteristics of the body. Values for basic shape factors (CSF, AS, F and e) are presented in Table 3.3.

Shape	CSF	AS	F	e	Φ	λ	ψ
Tetrahedron	1.00	1.00	1.00	1.00	0.67	1.29	0.52
Cube	1.00	1.00	1.00	1.00	0.81	1.13	0.71
Octahedron	1.00	1.00	1.00	1.00	0.84	1.71	0.49
Dodecahedron	1.00	1.00	1.00	1.00	0.91	1.02	0.89
Icosahedron	1.00	1.00	1.00	1.00	0.94	1.09	0.86

Table 3.3: Values of shape factors for Platonic solids: Corey Shape Factor (CSF), Aspect Ratio (AS), Form Factor (F), Eccentricity (e), sphericity (Φ), circularity (λ), and shape factor (ψ) .

The data presented in Table 3.3 indicate that parameters such as Corey Shape Factor, Aspect Ratio, flatness, and elongation are insufficient for differentiating among the shapes chosen for the experimental analysis. This limitation arises from the high degree of symmetry present in the experimental shapes due to the intentional use of Platonic solids. Therefore, to develop a robust numerical model, it is essential to utilize shape descriptors capable of discriminating between these symmetrical forms. To effectively quantify the influence of particle shape on the transport process, it is crucial to adopt more sophisticated parameters, such as sphericity, circularity, and shape factor. These variables are capable of differentiate between various symmetrical forms. The corresponding values are also provided in Table 3.3.

The calculated values show clear difference in ability to distinguish between five chosen shapes of MP. Sphericity values range from 0.67 for tetrahedron to 0.94 for icosahedron, increasing with the rising number of faces. This is expected because with increase in number of faces, the body becomes closer to the ideal sphere with $\Phi = 1$. Values for circularity increase as the projection of the body moves away from the perfect circle or as the body becomes more stretched. Maximum value is 1.71 for octahedron and minimum is 1.02 for dodecahedron. Shape

factor ψ values give combined information of both projection perimeter and surface area of MP particle.

The presented shape parameterization will be correlated with experimentally measured drag coefficients and water flow conditions represented by the Reynolds number. A numerical model is proposed that quantifies these relationships for known particle shapes using parametric methodology. Historically, the characterization of MP shapes has largely depended on subjective assessments by researchers and statistical analyses of particle shape distributions. This approach, while useful, has limitations. Visual inspection is often subjective, leading to potential inconsistencies in shape classification. Additionally, relying on qualitative assessments and basic statistical analyses can limit the ability to conduct rigorous quantitative analyses. Transitioning from subjective assessments and basic statistical analyses to the use of Platonic solids can represents a significant advancement in the study of MP transport. This approach enhance the advantages of standardized, reproducible shapes to underline the precision, reliability, and depth of experimental research.

4 Physics of a body in fluid

In this chapter, an brief overview of the fundamental physical principles governing fluid behavior and its interaction with solid bodies is provided. The focus is on laying out basic theoretical framework necessary for understanding fluid motion and the forces acting upon particles immersed in it. This includes conservation laws such as the conservation of mass and momentum, as well as the mathematical equations that describe fluid dynamics, also known as Navier-Stokes equations. Additionally, the chapter addresses turbulence modeling, an essential aspect for accurately predicting fluid behavior under various conditions.

4.1 Theoretical basis for flow description

Fluid dynamics is a complex area that requires a wide theoretical foundation to accurately understand and predict how fluids move [11, 45, 20]. This chapter lays out the core principles of fluid motion. It begins by discussing the basic conservation laws that serve as the basis for all fluid flow analysis. From there, it continues into the governing equations that define fluid behavior and concludes by exploring the techniques used to model turbulent flow.

4.1.1 Conservation of Mass

One of the basic principle in the analysis of fluid flows is conservation of mass. This principle asserts that mass cannot be created or destroyed in a closed system. In the context of a moving fluid, this law is mathematically represented through the continuity equation:

$$\frac{\partial \rho_f}{\partial t} + \nabla(\rho_f \cdot \mathbf{v}) = 0 \tag{4.1}$$

where ρ_f represents the density of the fluid, t is time, and $\mathbf{v}$ is the velocity field. The continuity equation ensures that the rate of change of mass within any control volume plus the net mass flux across the control volume's boundaries is always zero. This equation describe base concept of how fluid density and velocity are connected.

4.1.2 Conservation of momentum

Second fundamental concept is the conservation of momentum, derived from Newton's second law of motion. This principle states that the rate of change of momentum of a fluid element is equal to the sum of the forces acting on it. The governing equation for the conservation of momentum in a fluid is expressed as:

$$\frac{\partial}{\partial t}(\rho_f \cdot \mathbf{v}) + \mathbf{v} \cdot \nabla(\rho_f \cdot \mathbf{v}) = -\nabla p + \nabla \mathbf{T} + \rho_f \cdot \mathbf{g} \tag{4.2}$$

where p is the pressure, $\mathbf{T}$ represents the viscous stress tensor, and $\mathbf{g}$ accounts for external body forces such as gravity. This equation describes how forces like pressure gradients, viscous stresses, and external forces influence the fluid's motion. For fluids, stress tensor term can be expressed as:

$$\nabla \mathbf{T} = \mu \cdot \nabla^2 \mathbf{v}, \tag{4.3}$$

and equation (4.2) can be expressed in form:

$$\frac{\partial}{\partial t}(\rho_f \mathbf{v}) + \mathbf{v} \cdot \nabla(\rho_f \mathbf{v}) = -\nabla p + \mu \cdot \nabla^2 \mathbf{v} + \rho_f \mathbf{g} \tag{4.4}$$

This equation is also known as Navier-Stokes equation.

A system of equations comprising equations (4.1) and (4.4) provides a general framework for modeling fluid motion. These equations describe the motion of viscous fluids and are used to model a wide range of flow phenomena. However, due to their complexity, exact solutions are often unattainable, especially for turbulent flows.

4.1.3 Turbulence modeling

One of the major challenges in fluid dynamics is the accurate prediction of turbulent flows, which are characterized by chaotic and irregular fluctuations. Turbulent flows are prevalent in nature and engineering applications, such as air flow around an aircraft or liquid flow through pipelines. These flows are challenging to model mathematically and solve numerically due to their rapid fluctuations in velocity and pressure. Turbulence modeling in computational fluid dynamics (CFD) allows for the approximation of turbulent flow behavior without the need to resolve all individual fluctuations within the flow field. Since directly solving turbulent structures would require extremely high computational power (often beyond the capabilities of modern

computers), various approaches have been developed to approximate and model turbulent flows.

One of this approaches is the Reynolds-Averaged Navier-Stokes (RANS). The RANS approach involves decomposing the velocity field into a mean component and a fluctuating component:

$$\mathbf{v} = \overline{\mathbf{v}} + \mathbf{v}' \tag{4.5}$$

where $\overline{\mathbf{v}}$ is the time-averaged velocity, and $\mathbf{v}'$ represents the turbulent fluctuations.

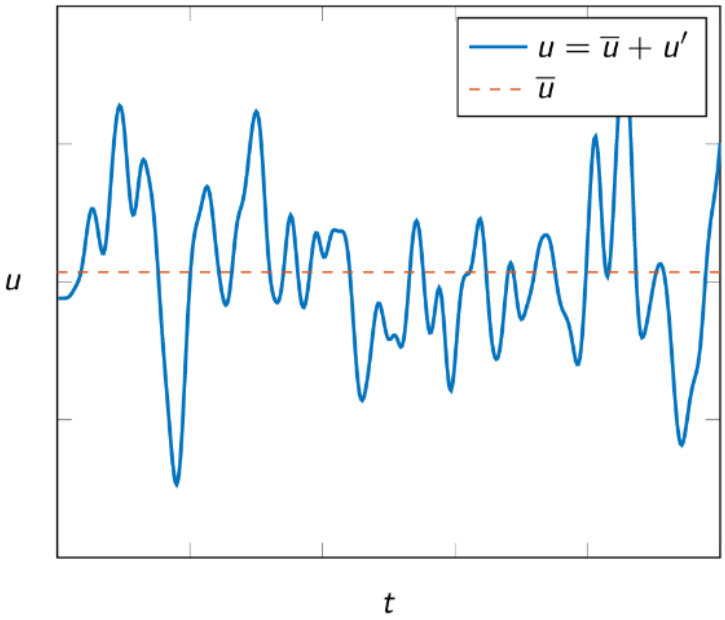

Figure 4.1: Decomposition of Turbulent Velocity in the RANS Framework.

Figure 4.1 illustrates the decomposition of a turbulent velocity signal (u) over time (t) into its mean and fluctuating components, a key concept in the Reynolds-Averaged Navier-Stokes (RANS) approach. The blue line represents the instantaneous velocity (u), which is a combination of the mean velocity ($\overline{u}$) (shown by the dashed red line) and the fluctuating component (u'). This decomposition is important part of turbulence modeling, allowing complex, fluctuating turbulent flows to be represented by their mean behavior and smaller fluctuating components. Substituting this decomposition into the Navier-Stokes equations introduces additional terms, known as Reynolds stresses, which represent the effects of turbulence. Since these terms cannot be directly calculated from the RANS equations, turbulence models such as the k-epsilon and k-omega models are employed to provide solutions. These models approximate the Reynolds stresses and make the equations solvable for engineering applications.

4.2 Acting forces on a body in fluid stream

Pressure forces and viscous forces are the two main categories of fluid forces acting on a body in a fluid [11]. These forces result from the fluid's interaction with the body and are impacted by the body's geometry, fluid viscosity, and fluid velocity. In general, hydrodynamic forces acting on a body come from two primary sources: the distribution of pressure and shear stress over the body surface. The pressure p acts perpendicular to the surface, while shear stress τ acts tangentially along the surface. The combined impact of the p and τ distributions, integrated across the entire body surface, produces the resulting hydrodynamic force (F_r) exerted on the body. The resultant force F_r can be divided into two sets of components (Figure 4.2).

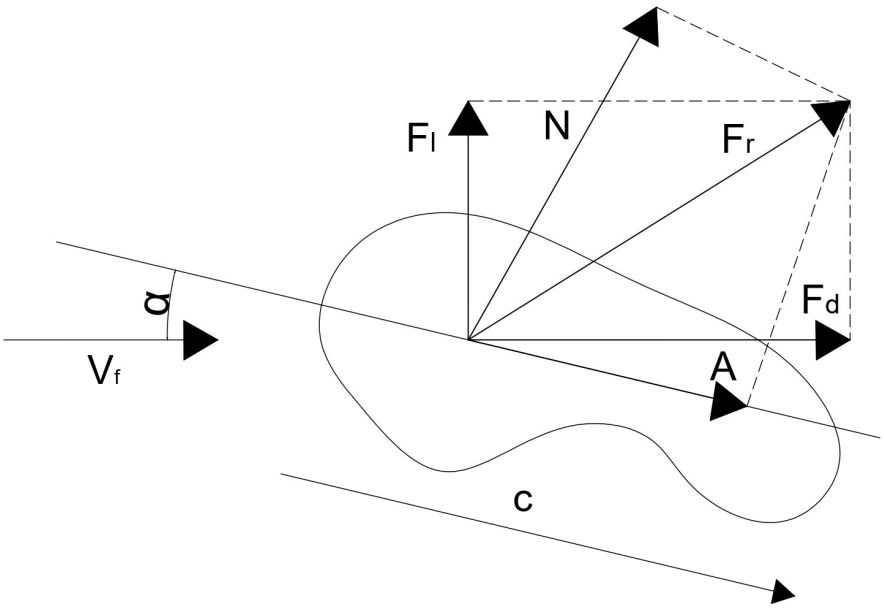

Figure 4.2: Hydrodynamic force on a body in a fluid and its components.

The hydrodynamic force F_r acting on a body can be decomposed into components relative to the flow velocity v_f and the body's axis system. Specifically, the component of F_r perpendicular to v_f is designated as the lift force (F_l), while the component parallel to v_f is termed the drag force (F_d). Additionally, when considering the body's axis system defined by the axis c, the hydrodynamic force R an be further resolved into components relative to this axis. The force component perpendicular to the axis c is known as the normal force (N), and the component parallel to the axis c is identified as the axial force (A).

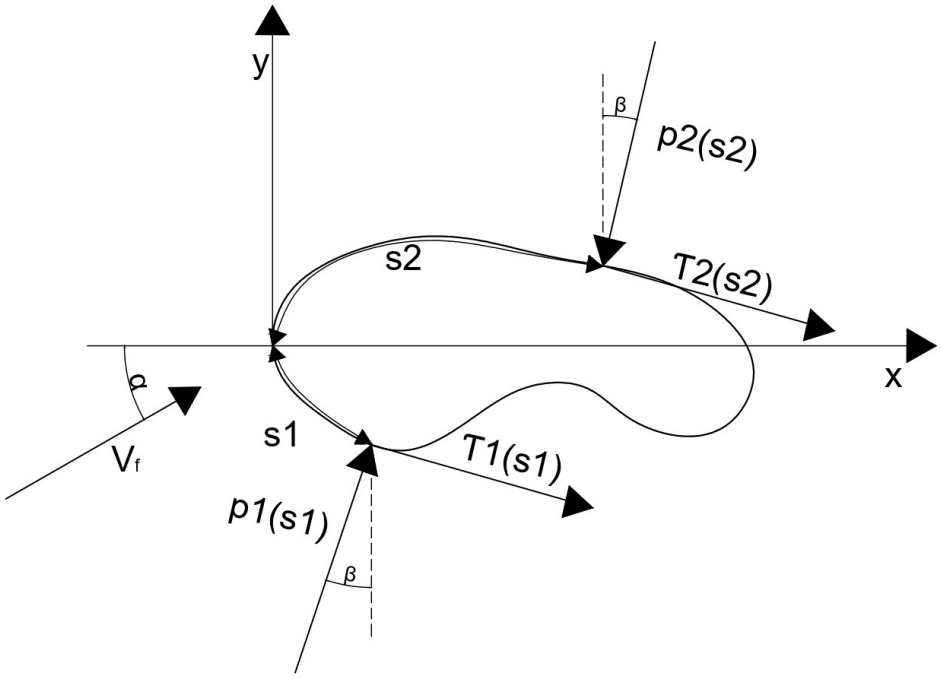

Figure 4.3: Pressure and shear stress force on a body in a fluid and its components.

To ascertain the total hydrodynamic force exerted on a body in fluid flow, it is essential to integrate the distributions of pressure and shear stress. This integration accounts for the spatial variations in velocity and pressure along the flow field near the body. Referring to Figure 4.3, the distance measured from the leading edge along the body surface to an arbitrary point A on the lower surface is denoted as s_1. Similarly, the distance to an arbitrary point B on the upper surface is represented as s_2. The pressure p_1 and shear stress τ_1 on the lower surface are functions of s_1. Correspondingly, the pressure p_2 and shear stress τ_2 on the upper surface are function of s_2. At any given point, the pressure exerts a normal force to the surface, which is inclined at an angle β relative to the surface normal, while the shear stress acts tangentially, also oriented at an angle β.

To express the contributions of pressure and shear stress on an infinitesimal surface element dS to the resultant normal force N and axial force A, the differential forces per unit span are considered. The normal force per unit span N' and the axial force per unit span A', exerted on the elemental area dS, can be mathematically formulated as follows:

a) lower body surface

$$dN_1' = p_1 \cdot ds_1 \cdot \cos\beta - \tau_1 \cdot ds_1 \cdot \sin\beta \tag{4.6}$$

$$dA_1' = p_1 \cdot ds_1 \cdot \sin\beta + \tau_1 \cdot ds_1 \cdot \cos\beta \tag{4.7}$$

b) upper body surface

$$dN_2' = -p_2 \cdot ds_2 \cdot \cos\beta - \tau_2 \cdot ds_2 \cdot \sin\beta \tag{4.8}$$

$$dA_2' = -p_2 \cdot ds_2 \cdot \sin\beta + \tau_2 \cdot ds_2 \cdot \cos\beta \tag{4.9}$$

The axial and normal forces per unit span are obtained by integrating the expressions provided in equations (4.6)-(4.9) from head end (H) to back (B). This integration process determines the cumulative contributions of the differential forces over the considered surface area.

$$N' = -\int_H^B (p_2 \cdot \cos\beta + \tau_2 \cdot \sin\beta) \cdot ds_u \; + \int_H^B (p_1 \cdot \cos\beta - \tau_1 \cdot \sin\beta) \cdot ds_1 \tag{4.10}$$

$$A' = \int_H^B (-p_2 \cdot \sin\beta + \tau_2 \cdot \cos\beta) \cdot ds_u \; + \int_H^B (p_1 \cdot \sin\beta - \tau_1 \cdot \cos\beta) \cdot ds_1 \tag{4.11}$$

Taking into account the angle α between the direction c and the velocity vector v_f yields the following relationships:

$$F_l = N \cdot \cos\alpha - A \cdot \sin\alpha \tag{4.12}$$

$$F_d = N \cdot \sin\alpha - A \cdot \cos\alpha \tag{4.13}$$

Total lift and drag force per unit span can be derived by substituting (4.10) and (4.11) into (4.12) and (4.13).

The drag force F_d is interpreted as the resistance experienced by a body moving through a fluid [11, 45]. This force acts opposite to the direction of the relative motion between the fluid and the body. Drag force can be characterized in different flow regimes by the Reynolds number and the body shape. For small particles in laminar flow, where (Re $<$ 1), the drag force can be described by Stokes' law. The drag force (F_d) acting on a spherical particle of radius (R) is given by:

$$F_d = 6 \cdot \pi \cdot \mu \cdot R_p \cdot \left(v_f - v_p\right) \tag{4.14}$$

Here μ is the dynamic viscosity of the fluid, R_p is the radius of the particle, v_f is the fluid velocity, v_p is the particle velocity. Stokes' law assumes that the flow around the particle is steady and the viscous forces dominate over the inertial forces.

For higher Reynolds numbers (Re $>$ 1), typically in turbulent flow regimes, drag force is modeled using a drag coefficient (c_d), which depends on the particle shape and the Reynolds number. Drag force is given by:

$$F_d = \frac{1}{2} \cdot c_d \cdot \rho_f \cdot A \cdot \left|v_f - v_p\right| \cdot \left(v_f - v_p\right) \tag{4.15}$$

where A represents the area of the projection of the surface of the particle on a plane perpendicular to the direction of motion, which changes as particle rotates. Lift force acts perpendicular to the direction of the relative motion between the fluid and the particle and arises due to pressure differences on the surfaces of the particle. For small spherical particles in a shear flow, the lift force can be approximated using the Saffman lift force F_l:

$$F_l = 1.615 \cdot \rho_f \cdot R_p \cdot |v_f - v_p| \cdot \gamma \tag{4.16}$$

where γ is local shear rate of the fluid. Buoyancy force F_b is an upward force exerted by a fluid that opposes the weight of an immersed object. It is often described by Archimedes' principle:

$$F_b = \rho_f \cdot V \cdot g \tag{4.17}$$

Other forces acting on a body in a fluid stream are the added mass force and Basset force. The added mass force arises from the inertia that results from additional volume of the surrounding fluid that moves together with particle [45]. It is given as:

$$F_{am} = C_m \cdot \rho_f \cdot V \cdot \frac{dv_f}{dt} \tag{4.18}$$

where C_m is the added mass coefficient.

Basset force accounts on how the relative velocity between the fluid and the body has changed over time [11]. It represents the lag in the development of the boundary layer around the particle due to changes in velocity. The Basset force is given by:

$$F_B = 6\pi\mu R^2 \cdot \int_0^t \frac{1}{\sqrt{\pi\nu(t-\tau)}} \cdot \frac{dv_r(\tau)}{d\tau}\, d\tau \tag{4.19}$$

The overall equation of motion for a particle in a fluid, combining all the above forces, has a form of:

$$m_p \cdot \frac{dv}{dt} = F_g + F_b + F_d + F_l + F_{am} + F_{\text{basset}} \tag{4.20}$$

where F_g is the gravitational force:

$$F_g = m_p \cdot g \tag{4.21}$$

4.3 Drag coefficient of a body in fluid

4.3.1 Drag coefficient under steady motion

Drag coefficient c_d is a dimensionless parameter used to quantify the resistance encountered by an object as it moves through a fluid medium. It is derived from the phenomenological model of drag force, which encompasses the effects of surface friction acting on the submerged body and the resultant force from the integration of pressure distribution around the object, collectively contributing to the overall resistance during motion. Drag coefficient, which is predominantly influenced by the shape of the particle, has been empirically determined to exhibit a correlation with the local Reynolds number Re_p. Local Reynolds number in particular is one of the crucial parameters for understanding the behavior of solid particles in fluid streams. It characterizes the relative importance of inertial forces to viscous forces acting on a particle, influencing its motion, interaction with the fluid, and resultant forces such as drag and lift. It is important to note that this correlation is based on the Reynolds number Re defined with respect to the characteristic dimension of the immersed object. In the context of MP particles, a specific formulation for Re_p can be defined accordingly:

$$Re_p = \frac{\rho_f \cdot d_p \cdot |\mathbf{v}_f - \mathbf{v}_p|}{\mu} \tag{4.22}$$

For the $x - z$ plane (with x axis being the axis in the direction of fluid flow and z axis being the vertical axis, i.e. the axis of gravity) this can be written as:

$$\mathrm{Re}_p = \frac{\rho_f \cdot d_p \cdot \sqrt{\left(v_{f,x} - v_{p,x}\right)^2 + \left(v_{f,z} - v_{p,z}\right)^2}}{\mu}, \tag{4.23}$$

where the difference of the velocity components in the numerator defines the relative velocity of the MP particle in relation to the local velocity of the fluid v_r (4.24).

$$v_r = \sqrt{\left(v_{f,x} - v_{p,x}\right)^2 + \left(v_{f,z} - v_{p,z}\right)^2}. \tag{4.24}$$

Extensive research has been conducted in examining the steady flow behavior of individual spherical particles in relation to the particle Reynolds number [27, 49]. Researchers have particularly concentrated on scenarios where Re_p is significantly less than 1, defining a state known as Stokes flow. In this regime, viscous forces exert a predominant influence, and inertial effects are negligible. Experimental studies focusing on spherical particles with relatively smooth surfaces have delineated three discernible regions within the $c_d - \mathrm{Re}_p$ relationship: the Stokes region ($0 < \mathrm{Re}_p < 1$), characterized by predominant viscous effects; a transitional phase featuring transitional flow ($1 < \mathrm{Re}_p < 1000$); and the turbulent regime ($\mathrm{Re}_p > 1000$), where inertial forces become dominant. Experimental determination of local particle Reynolds number involves measuring the relevant parameters such as fluid density, particle diameter, fluid and particle velocities, and fluid viscosity. Common experimental techniques include particle image velocimetry (PIV), high-speed photography, or, alternatively, computational fluid dynamics (CFD) simulations [11, 45].

As it was previously explained, for low Reynolds number values the expressions for the drag coefficient are well known. Stokes' drag law for $\mathrm{Re}_p < 1$ and Oseen's expression for $1 < \mathrm{Re}_p < 10$. In conditions of higher Reynolds numbers, empirical drag models are based on experimental data. For very high Reynolds numbers ($\mathrm{Re}_p > 1000$), the drag coefficient for sphere becomes relatively constant:

$$c_d \approx 0.44 \tag{4.25}$$

One of the most widely utilized drag models for spherical particles is the Clift-Gauvin model [18]. This model takes into account factors such as fluid turbulence, acceleration, particle shape

and orientation and particle-fluid mass transfer. The formula of the model has the form of:

$$c_d = \frac{24}{\mathrm{Re}} \cdot \left(1 + 0.15 \cdot \mathrm{Re}^{0.687} + \frac{0.42}{1 + \frac{42500}{\mathrm{Re}^{1.16}}} \right). \tag{4.26}$$

In practical fluid dynamics there is often a need for data correlation that spans a wide range of Re, ranging from laminar (creeping) flow, transitional flows characterized by vortices, to turbulent flows exhibiting the highest Reynolds numbers. Morrison [24] introduced an empirical formulation for the drag coefficient governing the flow of a uniform medium around a sphere. This correlation serves as a robust representation delineating the interdependency between the c_d and Re, effectively encapsulating Reynolds number magnitudes up to 10^6.

$$c_d = \frac{24}{Re} + \frac{2.6 \cdot \frac{Re}{5.0}}{1 + \frac{Re}{5.0}^{1.52}} + \frac{0.411 \cdot \left(\frac{Re}{2.63 \cdot 10^5} \right)^{-7.94}}{1 + \left(\frac{Re}{2.63 \cdot 10^5} \right)^{-8.00}} + \frac{0.25 \cdot \frac{Re}{10^6}}{1 + \frac{Re}{10^6}} \tag{4.27}$$

For low Reynolds numbers, this equation collapses to the result for creeping flow, where:

$$c_d = \frac{24}{Re}. \tag{4.28}$$

At the higher Reynolds numbers, the formula (4.27) stabilizes at $c_d \approx 0.14$.

4.3.2 Drag coefficient under unsteady motion

When the relative velocity between the fluid and the particle changes, unsteady drag models must be employed to account for the dynamic interaction between the particle and the fluid. Dynamics of forces acting on particles with variable velocities were initially explored in [10], following research like [52, 51, 39, 58]. Mathematical formulation of the Lagrangian acceleration of a spherical particle, moving with Lagragian velocity, in an unsteady flow is given with the Basset–Boussinesq–Oseen equation (BBO equation) as the sum of the viscous, gravitational, buoyancy, virtual mass, and Basset forces acting respectively on the particle. Assuming low particle acceleration ($a_p << 1$), Navier-Stokes equation is solved by disregarding inertial acceleration terms. Resulting equation of the drag force exerted on the sphere then takes form:

$$
\begin{aligned}
m_p \cdot \frac{dv_p}{dt} = & \underbrace{m_f \left(\frac{Dv_f}{Dt} - \nu \cdot \Delta^2 \cdot v_f \right)}_{F_1} \\
& \underbrace{- m_f \cdot \frac{1}{2} \cdot \frac{dv_r}{dt}}_{F_2} \\
& \underbrace{- 6 \cdot \pi \cdot d_p \cdot \mu \cdot v_r}_{F_3} \\
& \underbrace{- 6 \cdot \pi \cdot r_p^2 \cdot \mu \int_{-\infty}^{t} \frac{\frac{dv_r}{d\tau}}{\sqrt{\pi \cdot \nu \cdot (t - \tau)}} d\tau}_{F_4} \\
& \underbrace{+ (m_p - m_f) \cdot g}_{F_5} .
\end{aligned}
\tag{4.29}
$$

in which ν represents kinematic viscosity, d_p is material particle diameter, μ represents dynamic viscosity, m_p is the mass of the material particle, m_f is the mass of the fluid corresponding to the particle volume, g is the acceleration vector of gravitational force, τ is the variable of pseudo-time and t is arbitrary point in time. This expression embodies Newton's second law of motion, where the left side denotes the particle's linear momentum rate of change and the right-hand side is the summation of forces acting on the particle. In equation (4.29), F_1 represents pressure gradient force which originates from the integration of normal and shear stresses acting over the particle surface

$$
F_1 = m_f \cdot \left(\frac{Dv_f}{Dt} - \nu \cdot \Delta^2 \cdot v_f \right). \tag{4.30}
$$

Term F_2 represents added mass force. The added mass force emerges due to the inertia of the fluid that is displaced by the particle's motion

$$
F_2 = m_f \cdot \frac{1}{2} \cdot \frac{dv_r}{dt}. \tag{4.31}
$$

Stokes' force is represented with right side term F_3, which provides a measure of the viscous drag for low Reynolds numbers, characterizing the resistance encountered by the particle's shape

$$
F_3 = 6 \cdot \pi \cdot d_p \cdot \mu \cdot v_r. \tag{4.32}
$$

Term F_4 represents Basset force that accounts for the transient effects of viscosity, capturing the influence of the boundary layer's evolution on the particle surface. It specifically addresses the temporal lag in the boundary layer's development when there is a change in the relative velocity between the particle and the fluid (4.19).

And finally, term F_5 represents buoyancy force one the moving particle

$$F_5 = \left(m_p - m_f\right) \cdot g. \tag{4.33}$$

Oseen [52] provided a detailed analysis of the drag coefficient for a sphere experiencing variable velocity. In this paper drag coefficient is decomposed into three distinct components: the drag coefficient for a sphere moving at a constant velocity, an additional drag coefficient accounting for velocity variations, and the Basset term, which represents the historical effects of velocity changes on drag. Total drag force of settling particle with variable velocity can be calculated like:

$$F_D = F_d + F_m + F_b = \frac{1}{2} \cdot \rho_f \cdot c_d \cdot A_p \cdot v_r^2 + k_m \cdot V \cdot \rho \cdot \frac{dv_r}{dt} + k_b \cdot \rho \cdot A_p \cdot \int_0^t \frac{f(t-\tau)}{\tau^{0.5} d\tau}, \tag{4.34}$$

where F_d is drag force of a sphere with constant velocity, F_m is additional mass force and F_b is Basset force. It can be observed that for constant velocity or $dv_r/dt = 0$, both F_m and F_b are equal to zero. Thus, equation (4.34) becomes:

$$F_d = \frac{1}{2} \cdot \rho_f \cdot c_d \cdot A_p \cdot v_r^2. \tag{4.35}$$

In the following chapter a description is presented for the drag model used for the purposes of this research.

4.4 Drag model for MP particles transported in fluid

Accurately modeling the drag force on particles, particularly microplastics, in fluid streams is a complex task. By combining theoretical models, empirical correlations, and experimental data, a comprehensive model can be formulated [62]. The proposed model was used to compute the drag coefficient using experimental data acquired from the particle trajectories. The settling velocity of a particle in a fluid is influenced by both fluid properties (density and viscosity)

and particle properties (density, size, shape, and surface texture). The functional relationship between these factors is generally not well quantified. Hence, empirical curves derived from laboratory experiments are typically proposed. When a particle is introduced into a Newtonian fluid with lower density, it will experience an initial acceleration driven by its own weight. The fluid's resistance to deformation, which is transmitted to the particle through surface drag and pressure disparities across it, generates forces that resist the particle's movement. These forces depend on the velocity and the acceleration of the particles [56].

Disregarding the particle and fluid movement in the lateral axis y (perpendicular to both vertical axis and fluid flow direction axis) allows us to conduct kinematic analysis in two-dimensional, x - z plane. Kinematic functions of a particle in a fluid stream were recorded experimentally. Using the measured accelerations, the experimentally measured force can be expressed in the x direction F_x and z direction F_z.

$$F_x = a_x \cdot V \cdot \rho_f, \tag{4.36}$$

$$F_z = a_z \cdot V \cdot \rho_f, \tag{4.37}$$

where a_z and a_z are experimentally measured particle accelerations, V is particle volume and ρ_f is fluid density. Taking into account the balance of forces in x and z directions it follows:

$$F_x = F_{Dx}, \tag{4.38}$$

and

$$F_z = F_{Dz} - G, \tag{4.39}$$

where F_{Dx} and F_{Dz} are drag force components in x and z axis. By combining Equations (4.38) and (4.39) it follows:

$$F_x + F_z = F_{Dx} + F_{Dz} - G, \tag{4.40}$$

Drag components in x and z axis can be written as:

$$F_{Dx} = \frac{1}{2} \cdot c_{dx} \cdot \rho_f \cdot A_p \cdot v_{rx}^2, \tag{4.41}$$

$$F_{Dz} = \frac{1}{2} \cdot c_{dz} \cdot \rho_f \cdot A_p \cdot v_{rz}^2, \tag{4.42}$$

where c_{dx} and c_{dz} are values of drag coefficients corresponding to the particle orientation in x

and z axis. However, for spherical and quasi spherical particles it follows that:

$$c_{dx} = c_{dz} = c_d. \tag{4.43}$$

It is important to note that, in this case, the mass and Basset forces from (4.34) can be neglected. This is direct results of static water conditions where acceleration is $a = 0$, i.e., there is no change in velocity over time. Therefore, we can express:

$$F_D = F_d. \tag{4.44}$$

Furthermore, expression (4.40) can be written as:

$$c_d \cdot \frac{1}{2}(\rho_f \cdot A_p \cdot v_{rx}^2 + \rho_f \cdot A_p \cdot v_{rz}^2) = (a_x + a_z) \cdot V \cdot \rho_f - G, \tag{4.45}$$

or finally:

$$c_d = 2 \cdot \frac{(a_x + a_z) \cdot V \cdot \rho_f - G}{\rho_f \cdot A_p \cdot v_r^2} \tag{4.46}$$

Reynolds number Re depends on the relative magnitude of the inertial and viscous forces, which can in its local form be written as:

$$\mathrm{Re_p} = \frac{|v_r| \cdot d_p}{\nu}, \tag{4.47}$$

where d is characteristic particle length, v_r is particle velocity relative to fluid velocity, and ν is kinematic fluid viscosity [22].

By capturing the complete particle settling process (namely particle positions $x(t)$ and $z(t)$), which was achieved by video recording and software analysis, and then using the Equations (4.46) and (4.47), it is possible to calculate the local values of the Reynolds number Re_p and drag coefficient c_d along the entire trajectory of a particle. Equation (4.46) can be used for calculation of drag coefficient under unsteady conditions when relative velocity between the fluid and particles changes in time. For static water conditions, and particles sinking at terminal

velocity, i.e. $a_p = 0$, this can be written as:

$$c_d = 2 \cdot \frac{F_r}{\rho_f \cdot A_p \cdot v_r^2}, \tag{4.48}$$

where

$$F_r = G. \tag{4.49}$$

In the engineering practice, this is widely known and used expression for calculation of drag force for practical purposes.

5 Experimental research

In order to further advance the knowledge in the field of particle transport, experimental research is necessary. Generally speaking, the purpose of experimental models is to validate and refine theoretical models and optimize practical applications. Furthermore, experimental approach deepens our understanding of complex systems, providing empirical data that can be used in comparison with theoretical results. Integrated approach, in which experimental findings are combined with numerical modeling, is particularly useful in the field of MP characteristics and transport.

MP particles interact with a variety of environmental variables like water currents, sediment dynamics, and biological organisms. Complexity and high variability of these interactions with different ecosystems make them hard to analyze with purely theoretical models. Experimental research allows for a precise characterization of size, shape and density of MP particles which predominantly influence their transport behavior. Experimental results on the relation between particle geometry and their behavior in flowing water can later be used to enhance analytical and numerical models.

5.1 Experimental setup

The sinking behavior of MP particles in water stream conditions was investigated using an experimental flume (Figure 5.1) of the hydraulic laboratory of the Faculty of Civil Engineering, University of Rijeka. The channel, measuring 12.5 m in length, features a rectangular cross-section with dimensions of 309 mm in width and 450 mm in height. To ensure experiment reproducibility, the flow conditions were regulated and this was achieved by controlling geometric and kinematic factors, specifically the flow discharge, channel slope, and water level. The flow discharge and water level within the flume are managed through a pump and a downstream weir located 12 meters from the flume's start. Notably, the channel's slope has been set to zero.

Figure 5.1: Experimental flume as part of the hydraulic laboratory at the University of Rijeka.

To ensure the control over MP geometry and also to achieve the repeatability of the experiment, a high-precision 3D printer was used for the production of MP particles. This printer boasts a precision capability of up to 32 microns and can create samples with a minimum size of 0.4 mm. Additionally, the 3D printer was utilized to fabricate a dosing ramp designed for introducing particles into the water stream. It ensured that particles entered the measurement zone without added linear or angular momentum, i.e. enabling for the particle momentum to be exclusively gained from the fluid (Figure 5.2). Constant flow conditions within the flume were maintained using an inlet pump and a 350 mm high weir positioned 7.5 meters downstream from the dosing ramp. This setup has resulted in a consistent water depth of 415 mm along the channel section designated for particle tracking, measured from the bottom of the flume.

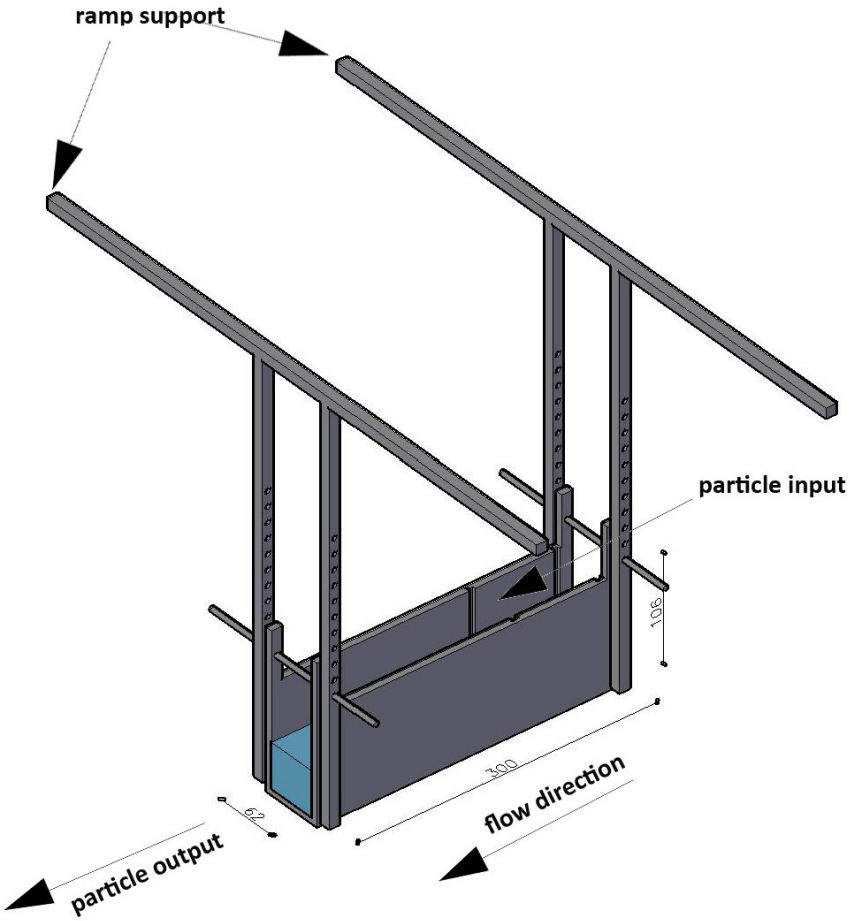

Figure 5.2: A 3D sketch of dosing ramp used for inserting particles into water stream (dimensions in mm)

Particle positions during sinking process were tracked using video equipment. The videos of each experimental run were recorded at 30 frames per second in UHD (ultra-high definition) video quality using a Samsung A53 camera (Samsung Electronics Co.Ltd., Suwon, South Korea). The camera was positioned at a distance of 2.4 meters from the flume and was aligned perpendicularly to the glass wall of the flume. Remote management of the camera was employed to minimize external influences caused by manual handling. The analysis of the experimental runs for each MP particle shape was conducted using the Open Source Computer Vision Library (OpenCV), leveraging the Python module of OpenCV version 4.5.5. The video analysis involved extracting particle trajectories and sinking times (Figure 5.3).

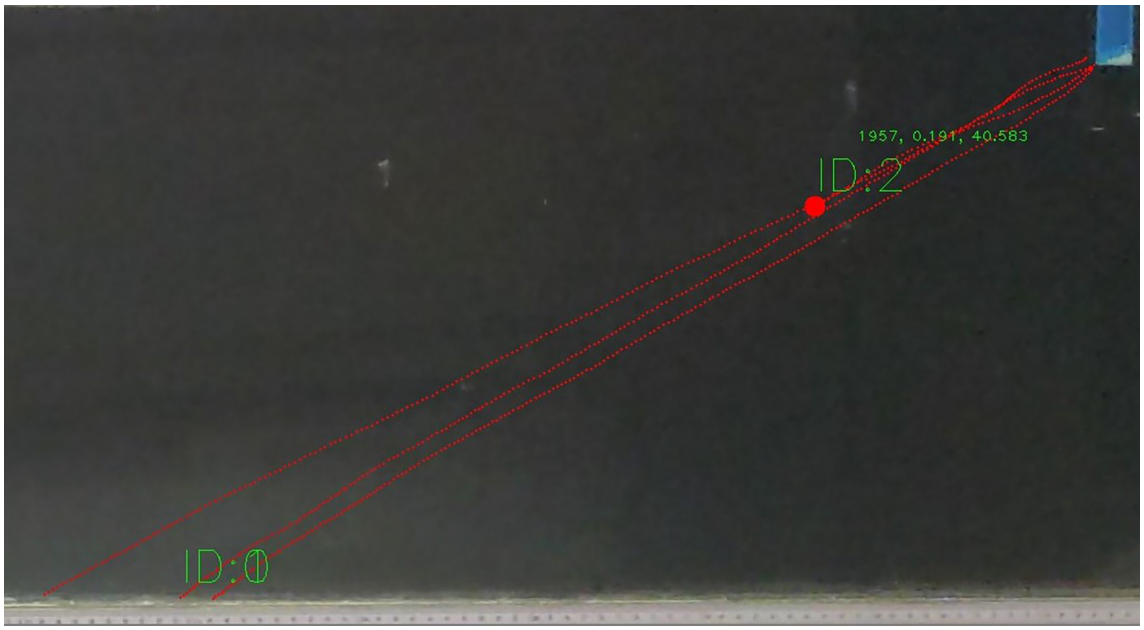

Figure 5.3: OpenCV motion detection of MP particle trajectories in experimental flume. IDs and coordinates of MP particles, together with time stamps, are shown in green text, whereas red dots represent particle trajectories

Particle position extraction was achieved through the utilization of the Mixture of Gaussians 2 (MOG2) background subtractor algorithm, specifically employing the createBackgroundSubtractorMOG2 function for motion detection. This function allows the identification and delineation of shadows present in the background model, indicative of the motion exhibited by the MP particles. In the analyses, the length of the history parameter for MOG2 remained constant at 100 across all evaluations. However, the varThreshold parameter, ranging from 300 to 800, was adjusted based on the size of the MP particle. Smaller values were allocated to smaller shapes. This parameter signifies the pixel-to-model distance, determining whether a pixel aligns sufficiently with the background model. OpenCV code in python with the definition of history and varTreshold parameters in the motion detection model is presented below.

```
frame_width = int(cap.get(3))
frame_height = int(cap.get(4))

out = cv2.VideoWriter('./out.mp4',cv2.VideoWriter_fourcc('m', 'p',
   '4', 'v'), 30, (frame_width, frame_height))

object_detector = cv2.createBackgroundSubtractorMOG2(history=100,
   varThreshold=500)
```

Due to the experimental conditions, it was necessary to conduct parallax correction to remove visual discrepancies caused by changes in camera position or perspective, as well as refraction of light when it passes through water and glass of the channel walls. Parallax occurs when foreground objects shift relative to the background when viewed from different angles, creating an illusion of depth or distortion in the video. This correction is used to ensure that particles detected in the channel are properly positioned in the x-z plane. For the parallax correction, control points were used with the exact position previously measured so that they could be used to calibrate the OpenCV settings. Python code for particle position correction is given below.

```
def pixelToX(px, px_min, px_max, py, py_min, py_max):

    px_ = px / np.abs(px_max - px_min)
    py_ = py / np.abs(py_max - py_min)
    xmin = 5.45
    xmax = 6.23
    ymin = 0
    ymax = 0.345
    dx = np.abs(xmax - xmin)
    x = xmin + dx * (1 - px_)
    dy = np.abs(ymax - ymin)
    y = ymin + dy * (1 - py_)
    return x, y

x_t = [5.405, 5.705, 6.105, 6.305, 6.705, 6.9, 7.30, 7.70]
px_ = [3840, 3340, 2710, 2410, 1810, 1525, 920, 300]
y_t = [0.405, 0.38, 0.31, 0.24, 0.17, 0.1, 0.03, 0]
py_ = [0, 65, 165, 265, 365, 465, 565, 605]

interp_x = intp.interp2d(px_, py_, x_t, kind='linear')
interp_y = intp.interp2d(px_, py_, y_t, kind='linear')
```

In all conducted experiments, flow rate in the channel was 72 m³/h, water depth at the point of measurement was 41 cm, and average flow velocity was 1.57 m/s. The entire experimental scheme is represented in Figure 5.4.

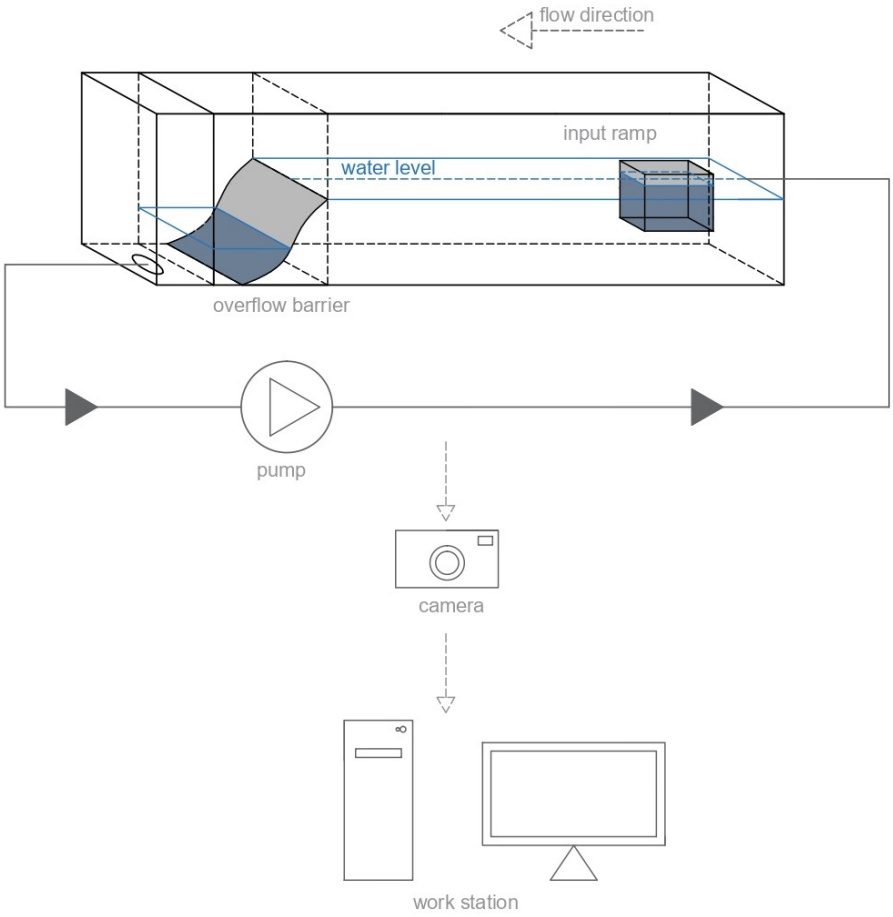

Figure 5.4: Schematic representation of the experimental tool used.

5.2 Particle characteristics

Six different shapes of MP particles were printed for this experiment: sphere (type A), tetrahedron (type B), cube (type C), octahedron (type D), dodecahedron (type E) and icosahedron (type F) as shown in Figure 5.5. Particle size is defined by measuring the greatest distance between two material points of the particle d_p. The density of the plastic material used to print the samples is 1185 m³/h. The density of the particles is higher than the density of water since they are non-buoyant particles. Also, the density of the particles was chosen taking into account the standard MP densities used in the industry.

Figure 5.5: 3D models of MP particles (left to right): particle groups B, C, D, E, and F

Printed particles are housed in a supporting material that has been removed prior to the further particle treatment (Figure 5.6). The support material is water soluble and was removed using a solution of acetone and water to obtain smooth particles for experiment.

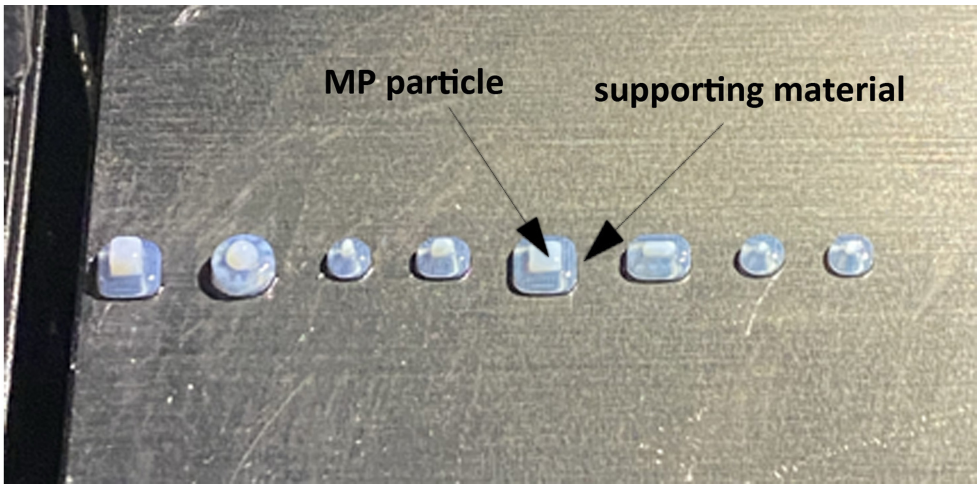

Figure 5.6: Example of printed MP particles (white) in the supporting material (semi-transparent).

For particle type A, the characteristic length d_p is the radius of the sphere. For particle types B to F, d_p is represented by greatest distance between two material points. By the size of the

characteristic length d_p, the particles were divided into four size groups, which were of equal size for all shapes. MP particle sizes used in previous experimental research were 0.5 to 5 mm in [41], 0.3 to 5 mm in [66] and 0.1 to 5 mm in [67]. The regarded experimental scenario of particles sinking in a water stream imposes the need to ensure a sufficient available length of the channel so that all used MP particles can sink to the bottom of the flume before they reach the weir at the channel end. In light of this, and considering the available length of the channel and the fact that the shape and size of MP particles affect the sinking time and trajectory, the MP particle sizes d_p chosen for this experiment were 1.5, 2.0, 2.5 and 3.0 mm. The chosen dimensions meet the condition that all MP particles are deposited within the length of the flume.

It is reasonable to expect some deviations in the kinematic behaviour of the MP particles sinking process recorded within the experiment. Deviations occur due to (i) the perturbations in the initial conditions as per varying initial amount of motion, (ii) local fluctuations of the water velocity, (iii) micro-imperfections of the MP samples geometry, and (iv) other influences due to the measurement accuracy. For this reason, conclusions for a particular type of particles must be formed on the basis of a statistical analysis, which imposes the need to test a larger number of particles. A total of 30 particles of each shape and size were printed and used to conduct the experiment.

5.3 Velocity field

To calculate the local Reynolds number Re_p, it is necessary to know the difference between the velocity of the particle and the velocity of water (4.47). Therefore, it is required to determine velocity field for the water flowing in the experimental flume. For this purpose, a numerical simulation of the flow inside the flume was performed using OpenFOAM software (version v2012).

Numerical domain is a rectangular channel with dimensions of 10.0 m in length, 0.5 m in width, and 0.3 m in depth, in order to replicate the experimental hydraulic channel. Boundary conditions were applied according to experimental settings: inlet with a uniform velocity, outlet with a zero-gradient pressure condition, walls with no-slip conditions, and the top surface with a free-slip condition for open water flow. The mesh, generated using the blockMesh utility in OpenFOAM, consists of 1,067,208 hexahedral cells, with refinement near walls and regions of high velocity gradients.

The resulting velocity field obtained by the numerical model was compared with the results

of the experimental measurements, which were collected using a Nortek Vectrino velocimeter (Figure 5.7). The Vectrino is an advanced acoustic velocimeter designed to accurately measure three-dimensional water velocity variations in a highly localized area, with sampling rates reaching up to 200 Hz. It can be used in diverse settings, ranging from hydraulic laboratories, where it is considered essential equipment, to open ocean environments. It excels in measuring near-boundary flows and capturing highly dynamic phenomena in closed hydraulic system.

Measurements were conducted at three specific positions in the flow direction relative to the entrance ramp: Position 1, situated 0.5 m upstream of the dosing ramp; Position 2, located 0.5 m downstream of the dosing ramp; and Position 3, situated 1.5 m downstream of the dosing ramp. At each of these positions, measurement was performed on a total of 7 vertically distributed points in the central axis of the flume (vertical points at a distance of 5 cm from each other, starting with a point at 5 cm from the bottom of the flume). The comparison of velocity profiles is given in (Figure 3). Due to technical limitations of the Vectrino device, the flow velocity near the bottom could not be measured, so it was linearly extrapolated, conforming to the bottom no-slip condition.

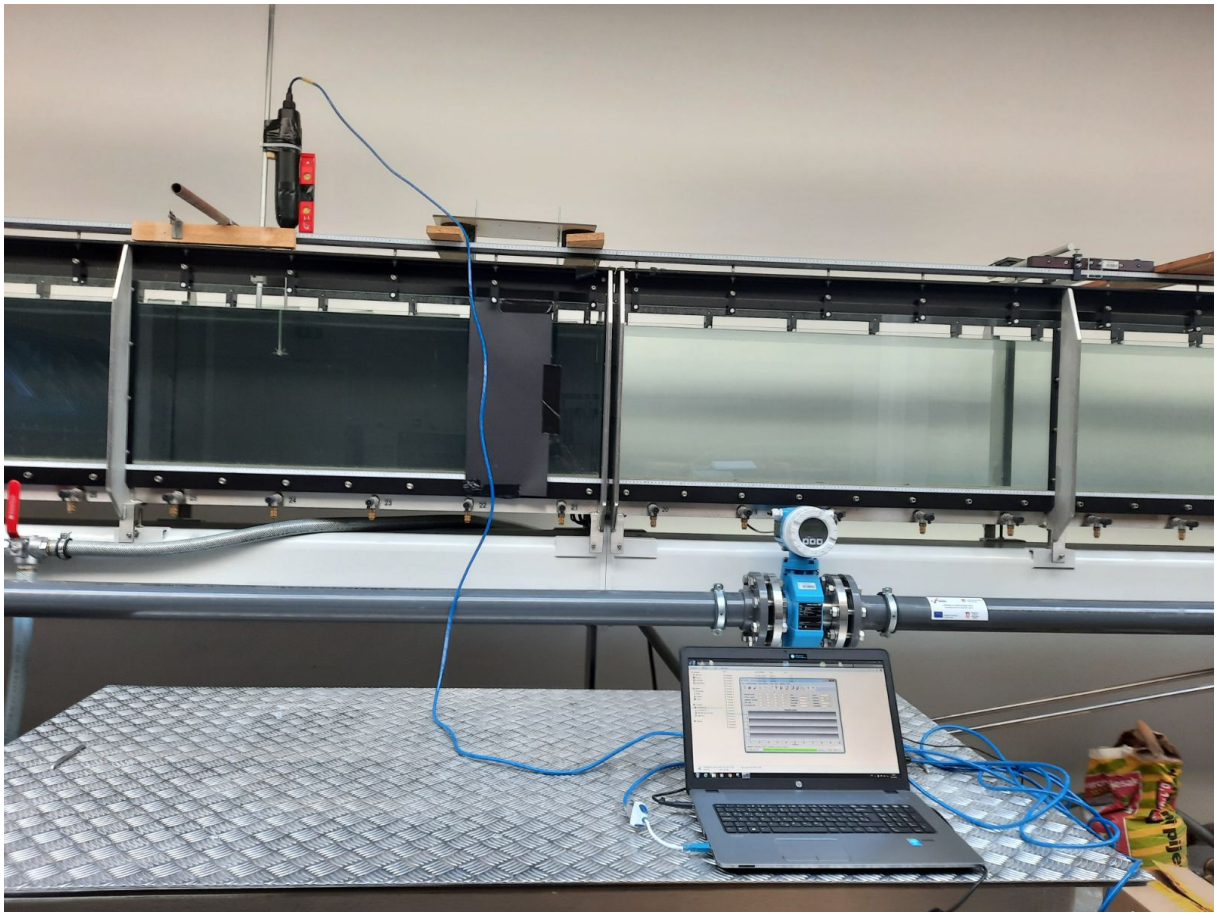

Figure 5.7: Measuring the velocity field inside experimental flume with Vectrino velocimeter.

From the data obtained with the numerical model and the experimental measurements, it can be observed that the differences between the measured and computed velocity values are smaller than the standard deviation of the measurements (Figure 5.8, Table 5.1).

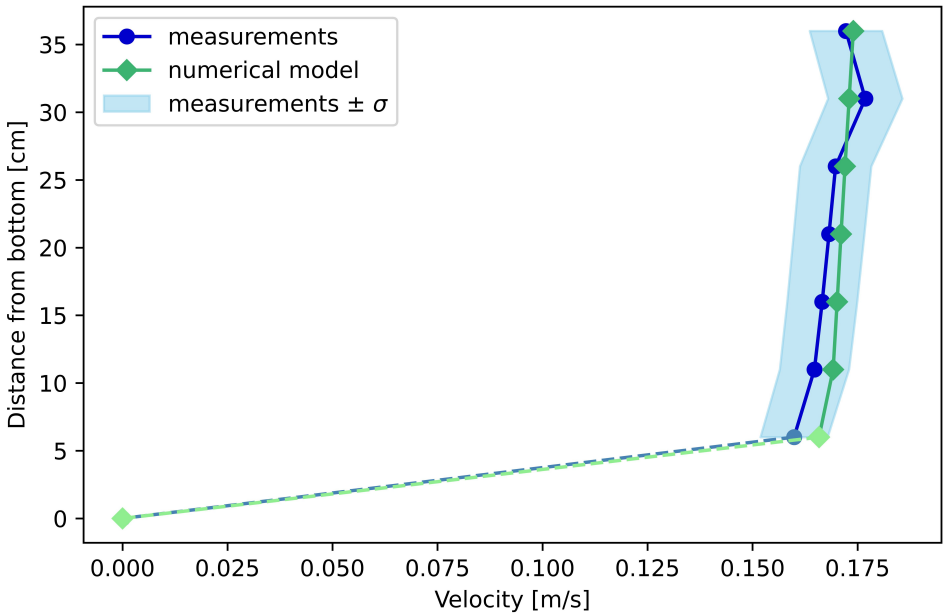

Figure 5.8: Comparison of the velocity profiles obtained by the numerical model and the experimental measurements.

Due to the fact that the discrepancies between the velocity measurements and numerical model are within the limits of standard deviation, the estimation of the particle drag coefficient was conducted by using the velocity field obtained with the OpenFOAM numerical model, it being much more detailed and comprehensive.

Distance from Bottom [cm]	**Measurements** $v_{f,x} \pm \sigma$	**Numerical Model** $v_{f,x}$
36	0.172234 ± 0.00861	0.173998
31	0.176840 ± 0.00884	0.173006
26	0.169773 ± 0.00848	0.172026
21	0.168210 ± 0.00841	0.171069
16	0.166590 ± 0.00832	0.170149
11	0.164735 ± 0.00823	0.169191
6	0.159888 ± 0.00799	0.165824

Table 5.1: Measured and simulated flow velocity in the experimental flume, 0.5 m downstream of the input ramp.

5.4 Experimental results

By systematically recording and analyzing the complete trajectory of a particle during its settling (specifically tracking its positions $x(t)$ and $z(t)$) through video recording and subsequent software processing, it is possible to determine local Reynolds number Re_p and drag coefficient c_d at each point along the particle's path using equations (4.47) and (4.46).

Since the formulas require particle velocities (v_p) and accelerations (a_p), these were analytically derived as the first and second time derivatives, respectively, from the trajectories reconstructed with Bézier curves for all particles within each shape and size group. A Bézier curve is a parametric curve widely utilized in various areas of application. It is defined by a set of discrete control points and a mathematical formulation, allowing the creation of smooth, continuous curves. Bézier curves are particularly useful for approximating complex real-world shapes that lack simple mathematical descriptions. A Bézier curve is specified by a series of control points P_0 through P_n, where n denotes the curve's order (e.g., $n = 1$ for linear, $n = 2$ for quadratic, and $n = 3$ for cubic curves). The curve starts and ends at the first and last control points, respectively, while the intermediate control points typically do not lie on the curve itself. Explicit definition of Bézier curve can be expressed as:

$$B(t) = \sum_{i=1}^{n} \binom{n}{i} (1-t) \cdot t^{n-1} \cdot t_i \cdot P_i, \tag{5.1}$$

where $B(t)$ represents the position of a point on the Bézier curve for a given value of t, $\binom{n}{i}$ are the binomial coefficients, t is dimensionless that ranges from 0 to 1. For $t = 0$, $B(0)$ equals to staring point of the curve, and for $t = 1$, $B(1)$ represent curve ending point. In this research, Bézier curve of the 5$^{\text{th}}$ order was used ($n = 5$) for the interpretation of the particle trajectories with continuous function. Continuous function was necessary for stable calculation of first and second time derivatives (v_p and a_p).

Figure 5.9 shows measured trajectories (blue line on graph) for spherical particles with d_p = 3.0 mm that is divided in 5 parts with red dots representing control points for a Bézier curve. Based on this points, Bézier curve was constructed for trajectories of particles group A to F (Figure 5.10). Blue dots on the graphs represents interpolated points based on Bézier control points (red dots). Number of points have been set as $n = 50$. The values for x and z have been normalized so that the initial point in the x direction is always set to zero, and the terminal point aligns with the final value in the z direction. For spherical particles with a diameter of 3 mm, the

settling time is around 3.5 seconds. The particle trajectory is predominantly linear, exhibiting a slight curvature and minimal fluctuations. Figure 5.11 illustrates the deposition times for a 1.5 mm spherical particle, which are nearly twice as long compared to a 3 mm sphere. This extended settling time is attributed to the hydrodynamic effects encountered by smaller particles in a flowing water environment. The reduced effective gravitational force acting on smaller particles results in prolonged settling times and thus longer trajectories through the water stream. Notably, the curve shape of the 1.5 mm particle remains largely consistent with that observed for the 3 mm particles, showing only minimal deviations. In order to model the trajectory curves for each of particle groups with various size and shape, a 5th-order Bézier interpolation was applied on the measured experimental data.

The measured trajectories needed to be statistically stabilized to provide balance with the steady (i.e., time-averaged) flow velocity field used in the formulae and the numerical model. Furthermore, it should be noted that the used experimental measurement technique cannot detect lateral movements of particles (in the direction of the y axis, i.e., orthogonal to the $x - z$ plane), and as a result, particle trajectories are not captured entirely accurately. Additionally, trajectories are observed only in the $x - z$ plane; therefore, the condition of balance of forces is not fully satisfied. There are also limitations of the particle tracking method precision manifesting through the discretization of the measured trajectories in the spatial and temporal domain, as well as through the imperfections of the OpenCV video analysis of the particle motion.

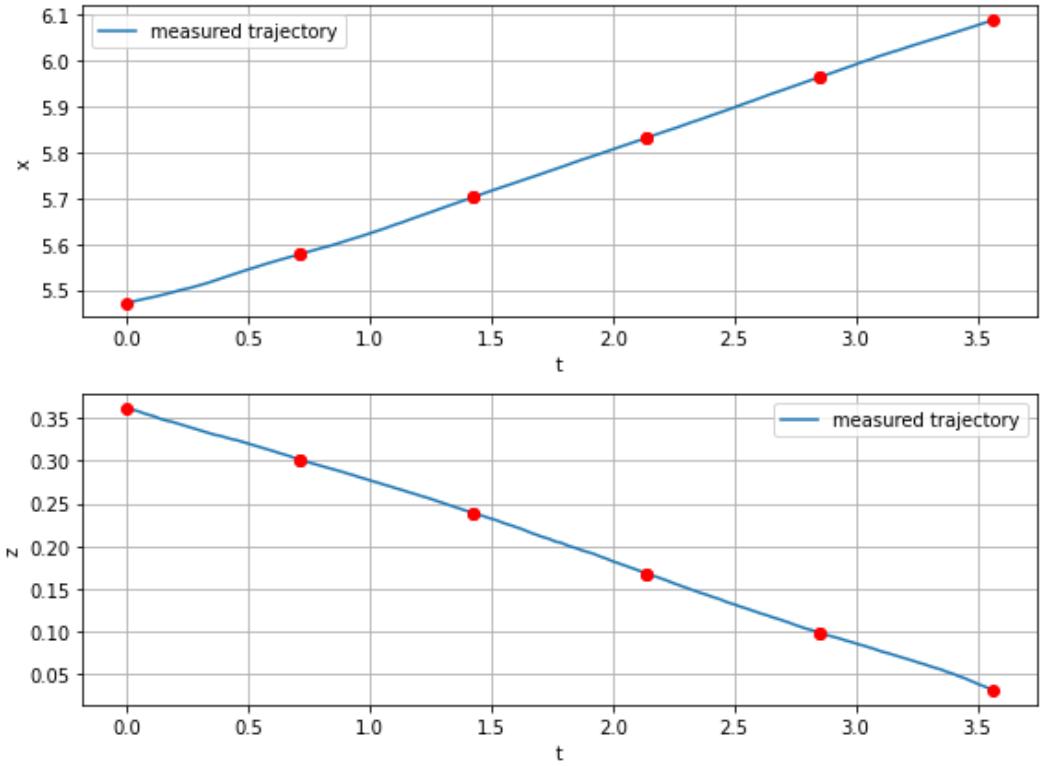

Figure 5.9: Measured trajectories for sphere MP particles of size $d_P = 3.0$ mm: $x - t$ graph (upper plot) and $z - t$ graph (lower plot).

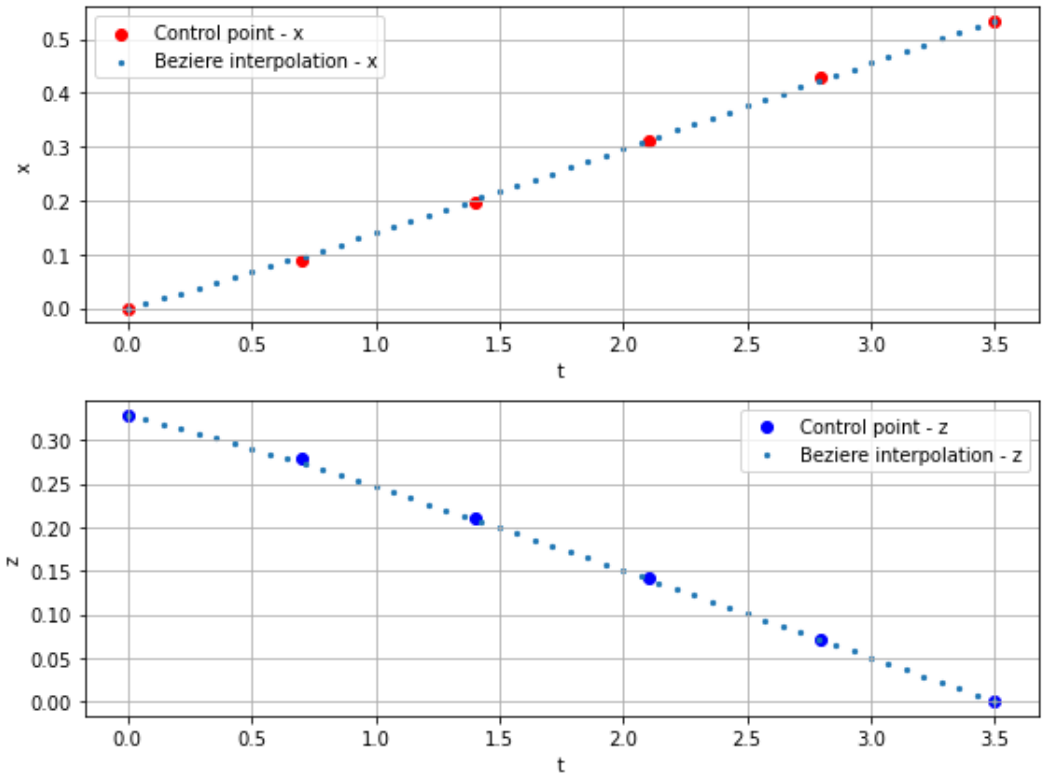

Figure 5.10: Bézier curve with $n = 5$ for spherical MP particles of size $d_P = 3.0$ mm: $x - t$ graph (upper plot) and $z - t$ graph (lower plot).

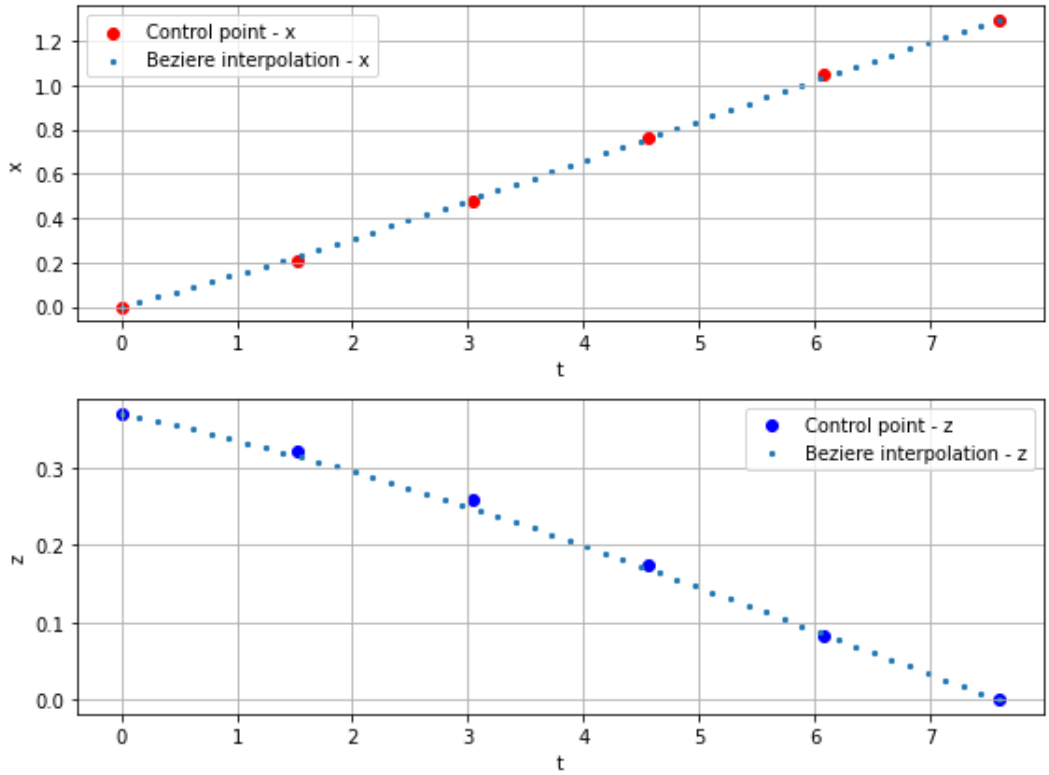

Figure 5.11: Bézier curve with $n = 5$ for spherical MP particles of size $d_P = 1.5$ mm: $x - t$ graph (upper plot) and $z - t$ graph (lower plot).

Particle velocity v_p components were calculated as first time derivative (Figure 5.12), and acceleration a_p as second time derivative of the trajectory curves, as shown in Figure 5.13. Both graphs represent results for one spherical particle with size $d_p = 3.0$ mm and will be used as demonstration of the method used in this research. Velocity in x-axis v_{px} has a convex form, it increases until the time point $t \approx 3$, after which it decreases until the end of the particle movement. The decrease in the final part can be explained as a result of the influence of the bottom of the experimental flume and boundary layer. Corresponding acceleration a_{px} at point $t \approx 3$ equals zero and becomes negative until the particle settles to the bottom. Vertical velocity component v_{pz} has a concave curve shape due to orthogonal orientation since the particle is falling along z-axis. The velocity values in the x direction (v_x) are an order of magnitude greater than those in the z direction. This observed difference indicates that adding horizontal flow velocity component into the experimental setup significantly influences the settling time and the resultant particle trajectory. Previous experiments described in the literature were conducted in a static system with a single water column, but introducing horizontal flow alters the dynamics, affecting how particles settle and move through the fluid.

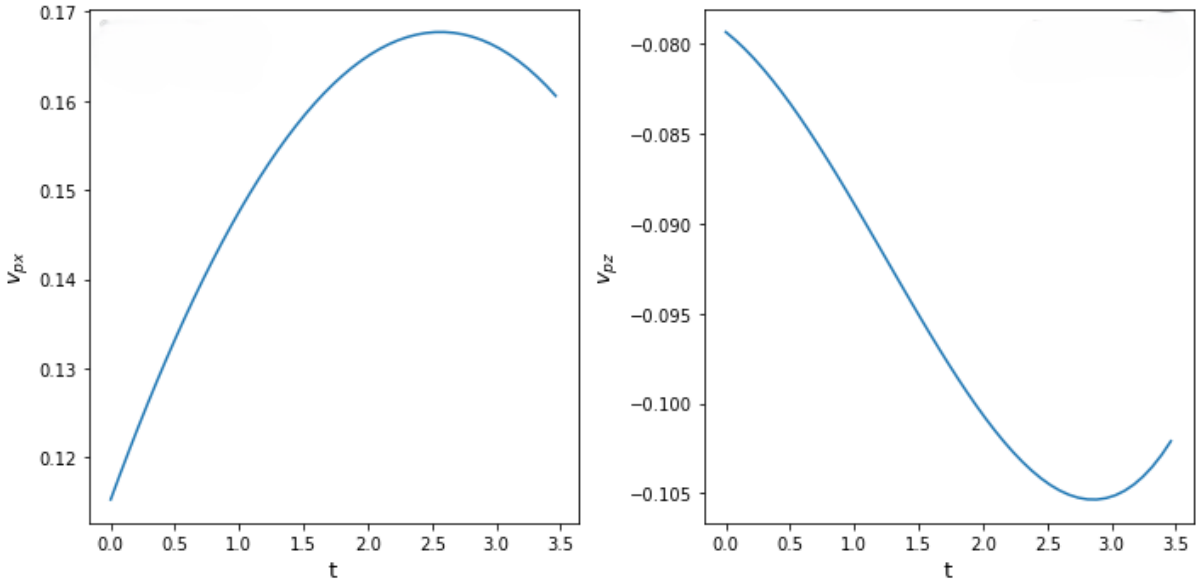

Figure 5.12: Comparison of particle velocity in x and z axis: horizontal velocity v_{px} (left) and vertical velocity v_{pz} (right) for spherical MP particles with size d_p = 3.0 mm.

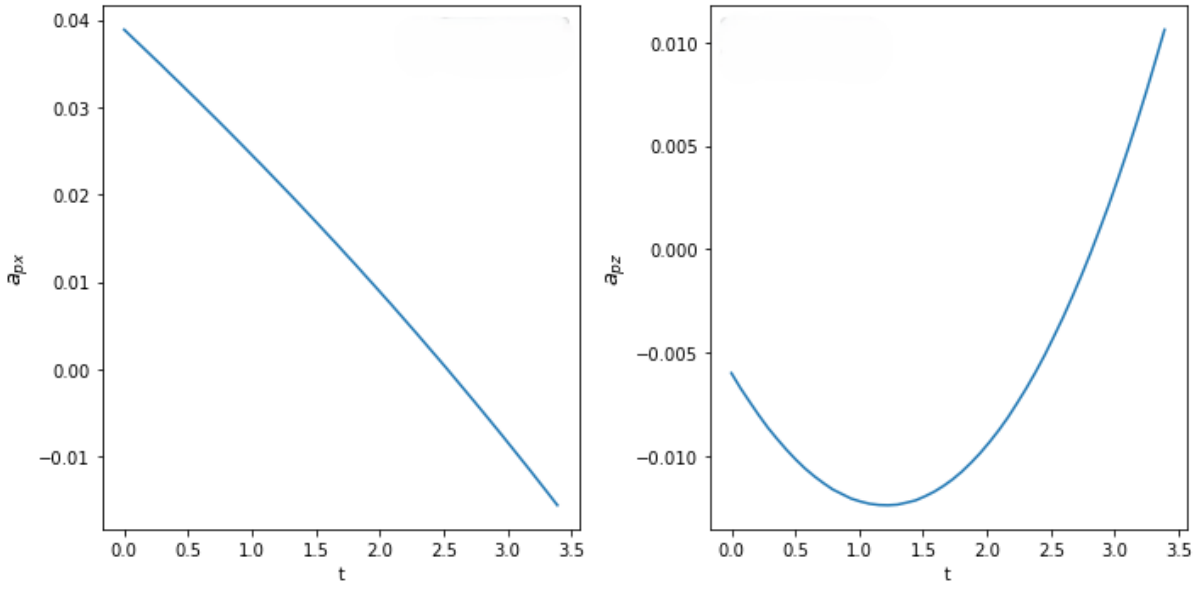

Figure 5.13: Comparison of particle acceleration in x and z axis: horizontal accelereation a_{px} (left) and vertical acceleration a_{pz} (right) for spherical MP particles with size d_p = 3.0 mm.

Based on the expressions (4.36) and (4.37), both forces in the x and z direction can be calculated during the particle settling process. The time-dependent behavior of this forces is illustrated in Figure 5.14 for F_x and Figure 5.15 for F_z. As the particle settles,both F_x and F_z decrease on pair with the particle's vertical position, $z(t)$. These forces are linked to the particle accelerations a_{px} and a_{pz}. It can be observed that the value of the force in z direction is approximately two orders of magnitude greater than that of direction, primarily due to the gravitational influence in the vertical (z) direction. At the start of particle motion, both the drag and lift forces are at their highest values. As the particle continues to settle, these forces gradually decrease.

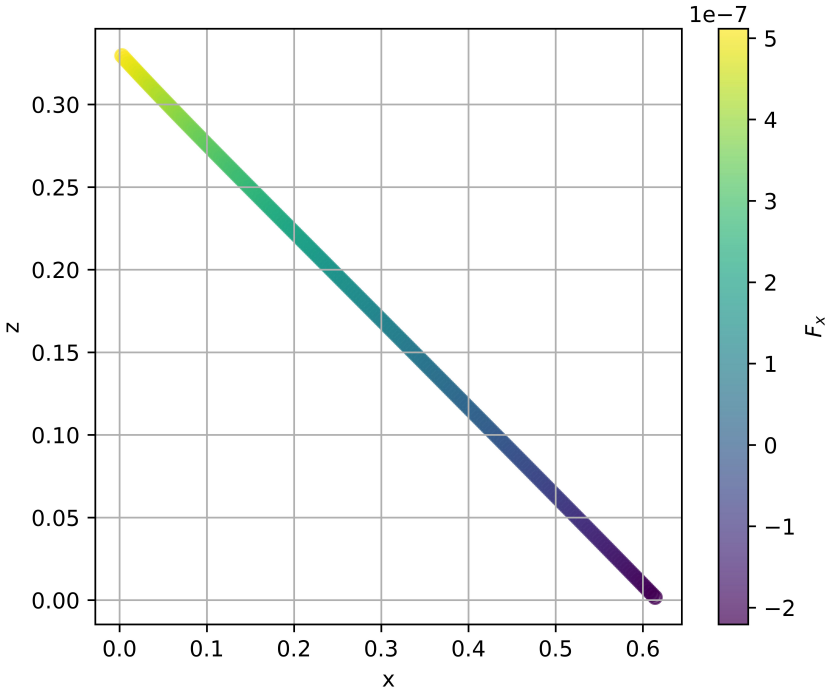

Figure 5.14: Graphical representation of F_x in x-z plane for spherical MP particles with size d_p = 3.0 mm.

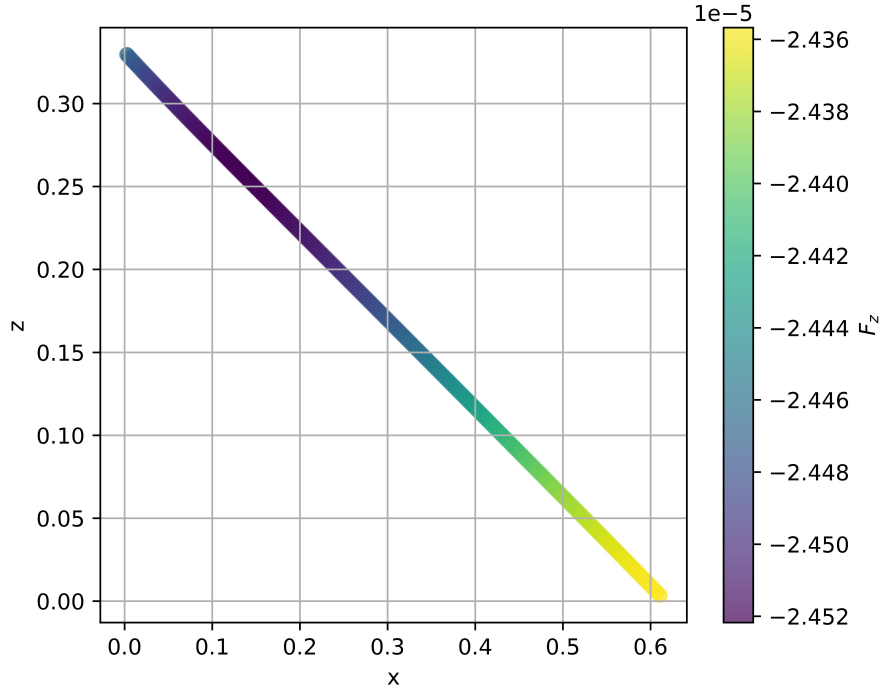

Figure 5.15: Graphical representation of F_z in x-z plane for spherical MP particles with size d_p = 3.0 mm.

Finally, the local particle Reynolds number Re_p and the drag coefficient c_d are calculated using the expressions given in (4.47) and (4.46). The variation of the particle Reynolds number with respect to the channel depth is presented in Figure 5.16. As shown, Reynolds number increases with water depth (z coordinate) of the channel increases, confirming the observed variations in the particle's relative motion through the fluid. Variations in the Reynolds number values are within the limits of ±10 %, which is why it can be concluded that there are no significant changes in the flow conditions along the trajectory. On the other hand, the drag coefficient c_d, which is illustrated in Figure 5.17, demonstrates a decreasing trend over time as the particle sinks. This results highlight the dynamic behaviour of the drag force acting on the particle in relation to its variable velocity and position within the fluid flow. In continuation with the described approach, a drag model was constructed based on experimental results for MP particles of different sizes and shapes.

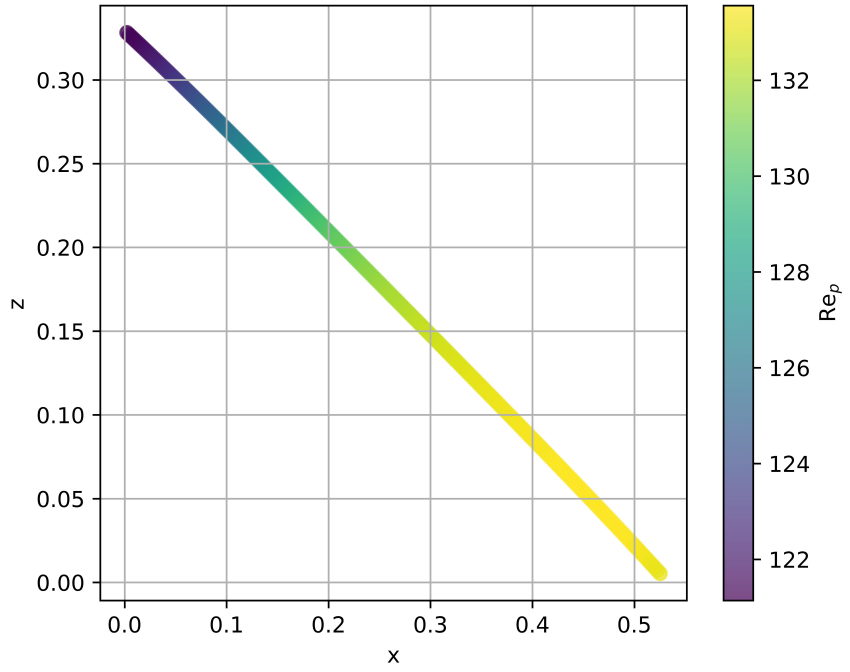

Figure 5.16: Graphical representation of local Reynolds number Re_p in x-z plane for spherical MP particles with size d_p = 3.0 mm.

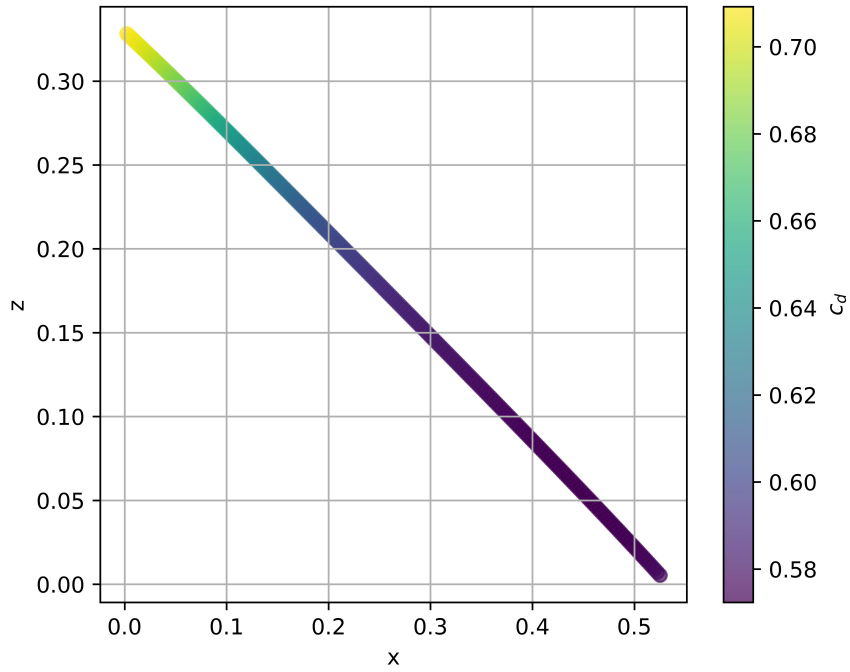

Figure 5.17: Graphical representation of local drag coefficient c_d in x-z plane for spherical MP particles with size d_p = 3.0 mm.

The c_d(Re) values were calculated for particle shapes A to F and particle sizes ranging from 3.0 mm to 1.5 mm. The values were obtained based on data average values, that is, for the trajectories obtained with Bezier curves. Trajectory-based c_d(Re) values for spheres, derived from the experimental data, were compared with previously reported results [24, 36, 35] for validation. Figure 5.18 shows the relationship between the drag coefficient (c_d) and the Reynolds number Re for spherical particles of various particle sizes. It can be observed that for each individual particle size there is a separate curve on the c_d(Re) plot which can be constructed by connecting the corresponding points. Specifically, the red points represent measured values for spheres with diameter (d_p = 1.5 mm), green points for (d_p = 2 mm), blue points for (d_p = 2.5 mm), and light blue points for (d_p = 3 mm). These points represent c_d(Re) values for every time point along the recorded particle trajectory. According to previous studies, the calculation of the drag coefficient in flow with variable velocity primarily depends on the Reynolds number and the particle acceleration [72, 52]. Results presented in Figure 5.18 show good agreement with previous results for a sphere with variable velocity [72]. In order to ensure the practical application of the experimental research in engineering practice, further analysis was conducted for time segments with constant velocity.

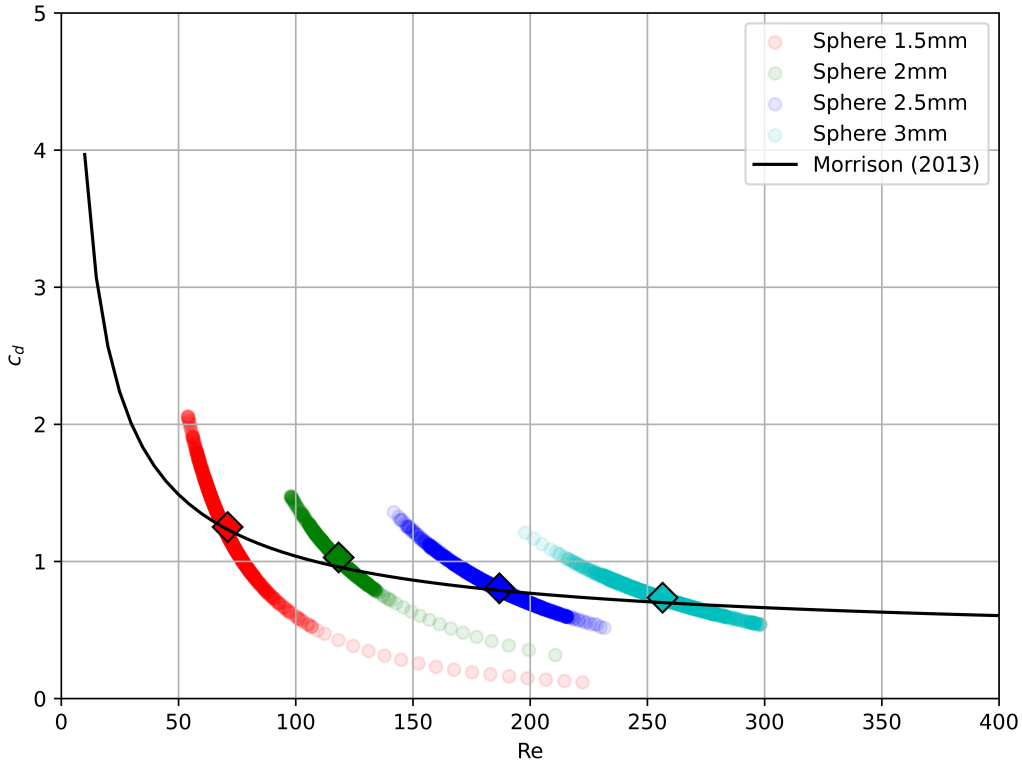

Figure 5.18: Graphical representation of c_d(Re) relation for spherical particles whit sizes d_p = 3 mm (light blue), d_p = 2.5 mm (dark blue), d_p = 2.0 mm (green), d_p = 1. 5mm (red).

In order to isolate the segment of particle movement with constant velocity, an additional criterion in the trajectory analysis was introduced. Specifically, analysis was conducted for points where the acceleration is less than 0.0001 m/s^2, ensuring that the particles were moving with negligible acceleration. In that case, the terms of the equation (4.34): F_m and F_b become zero and only the term F_d remains. By implementing statistical analysis, it was shown that the median values for each group of particles lie along the Morrison [24] curve (Figure 5.19). Therefore, mean values were calculated for each of the particle groups taking into account acceleration criterion ($a \approx 0$). The mean values for each particle size are emphasized with diamond markers in the respective colors. This effect is a consequence of the experimental conditions within which there is movement of particles with variable velocity, i.e. where the acceleration is non-zero. As a result, the c_d(Re) values reflect these dynamic changes in particle motion.

In Figure 5.19, the results for spherical particles under this criterion are presented. Here, the measured c_d(Re) for the condition $a \approx 0$ are compared with the theoretical expression as referenced in [24]. The close agreement between the experimental data and the values from the

literature validates the used experimental procedure and confirms the need for using only the constant velocity segment of particle trajectories.

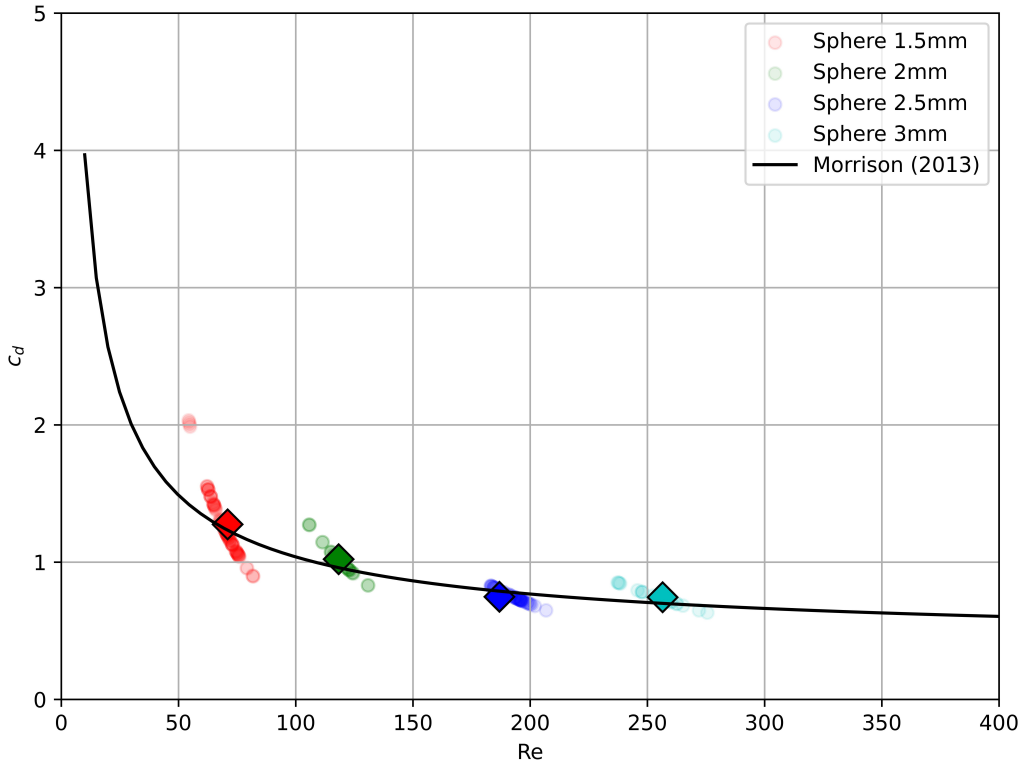

Figure 5.19: Graphical representation of c_d(Re) relation for spherical particles with sizes d_p = 3 mm (light blue), d_p = 2.5 mm (dark blue), d_p = 2.0 mm (green), d_p = 1.5 mm (red) and acceleration $a \approx 0$.

By implementing the analysis presented for spherical particles, this study was extended on the rest of particle shapes used in the experiments. For every particle group, aforementioned condition for acceleration limit was applied in order to avoid variability in velocity along settling trajectory. Additionally, median values were derived for each particle size and shape. Finally, regression functions were proposed within the established Reynolds number range. The respective regression curves for each particle shape are illustrated in Figure 5.20. Table 5.2 presents function curves for each of MP shapes. These expressions can be of practical use as a means of quick approximation of the drag coefficient under known flow conditions. Numerical results for regression curves are presented in Table 5.3. Values that fall outside the range of Re numbers analyzed by the experiment should be approached with caution.

In conclusion, it can be observed from Figure 5.20 that calculated drag coefficients for spher-

ical particles align well with theoretical predictions of Morrison. Calculated values of c_d are in range of 0.74 to 1.28 across Reynolds numbers ranging from 71 to 257. The characteristic concave trend of the c_d(Re) curve is observed across all particle shapes. For cube-shaped particles, the drag coefficients values increase in comparison to spherical particles, which is manifested due to their less efficient hydrodynamic properties. Specifically, the drag coefficients for cubes range from 0.81 to 1.89 with Reynolds numbers between 77 and 272. Notably, particles with tetrahedral and octahedral shapes exhibit even higher drag coefficients. Tetrahedral particles have c_d values ranging from 1.43 to 2.80, with corresponding Reynolds numbers between 55 and 165. Octahedral particles c_d values are in range from 1.43 to 4.07 over Reynolds numbers from 40 to 145. Further, for dodecahedral particles, c_d values range from 1.05 to 2.56 with Reynolds numbers spanning 21 to 104. In adittion, the drag coefficient values for dodecahedrons partially overlap with those of spherical particles, which can be expected due to their closer resemblance to a sphere. In contrast, icosahedral particles exhibit drag coefficients from 0.91 to 3.78, parallel with cube in terms of c_d magnitude. The highest drag coefficients are observed for tetrahedral and octahedral particles. This is consisted with their geometric configurations, which in terms of geometric symmetry, deviate the most from a perfect sphere.

Particle Group	**Shape**	**Regression Function**	**Re range**
B	Tetrahedron - f_2	$1.41 \cdot 10^{-3}\ \mathrm{Re}^2 - 0.043\ \mathrm{Re} + 4.70$	55 ... 165
C	Cube - f_3	$-1.99 \cdot 10^{-7}\ \mathrm{Re}^3 + 1.44 \cdot 10^{-4}\ \mathrm{Re}^2 - 0.0357\ \mathrm{Re} + 3.88$	77 ... 272
D	Octahedron - f_4	$-2.90 \cdot 10^{-6}\ \mathrm{Re}^3 + 1.15 \cdot 10^{-3}\ \mathrm{Re}^2 - 0.156\ \mathrm{Re} + 8.65$	40 ... 145
E	Dodecahedron - f_5	$-5.75 \cdot 10^{-6}\ \mathrm{Re}^3 + 1.59 \cdot 10^{-3}\ \mathrm{Re}^2 - 0.15\ \mathrm{Re} + 6.06$	20 ... 110
F	Icosahedron - f_6	$-1.23 \cdot 10^{-6}\ \mathrm{Re}^3 + 5.52 \cdot 10^{-4}\ \mathrm{Re}^2 - 0.0874\ \mathrm{Re} + 5.94$	25 ... 170

Table 5.2: Numerical representation of regression functions for MP particles regarding shape groups B to F with corresponding Reynolds number range

Interpolated curves presented in Table 5.2 enable easy calculation of the drag coefficient when the flow conditions in the form of Reynolds number are known. The derived c_d(Re) relationships are represented by second- or third-degree polynomial curves, each uniquely defined across the specific Reynolds number range.

To advance their applicability, the given regression formulae should be expanded to incorporate a parameter that characterizes particle shape within the functional dependencies. This can be achieved with multivariable shape analysis, thereby allowing the expressions to be generalized and applied to a broader range of particle geometries. In the following section, the process

of obtaining a regression model based on the used shape parameters, measured data and the optimization process will be presented.

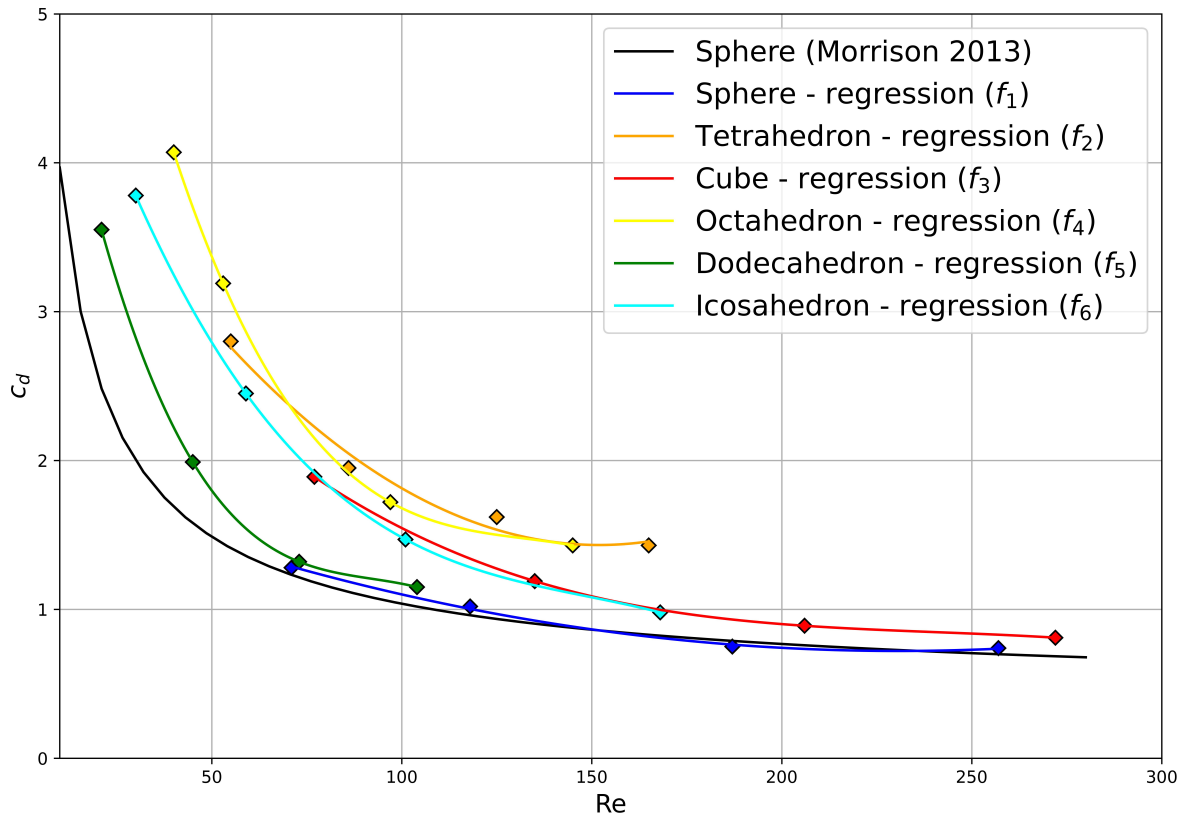

Figure 5.20: Comparison of c_d(Re regression models for various MP shapes, with theoretical values by Morrison $c_d(\mathrm{Re}_p)$ curve for spheres

.

Shape	d_p	c_d	**Re**
Sphere	1.5 mm	1.28	71
Sphere	2.0 mm	1.02	118
Sphere	2.5 mm	0.75	187
Sphere	3.0 mm	0.74	257
Tetrahedron	1.5 mm	2.8	55
Tetrahedron	2.0 mm	1.95	86
Tetrahedron	2.5 mm	1.62	125
Tetrahedron	3.0 mm	1.43	165
Cube	1.5 mm	1.89	77
Cube	2.0 mm	1.19	135
Cube	2.5 mm	0.89	206
Cube	3.0 mm	0.81	272
Octahedron	1.5 mm	4.07	40
Octahedron	2.0 mm	3.19	53
Octahedron	2.5 mm	1.72	97
Octahedron	3.0 mm	1.43	145
Dodecahedron	1.5 mm	3.55	21
Dodecahedron	2.0 mm	1.99	45
Dodecahedron	2.5 mm	1.32	73
Dodecahedron	3.0 mm	1.15	104
Icosahedron	1.5 mm	3.78	30
Icosahedron	2.0 mm	2.45	59
Icosahedron	2.5 mm	1.47	101
Icosahedron	3.0 mm	0.91	168

Table 5.3: Specific c_d and Re values for various MP particle shapes

5.5 Shape based drag coefficient approximation

The results presented above were utilized to develop a regression model for estimating the drag coefficient c_d, based on specific shape parameters. Specifically, particle circularity λ, and particle sphericity Φ, were correlated with the obtained c_d(Re) values across all particle groups. Additionally, the shape factor ψ, defined as the ratio of sphericity to circularity, was also derived and its relationship with c_d(Re) was explored.

First, interpolation is applied to the measured data and they are displayed graphically as a two-dimensional surface. The relationship of sphericity with drag coefficient c_d and Re is shown in Figure 5.21. Additionally, circularity and shape factor correlation with drag coefficient and Reynolds number can be observed in Figures 5.22 and 5.23. Shape parameter values are given on the left vertical axis, while drag coefficient values are represented with a color gradient. The values of the parameters in relation to c_d(Re) are given in Table 5.4.

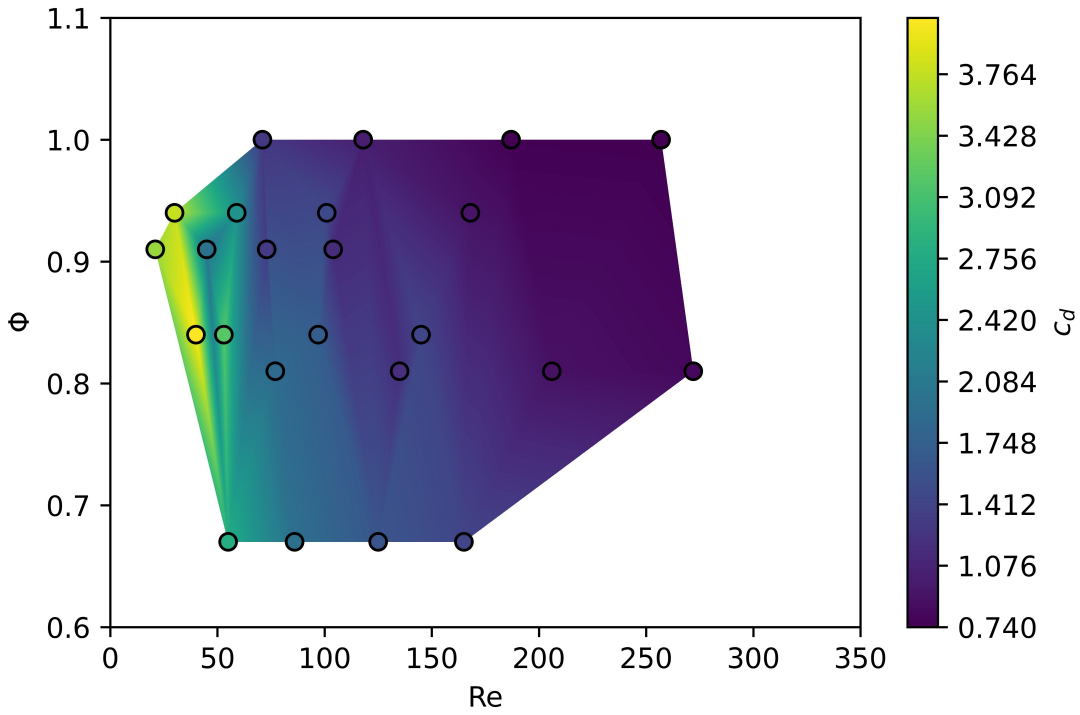

Figure 5.21: Graphical representation of c_d as a function of Re and sphericity Φ

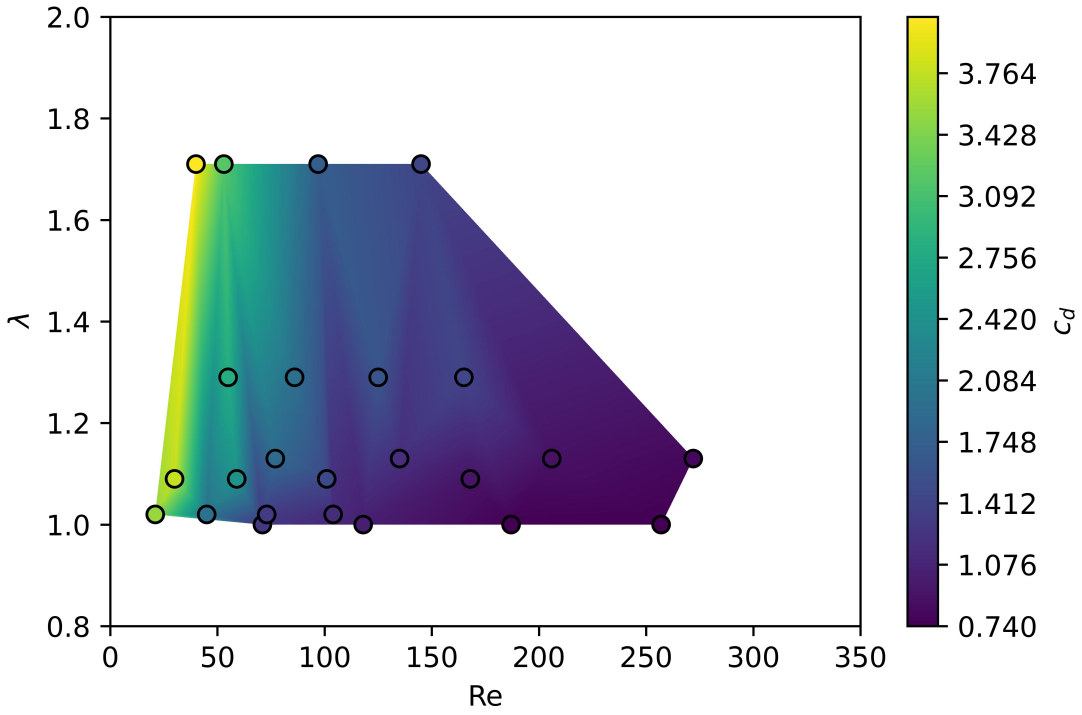

Figure 5.22: Graphical representation of c_d as a function of Re and circularity λ

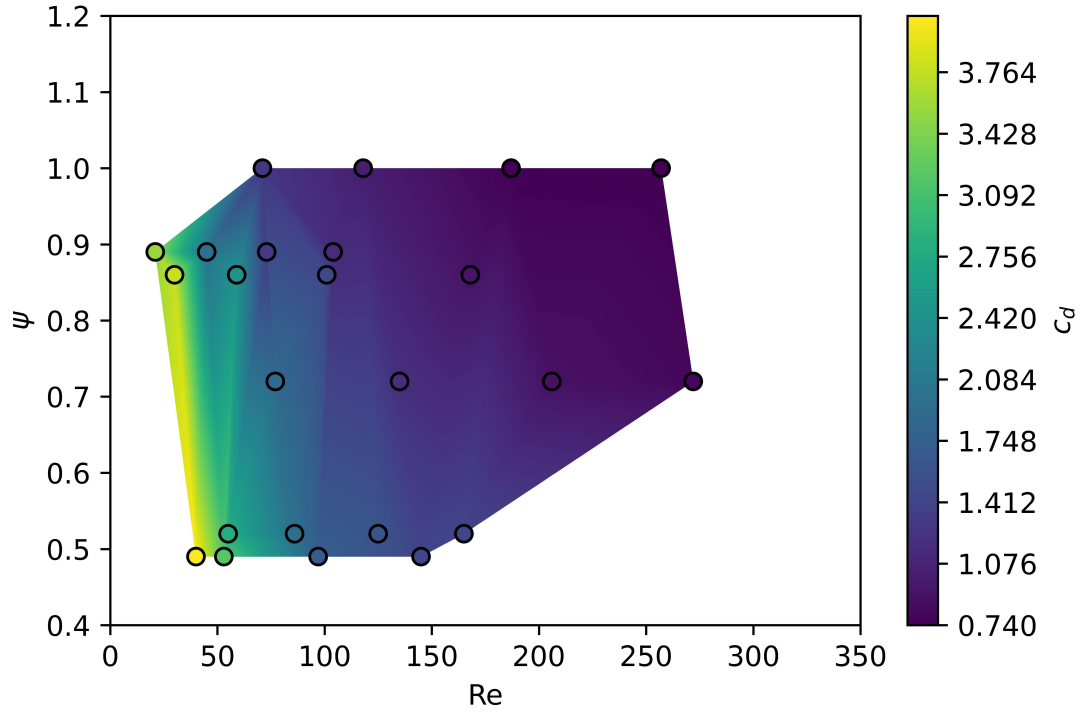

Figure 5.23: Graphical representation of c_d as a function of Re and shape factor ψ

Particle sphericity has a minimum value of 0.67 for tetrahedral shapes with maximum values of 1 for sphere. In contrast, minimum values of circularity are by definition equal to 1 for spherical particles while maximum value is observed to be 1.71 for octahedral shapes. Furthermore, both sphericity and circularity are not influenced by particle size, depending solely on the particle's geometry. In terms of circularity, the drag coefficient c_d increases as the Reynolds number Re decreases. Conversely, for sphericity a minor local instability is observed for values of Reynolds number around 50, where c_d decreases with a reduction in Re. This instability can be mitigated by introducing a shape factor that combines both attributes of sphericity and circularity, as illustrated in Figure 5.23. The shape factor ranges from a minimum of 0.49 for the octahedron to a maximum of 0.89 for the dodecahedron. All of the used shape descriptors have practical applications in the parameterization of MP particles. The choice of the shape parameter is dependent upon the specific problem and the characteristics of the particles under consideration.

Shape	d_p	Φ	λ	ψ
Sphere	1.5 mm	1	1	1
Sphere	2.0 mm	1	1	1
Sphere	2.5 mm	1	1	1
Sphere	3.0 mm	1	1	1
Tetrahedron	1.5 mm	0.67	1.29	0.52
Tetrahedron	2.0 mm	0.67	1.29	0.52
Tetrahedron	2.5 mm	0.67	1.29	0.52
Tetrahedron	3.0 mm	0.67	1.29	0.52
Cube	1.5 mm	0.81	1.13	0.72
Cube	2.0 mm	0.81	1.13	0.72
Cube	2.5 mm	0.81	1.13	0.72
Cube	3.0 mm	0.81	1.13	0.72
Octahedron	1.5 mm	0.84	1.71	0.49
Octahedron	2.0 mm	0.84	1.71	0.49
Octahedron	2.5 mm	0.84	1.71	0.49
Octahedron	3.0 mm	0.84	1.71	0.49
Dodecahedron	1.5 mm	0.91	1.02	0.89
Dodecahedron	2.0 mm	0.91	1.02	0.89
Dodecahedron	2.5 mm	0.91	1.02	0.89
Dodecahedron	3.0 mm	0.91	1.02	0.89
Icosahedron	1.5 mm	0.94	1.09	0.86
Icosahedron	2.0 mm	0.94	1.09	0.86
Icosahedron	2.5 mm	0.94	1.09	0.86
Icosahedron	3.0 mm	0.94	1.09	0.86

Table 5.4: Comparison of sphericity Φ, circularity λ and shape factor ψ for various MP particle shapes

As a further illustration of the potential usefulness of presented models, a new regression model was produced, based on the shape parameters. The models were fitted by use of numerical optimization, namely 8 different optimization functions: Nelder-Mead, Powell, CG, BFGS, L-BFGS-B, TNC, COBYLA and SLSQP. The regression function has a general form of:

$$c_d(\mathrm{Re}, X) = a \cdot \mathrm{Re}^b + c \cdot X^d + e \cdot \mathrm{Re} \cdot X + k \tag{5.2}$$

where X is selected shape parameter and parameters a to k are optimization variables. A total of 24 observed $c_d(\mathrm{Re})$ data points were used in all three cases: sphericity, circularity and shape factor. The regression models were fitted by minimizing the Root Mean Squared Error (RMSE) between the model approximation and experimental data. The calculated values for RMSE are presented in Table 5.5.

Method	RMSE - Sphericity	RMSE - Circularity	RMSE - Shape Factor
Nelder-Mead	0.43575	0.54058	0.60632
Powell	2.01541	13.22811	44.86318
CG	0.37947	0.30321	0.25597
BFGS	0.37175	**0.29848**	0.34731
L-BFGS-B	0.37185	0.32955	0.27400
TNC	0.61901	0.52893	0.63792
COBYLA	0.93648	1.05113	1.07859
SLSQP	**0.2717**	0.32955	**0.24952**

Table 5.5: Comparison of RMSE values for regression models based on sphericity Φ, circularity λ and shape factor ψ

Best results for circularity are given by BFGS method with RMSE equal to 0.2984, for sphericity best method is SLSQP with RMSE equal to 0.2717 and for shape factor best method is SLSQP with RMSE equal to 0.2495. Resulting expressions are obtained by implementing optimization parameters a to k into the formula (5.2). Resulting expressions for circularity, sphericity and shape factor are as follows:

$$c_d(\mathrm{Re}, \lambda) = 27.17634 \cdot \mathrm{Re}^{-0.59838} + 255.05187 \cdot \lambda^{0.00759} - 0.00025 \cdot \mathrm{Re} \cdot \lambda - 255.49643\,, \quad (5.3)$$

$$c_d(\mathrm{Re}, \phi) = -19.26033 \cdot \mathrm{Re}^{0.08570} + 30.54575 \cdot \phi^{-0.09834} + 0.01262 \cdot \mathrm{Re} \cdot \phi - 2.00000\,, \quad (5.4)$$

$$c_d(\mathrm{Re}, \Psi) = -92.25780 \cdot \mathrm{Re}^{0.02211} + 100.00000 \cdot \Psi^{-0.02203} + 0.01250 \cdot \mathrm{Re} \cdot \Psi + 2.50000\,. \quad (5.5)$$

The regression plots were generated using the `contour` function from the Python library. Final regression models are presented in Figures 5.24, 5.25, and 5.26. The experimentally measured drag coefficient values are also shown on these plots. Values of drag coefficients are shown using color gradient on the right. Generally speaking, the plots show strong agreement between the empirical data points and the regression model. Furthermore, the plots highlight a systematic decrease in the drag coefficient (c_d) as the Reynolds number (Re) increases. Slightly larger deviations are present in the zone of Re < 50, which is zone where c_d values increase exponentially with change in Re. This deviation is expected considering the fine variations and sensitivity of the experimental procedure.

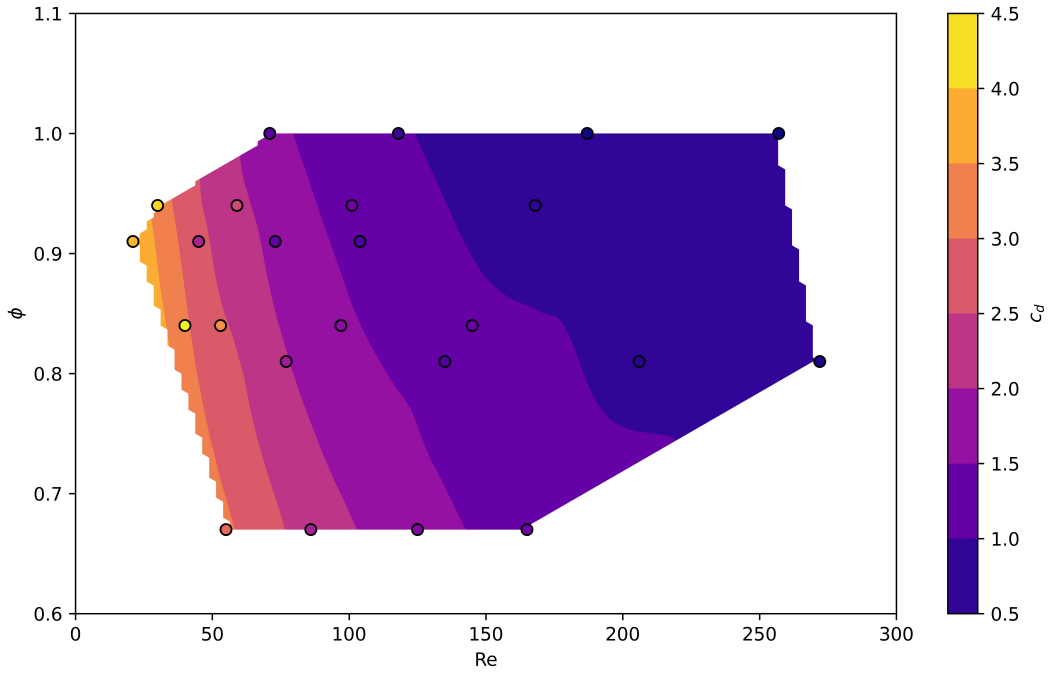

Figure 5.24: Graphical representation for regression model where c_d is a function of Re and sphericity ϕ.

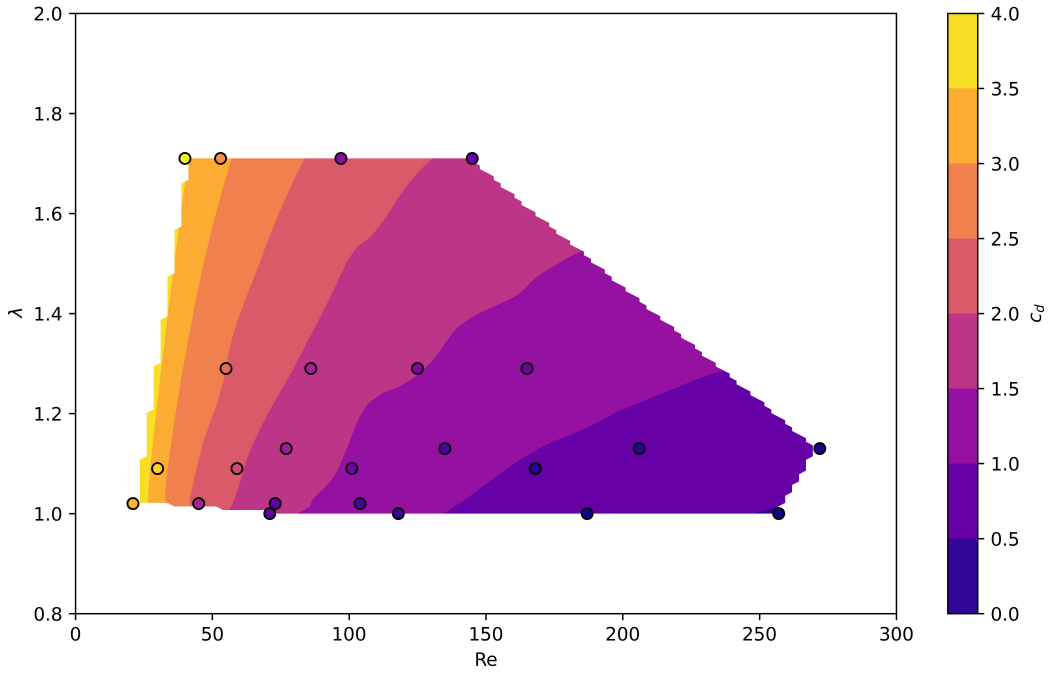

Figure 5.25: Graphical representation for regression model where c_d is a function of Re and circularity λ.

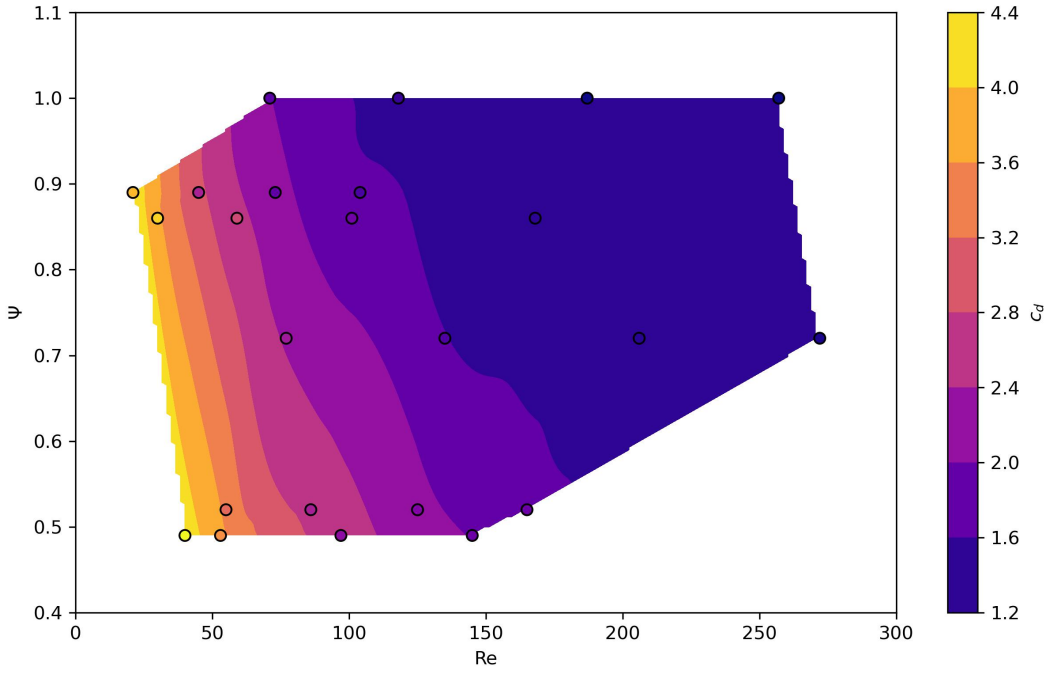

Figure 5.26: Graphical representation for regression model where c_d is a function of Re and shape factor Ψ.

Formulas in (5.3), (5.4) and (5.5) should be used only for the presented range of Reynolds number Re and values of shape factors Φ, λ and ψ.However, using the regression models gives additional practical value to the experimentally obtained data. Such dimensionless shape parameterization enable the analysis of transport properties of different MP particle shapes, regardless of their size.

The approach presented in this study allows practical calculation of the drag coefficient, and consequently resistance force, for particles whose shape can be quantified based on the standard shape parameters. The proposed models ((5.3), (5.4) and (5.5)) can be a useful tool for defining the dynamic properties of MP when solving practical engineering problems of MP transport. Future research should consider the use of additional shape descriptors for various types of MP particles, as well as examine the behavior of MP particles in a wider range of flow conditions represented by a wider range of Reynolds number.

6 Numerical analysis

Numerical models are an important tool for simulating complex physical processes, enabling the analysis and prediction of particle behavior in fluid environments. They offer a way to extend the findings of experimental research and explore scenarios that may be challenging to replicate in controlled settings. In this chapter, a numerical model is developed to simulate the transport of MP particles, replicating the experimental setup to validate its effectiveness. This approach provides a deeper understanding of particle dynamics and facilitates the extension of results to a broader range of environmental conditions. The methods and findings presented here connects experimental observations with predictive numerical techniques, contributing to a more detailed analysis of MP behavior in water systems.

6.1 Numerical model

In order to expand our understanding on MP particle behavior in fluid stream, numerical simulations of particle transport was conducted using OpenFOAM software. OpenFOAM [26] is a free CFD platform that offers various tools to simulate fluid flow and related phenomena. Given the complex nature of MP particle transport, which involves tracking the temporal evolution of particle positions and their interactions with the fluid, a transient solver specifically designed for particle movement simulations was employed for simulations. Consequently, the *icoUncoupledKinematicParcelFoam* solver was selected due to its capability in handling transient, particle-laden flow scenarios. This solver is part of OpenFOAM Lagrangian solvers, which utilize the Lagrangian description to model the motion of discrete particles within a continuous fluid phase. The *icoUncoupled* solver is particularly suitable for this study as it describes the motion of a group of particles (particle cloud), which are suspended in the fluid stream. These particles could represent various scenarios, such as water droplets in a cloud, plastic particles in water, or other types of particles suspended in a fluid. In the context of this study, the fluid is considered incompressible with a steady-state velocity field. This assumption simplifies the simulation while maintaining the essential characteristics of the flow necessary for accurately modeling MP transport. It is important to emphasize that the interaction between the particles and the fluid is unidirectional, i.e. the particles feel the fluid, but the fluid does not feel the particles.

The primary objective of using numerical modeling was to test the feasibility and accuracy of numerically simulating the MP transport and to compare the numerical results with experimentally obtained measurements. By simulating the hydrodynamic behavior and particle interactions within the flume, the study aims to provide a deeper understanding of how MP move and disperse in aquatic environments. Considering the increasing importance of numerical models in engineering practice, this knowledge is important for developing effective strategies to mitigate the impact of MP pollution in water bodies. The results from the numerical simulations conducted as part of this research are expected to offer valuable insights into the mechanisms governing MP transport, validate the numerical model against experimental data, and highlight the potential of using CFD tools like OpenFOAM for studying environmental phenomena involving particulate matter.

6.2 Problem definition

In this section, description is given for the creation of the computational domain and the setup of the flow simulation used to study the transport of MP particles. Model domain was constructed to correspond with the dimensions and specific characteristics of the hydraulic channel used in the experimental analysis. Within this domain, the position and geometry of the dosing ramp, utilized for introduction of MP particles were defined to match properties of laboratory settings. The domain is a rectangular channel with a length of 10 meters, a width of 0.5 meters, and a depth of 0.3 meters. These dimensions were chosen to ensure development of the key flow features while providing required length for particle tracking experiment. Furthermore, at the downstream end, overflow characteristics were set according to experimental overflow geometry and position. A high-quality mesh was generated using the $blockMesh$ utility in OpenFOAM, which allows for structured mesh creation. The mesh consists of total of 1.067.208 hexahedral cells. Mesh refinement was applied near the walls and in regions where high velocity gradients were expected, such as around obstacles and overflow in the flume. This refinement ensures that the flow features are accurately captured, which in turn enables for precise particle tracking. In order to validate the mesh design, a mesh study was conducted by comparing simulation results across different mesh densities. The results showed that additional improvements past the selected mesh density didn't have a significant impact on the results. This indicated that the mesh is detailed enough for the purpose of study. The visualization of the domain and the

simulation results was carried out using the ParaView software (Figure 6.1).

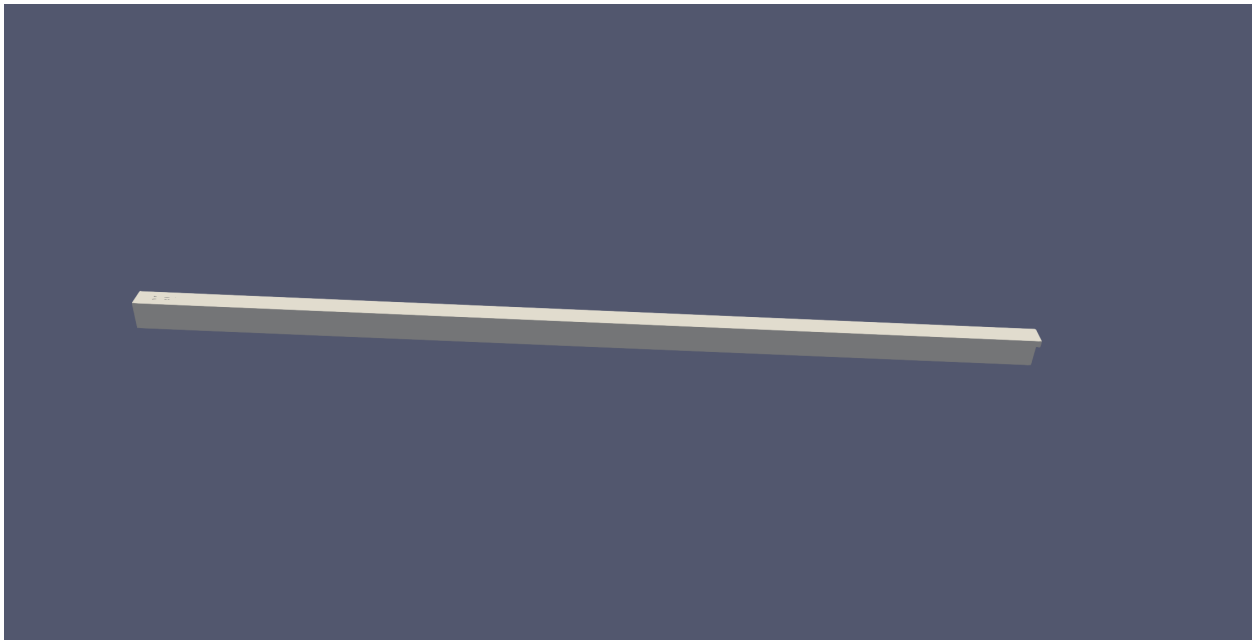

Figure 6.1: Domain of the experimental flume.

Boundary conditions were applied to each boundary of the domain to replicate the experimental conditions:

- Inlet: A uniform velocity profile of 0.17 m/s was applied at the inlet, corresponding to the average flow rate used in the experiments.
- Outlet: A zero-gradient pressure condition was applied at the outlet, allowing the flow to exit the domain freely.
- Walls: No-slip boundary conditions were applied to all walls, ensuring that the fluid velocity at the walls is zero, which simulates the physical interaction between the fluid and the flume boundaries.
- Top Surface: A free-slip boundary condition was used at the top surface to represent an open water surface, allowing horizontal fluid motion without friction.

The numerical simulations were performed with *simpleFoam* solver. *simpleFoam* is specifically designed for solving steady-state turbulent incompressible fluid flow. It employs the SIMPLE (Semi-Implicit Method for Pressure Linked Equations) algorithm, which facilitates the coupling of pressure and velocity fields within the flow to ensure accurate and efficient computation of the fluid dynamics.

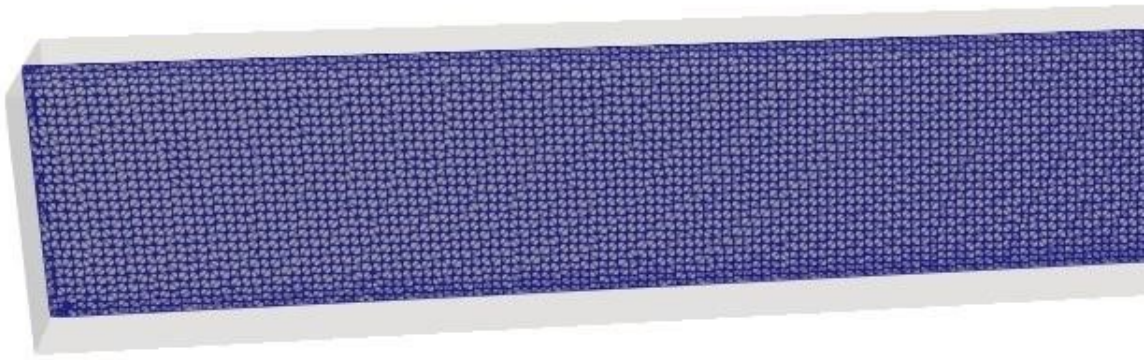

Figure 6.2: A slice of the numerical mesh along the central longitudinal section of the experimental flume.

For single-phase incompressible flows where density is constant, the continuity equation is (4.1) and momentum equation becomes (4.4). The SIMPLE algorithm facilitates the iterative solution of the Navier-Stokes equations for incompressible flow. It begins by setting boundary conditions for velocity, pressure, and other variables. Then, it computes an intermediate velocity field by solving the discretized momentum equation using the current pressure field. Next, the algorithm calculates mass fluxes at the faces of each cell in the computational mesh. It proceeds by solving a pressure correction equation with under-relaxation to adjust the pressure field, stabilizing the solution and aiding convergence. Subsequently, it corrects mass fluxes at cell faces using the updated pressure field to ensure conservation of mass. In the next step, the algorithm adjusts the velocities based on the newly corrected pressure field. Throughout the iterative process, boundary conditions are continuously updated with the latest velocity and pressure data until the solution converges to a satisfactory level. This methodology effectively couples pressure and velocity fields, enabling accurate simulation of fluid dynamics within the computational domain.

Turbulence was modeled by utilizing the ”realizable” k–ϵ turbulence model. To determine the turbulence parameters, a turbulence calculator was used [1]. This calculator requires inputs of the flow velocity, the turbulence intensity, and the turbulent length scale.

The turbulence intensity can be approximated with expression:

$$I = 0.16 \cdot \mathrm{Re}^{-\frac{1}{8}} \tag{6.1}$$

while turbulent length scale can be calculated as:

$$T_{UL} = 0.38 \cdot d_h \tag{6.2}$$

where d_h is width of experimental flume. Obtained turbulence properties are presented in Table 6.1:

Parameter	**Symbol**	**Value**
Turbulence kinetic energy	k	0.0000496282560000 m^2/s^2
Turbulence dissipation	ε	0.00000180009158567 m^2/s^3
Specific turbulence dissipation	ω	0.4030167334235939 1/s

Table 6.1: Resulting turbulence parameters for numerical flow simulation.

The resulting velocity field obtained by the numerical model was validated in comparison with the experimental results measured with Nortek Vectrino velocimeter. Comparison was given in previous chapter by Figure 5.8 with respective values given in Table 5.1. Numerically calculated flow field presented good correlation with experimental measurements. Resulting flow field was utilized in further simulation of MP particle transport behaviour conducted in OpenFOAM.

6.3 Particle transport model

This subsection presents a detailed description of the transport simulation of MP particles using the *icoUncoupledKinematicParcelFoam* solver in OpenFOAM. This solver is specifically designed for simulation of the transient behavior for discrete particles in a fluid, making it appropriate to study the movement and interactions of MP particles within the water flow. The *icoUncoupledKinematicParcelFoam* solver employs a Lagrangian approach to track individual particles as they move through the fluid domain. This method allows for detailed modeling of particle trajectories and interactions with the surrounding fluid. One of the such examples is transport of plastic particles in water. Coupling process between the fluid phase and the particle phase is addressed by solving the Navier-Stokes equations for the fluid ((4.1) and (4.4)) and the force balance equations for the particles separately, ensuring accurate representation of the complex dynamics involved in MP transport. The fluid velocity is assumed to be in a steady-state condition. Therefore, it is calculated initially by solving the conservation equations for

mass and momentum. Particle movements is computed with intergration of Newton's second law over time.

Spatial coordinates and physical properties of the particles are defined within the files *kinematicCloudPositions* and *kinematicCloudProperties*. The initial distribution of MP particles within the domain was set to match the conditions observed in the experimental setup. Particle were introduced in the flume with the dosing ramp which is recreated in the model domain, with properties such as size, density, and shape based on the experimental measurements. The size of the particles ranged from 1.5 to 3 mm. Another particle property that needs to be defined are Young's modulus E and Poisson's ratio ν which are defined as follows:

$$E = 3 \cdot 10^9 \text{ Pa} \tag{6.3}$$

$$\nu = 0.35 \tag{6.4}$$

Within the model, defining the drag coefficient is crucial for accurately simulating the behavior of MP particles. For spherical particles, this is accomplished by selecting the *sphereDrag* option under the *particleForces* settings for the particle cloud model. This selection specifies a drag coefficient model tailored for spherical particles, described by the following formulation:

$$F_d = \frac{3}{4} \cdot \frac{\mu \cdot c_d \cdot \text{Re}_p}{\rho_p \cdot d_p^2} \tag{6.5}$$

$$c_d = \frac{24}{Re_p} \cdot \left(1 + \frac{1}{6} \cdot \text{Re}_p^{2/3}\right), \qquad \text{Re}_p \leq 1000 \tag{6.6}$$

$$c_d = 0.424 \cdot \text{Re}_p. \qquad \text{Re}_p > 1000 \tag{6.7}$$

For the simulation of non spherical particles, drag model is defined as:

$$c_d = \frac{24}{Re_p} \cdot \left(1 + A \cdot Re_p^B\right) + \frac{C \cdot Re_p}{D + Re_p} \tag{6.8}$$

$$A = \exp\left\{\left(2.3288 - 6.4581 \cdot \phi + 2.4486 \cdot \phi^2\right)\right\} \tag{6.9}$$

$$B = 0.0964 + 0.5565 \cdot \phi \tag{6.10}$$

$$C = \exp\left\{(4.9050 - 13.8944 \cdot \phi + 18.4222 \cdot \phi^2 - 10.2599 \cdot \phi^3)\right\} \tag{6.11}$$

$$D = \exp\left\{(1.4681 + 12.2584 \cdot \phi - 20.7322 \cdot \phi^2 + 15.8855 \cdot \phi^3)\right\} \tag{6.12}$$

$$\phi = \frac{A_p}{A_a} \tag{6.13}$$

where A_p is surface area of sphere with the same volume as the particle, A_a is actual surface area of the particle, and ϕ is sphericiy of MP particle.

Additionally, in the context of the particle cloud model, lift force needs to be defined. OpenFOAM provides options for lift definition through two models, specifically the Tomiyama and Saffman-Mei force models. The Tomiyama model is designed for scenarios where the particles are presented as bubbles, necessitating the input of surface tension as a parameter. However, given the application constraints, this model is unsuitable for our scenario. Consequently, Saffman-Mei model was selected, which is intended for accurately modeling the buoyancy forces acting on spherical particles. Saffman-Mei model has a form of:

$$c_l = \frac{3}{2 \cdot \pi} \cdot \frac{1}{\sqrt{Re_f}} \cdot c_{ld} \tag{6.14}$$

$$c_{ld} = \begin{cases} 6.46 \cdot f & \text{if} \quad \alpha \cdot Re_p < 40 \\ 0.338504 \cdot \sqrt{\beta \cdot Re_p} & \text{if} \quad \alpha \cdot Re_p > 40 \end{cases} \tag{6.15}$$

$$Re_f = \frac{\rho_f \cdot \|v_r\| \cdot d_p}{\mu} \tag{6.16}$$

$$\beta = 0.5 \cdot \frac{Re_f}{Re_p} \tag{6.17}$$

$$\alpha = 0.3314 \cdot \sqrt{\beta} \tag{6.18}$$

$$f = (1 - \alpha) \cdot \exp\left\{(-0.1 \cdot Re_p)\right\} + \alpha \tag{6.19}$$

where c_l is lift coefficient, Re_f is fluid Reynolds number and v_{rel} is particle relative velocity. Lift force F_L can be calculated as:

$$F_L = \frac{m}{\rho_p} \cdot \rho_f \cdot c_l \cdot \left((v_f - v_p) \cdot (\nabla \cdot v_f\right) \tag{6.20}$$

The main parameter in defining this model is the sphericity index, which quantifies the deviation of a particle from an ideal spherical shape. The simulation process initially assumes particles to be spherical, and subsequently integrates a non-spherical drag resistance model to these particles. This sequential approach enables the simulation of non-spherical particle behav-

ior. The procedure for defining other particle characteristics remains consistent with that used for spherical particles. Example of defining particle cloud model settings is presented below.

```
subModels
{
    particleForces
    {
        sphereDrag;
        gravity;
    }

    injectionModels
    {
        model1
        {
            type            manualInjection;
            massTotal       0;
            parcelBasisType fixed;
            nParticle       1;
            SOI             0;
            positionsFile   "kinematicCloudPositions";
            U0              (0 0 0);
            sizeDistribution
            {
                type                    fixedValue;
                fixedValueDistribution
                {
                    value 0.003;
                }
            }
        }
    }
}
```

Assumption for transient solvers is that they model the transport or motion of a large particle clouds. Consequently, particle sizes are characterized using a size distribution and maximum possible particle diameter. For a single particle with a known dimensions, it is sufficient to define maximum possible diameter in the solver's framework. This is defined for each of particles groups according to Table 3.3.

Prior to initiating the particle simulation, simulation case has to be prepared by introducing the particles into a pre-established turbulent flow. The initial conditions are derived from a preceding turbulent flow simulation. To achieve this, the solution directory containing the converged turbulent flow results is copied into the directory designated for the transit solver.

```
Evolving kinematicCloud

Solving 3-D cloud kinematicCloud
    34294 move-collide subCycles
Cloud: kinematicCloud
    Current number of parcels       = 1
    Current mass in system          = 1.67525e-05
    Linear momentum                 = (-2.76287e-06 1.46968e-10 -1.58254e-06)
   |Linear momentum|                = 3.18401e-06
    Linear kinetic energy           = 3.02578e-07
    model1:
        number of parcels added     = 1
        mass introduced             = 1.67525e-05
    Rotational kinetic energy       = 0

ExecutionTime = 480.4 s  ClockTime = 480 s

Time = 0.15

Evolving kinematicCloud

Solving 3-D cloud kinematicCloud
    35315 move-collide subCycles
```

Figure 6.3: Example of the one cycle for the *icoUncoupledKinematicParcelFoam* solver

In order to solve equations, OpenFOAM uses finite volume method to discretize the equation. After that, linear system is solved with PISO or SIMPLE algorithm. To ensure the accuracy of the numerical model, the simulation results were validated against experimental data. This involved comparing the trajectories and final positions of MP particles observed in the simulations with those measured in the experiments. Transport simulation and *icoUncoupled* solver was validated based on experimental results for spherical particles. Detailed validation process is presented in following chapter.

6.4 Numerical model validation

In this chapter, validation of the used numerical model against experimental data is presented. For validation purposes, a series of flow simulations were performed in which settling of a single spherical MP particle was simulated (Figure 6.4). These simulations enabled calculation of the drag coefficient, which was compared to experimental measurements. Furthermore, simulated particle trajectories are compared with those recorded in experimental observations. The duration of the simulation was set to 10 seconds. Preliminary control indicated that spherical particles sink within the first 10 seconds and then move along the bottom of the domain in the direction of the x-axis, with no further changes in their dynamics. Thus, for the purposes of

depicting the sinking phase and calculating drag coefficients, a simulation period of 10 seconds has shown to be sufficient.

Figure 6.4: Example of numerical simulation for spherical particle settling in experimental flume (MP particle is marked with red dot). Upper picture represents particle in water stream while bottom one represents settled particle

Drag coefficient is calculated using equation (6.21). For computation of the particle settling velocity, the vertical positions at the start and end of the measurement period must be determined. In the validation simulations referent vertical positions of $z_{start} = 0.3$ m and $z_{stop} = 0.1$ m were chosen.

Using $v_r = v_z$ in (4.48) it follows:

$$c_d = 2g\frac{(\rho_f - \rho_p)\cdot V}{\rho_f \cdot A_p \cdot v_z^2}, \tag{6.21}$$

with average vertical settling velocity v_z of an individual particle being:

$$v_z = \frac{z_{start} - z_{stop}}{t_{stop} - t_{start}}, \tag{6.22}$$

and Reynolds number being defined as:

$$\mathrm{Re}_p = \frac{v_z \cdot d_p}{\nu}. \tag{6.23}$$

Here z_{start} and z_{stop} are the vertical positions of the particles at the beginning and end of the measurement, and t_{start} and t_{stop} are the corresponding times. The characteristic surface area A_p of a spherical particle is defined as:

$$A_p = \frac{d_p^2 \cdot \pi}{4}. \tag{6.24}$$

Table 6.2 presents a comparison between the drag coefficients obtained from the numerical simulation results utilizing the above given calculation and the experimental values. The simulated coefficients are generally within limits of ±10%. This shows the good agreement of the numerical method with the experimental results.

d_p	c_d - OpenFOAM	c_d - Experiment	Percent difference
1.5mm	1.20	1.28	6.25%
2.0mm	0.96	1.02	5.8%
2.5mm	0.73	0.75	2.6%
3.0mm	0.67	0.74	9.5%

Table 6.2: Comparison of the drag coefficient values for spherical particles, obtained from the numerical model and experimental analysis

In the second part of this analysis, particle trajectories from the numerical simulations were compared with those observed experimentally (Figure 6.5). This comparison was performed by analyzing the time-resolved positions for individual MP particles. Results indicated that numerical model successfully captured the general trends of particle movements with deviations in individual particle paths being within acceptable limits.

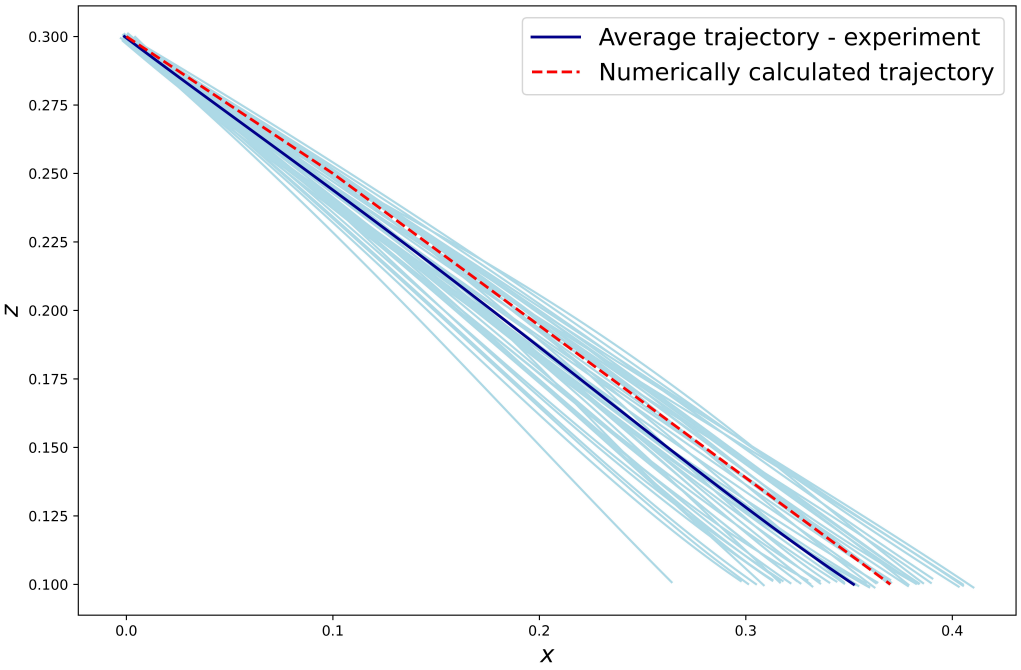

Figure 6.5: Graphical representation of MP particle trajectories (for sphere). Graph shows experimentally measured trajectories (light blue color), averaged experimental trajectories (dark blue) and numerically calculated trajectories (red dotted line)

Simulated drag coefficients show a decreasing trend with increasing particle size, mirroring the behavior observed in the experimental results. Additionally, an inverse relationship between the Reynolds number and the drag coefficient is preserved. The validation results demonstrated that the numerical model can be used to simulate the transport and deposition of MP particles in a controlled flume environment. It should be kept in mind that both experimental and numerical approaches have their own limitations. Experimental analysis has some implicit uncertainties, particularly including particle tracking and velocity measurement techniques. Numerical model on the other hand is based on some fundamental approximations, such as discretization of governing mathematical model and assumptions in turbulence modeling, which could affect accuracy. In light of these remarks, it can be concluded that reasonably strong validation of the numerical model with respect to its capability to simulate MP transport and deposition was obtained.

6.5 Results and discussion

Main motivation of performed numerical simulations was to investigate particle motion within a domain characterized by a developed velocity field, replicating the particle shapes utilized in the experimental procedure. Non-spherical shapes tested experimentally were also simulated using a numerical model, utilizing a non-spherical drag model provided by the software tool. This methodology enabled a comprehensive analysis of particle trajectories and deposition patterns. Consistent with the validation process, the segment between z = 0.3 m and z = 0.1 m was selected as the representative trajectory segment for this analysis, in alignment with the experimental procedure. The simulation results are presented graphically, and recommendations for improving the drag model in OpenFOAM, based on empirical data, are proposed.

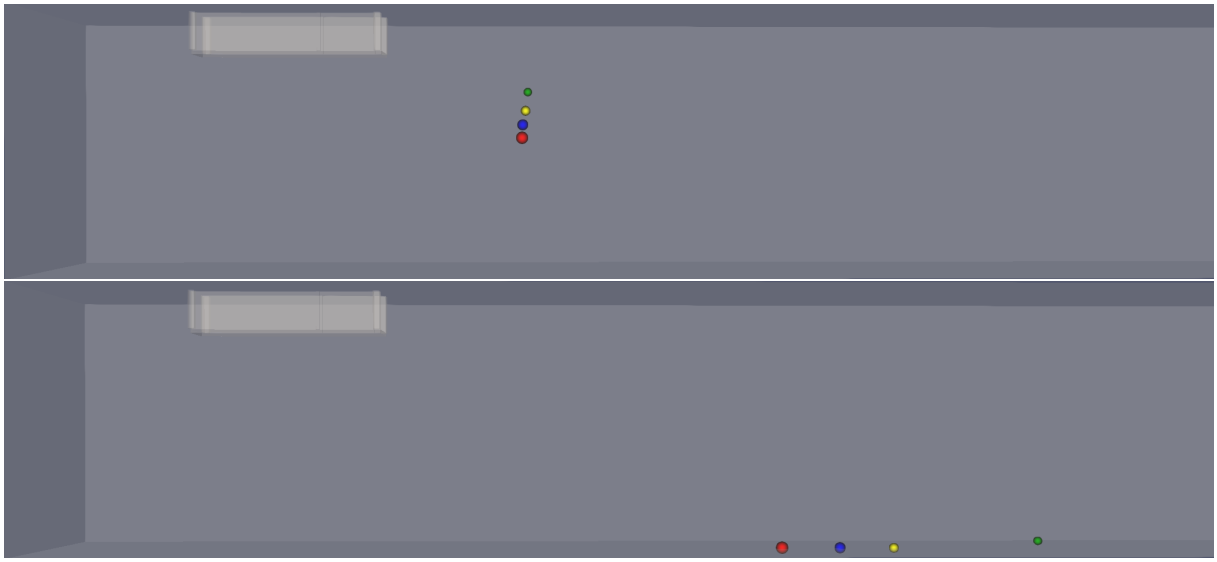

Figure 6.6: Numerical simulation for spherical particles ranging from 3.0 to 1.5 mm for simulation time t = 1.5 seconds and for simulation time t = 5.0 seconds. Sizes of particles are: 3.0 mm (red dot), 2.5 mm (blue dot), 2.0 mm (yellow dot) and 1.5 mm (green dot).

Numerical simulations started with spherical particles with diameters ranging from 1.5 mm to 3 mm. This range of particle sizes was chosen to represent the conducted experimental procedure. Simulations were designed to track the movement and settling behavior of these particles within the flume. Figure 6.6 illustrates the model's results at a moment $t = 1.5$ seconds. Particles are color-coded by size, with the largest particle ($d_p = 3$ mm, red circle) descending the fastest. This visualization highlights the differential settling velocities among the particles, driven by their size. From the bottom to the surface of the water, the particles are arranged according to their size, which is consistent with experimental results, where larger particles exhibit higher settling velocities compared to smaller ones. The observed behavior confirms the model's ability to accurately simulate the settling dynamics of spherical particles in a fluid. Figure 6.6 presents the positions of the spherical particles at $t = 5$ seconds. By this time, all particles have reached the flume bottom, completing their settling process. Simulation provides a clear view of the final deposition patterns and the relative positions of the particles. Relative positioning of the particles remained unchanged throughout the settling process, with the largest particles ($d_p = 3$ mm) settling first, followed sequentially by the smaller particles. The smallest diameter particles ($d_p = 1.5$ mm) were the last to settle, indicating model's ability in capturing the size-dependent settling behavior. This outcome is consistent with theoretical expectations and experimental observations, where particle size directly influences settling velocity.

After successful model validation, numerical analysis was conducted for particles of varying shapes, specifically focusing on non-spherical particles. This part of the study aimed to further expand understanding on how particle shape influences settling behavior within the simulation software. The comparison focused on distinguishing between the *sphereDrag* and *nonSphereDrag* model to accurately represent the drag forces acting on particles of different shapes.

The first step was to compare results for spherical and cubic particles. Both particle types had a characteristic length of $d_p = 3$ mm, ensuring that size was not an influential variable. In order to describe cubic particles, the non-sphere drag model was implemented. More precisely, it is necessary to specify the sphericity index for the cube within the computer program. The simulations were conducted under identical conditions to isolate the effects of shape on settling behavior. Figure 6.7 illustrates the comparison between spherical and cubic particles at $t = 1.0, t = 1.5$, and $t = 2.5$ s. At all of the presented time points, the positions of the particles indicate significant differences in settling rates between the two shapes. The results show that under the same simulation conditions and particle sizes, the cubic particles settle slower than the

spherical particles. This observation is consistent with the theoretical predictions based on the sphericity index. The sphericity (ϕ) of a particle is a measure of how closely its shape approaches that of a perfect sphere. For a sphere, $\phi = 1$, while for a cube, $\phi = 0.806$. The lower sphericity of the cubic particles results in higher drag forces acting on them, leading to a longer settling time compared to the spherical particles. Example of code for non-spherical drag model for cubes is given below.

```
constantProperties
{
    rho0            1185;
    youngsModulus   3e9;
    poissonsRatio   0.35;
}
subModels
{
    particleForces
    {
        nonSphereDrag
        {
            phi 0.806;
        }
        gravity;
    }
}
```

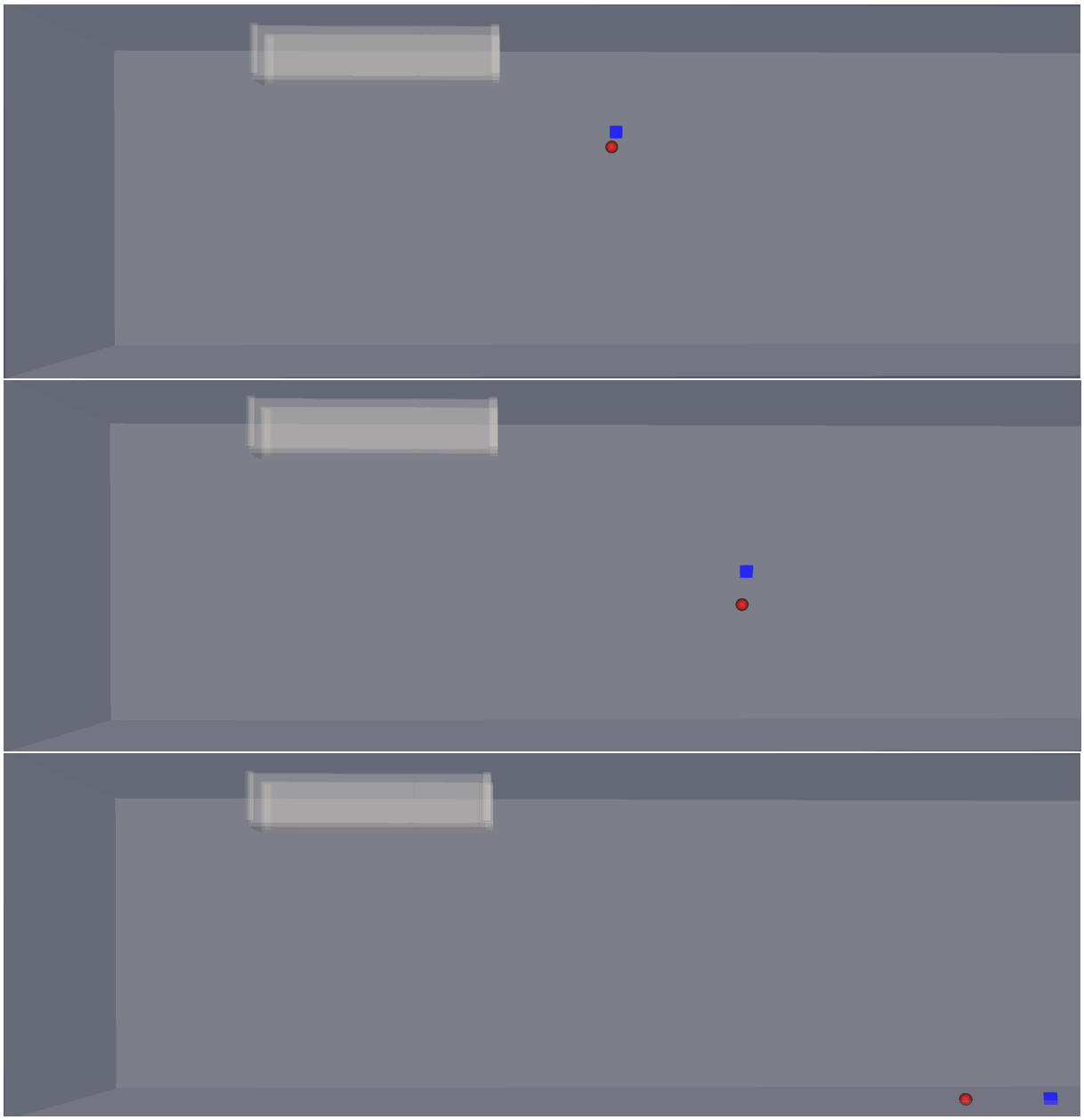

Figure 6.7: Comparison of numerical results for spherical and cubical particles settling in in reconstructed flume domain. Sphere is represented with red dot and cubical particle is represented with blue.

Model results show why it's important to use the appropriate drag models to simulate how MP particles move and settle in water environments. Non-spherical particles, such as cubes, experience higher drag which correlates with their lower sphericity index, resulting in lower settling rates compared to spherical particles of the same size. High level of agreement between numerical simulations and experimental data underscores the validity of the numerical model and the selected drag models for studying particle transport in fluid flows. Figure 6.8 illustrates the positions of cubic particles with diameters ranging from d_p = 1.5 mm to d_p = 3 mm at t = 2

seconds and for cubical particles reaching model bottom. At both time instant, the particles are distributed within the flow field according to their sizes. Simulation results show that the vertical distribution of particles is consistent with their sizes, demonstrating the model's ability to replicate size-dependent settling behavior. Largest particles (d_p = 3 mm, blue cube) are closest to the bottom, reflecting their higher settling velocities due to greater mass and lower drag relative to their size. Sequentially above them are the particles with diameters of 2.5 mm (red cube), 2 mm (green cube), and 1.5 mm (yellow cube). Smallest particles, being the lightest and experiencing the highest drag forces relative to their weight, are closest to the surface at this stage. This distribution aligns with theoretical expectations, where particle settling velocity is a function of particle size and shape. Final arrangement again shows that all particles reached the bottom of the flume, settling in a pattern consistent with their initial size-dependent distribution. largest particles (d_p = 3 mm) settled first, followed by the 2.5 mm, 2 mm, and finally the 1.5 mm particles.

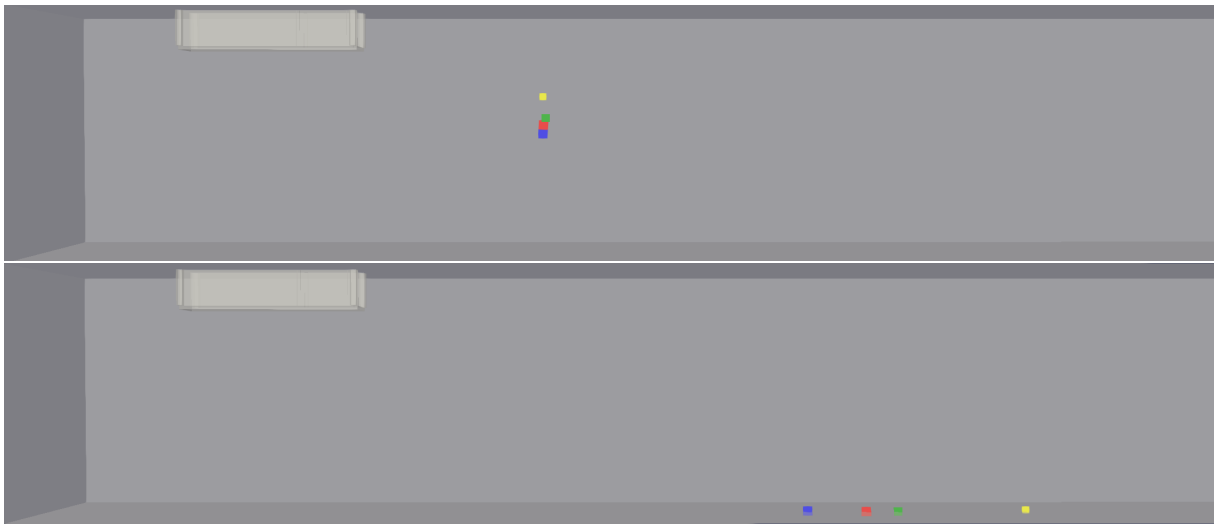

Figure 6.8: Numerical simulation for cubical particles ranging from 3.0 to 1.5 mm for simulation time t = 2.0 s and for simulation time t = 6.0 s. Sizes of particles are: 3.0 mm (blue dot), 2.5 mm (red dot), 2.0 mm (green dot) and 1.5 mm (yellow dot).

Numerical analysis described above was also extended to include other particle shapes used in the experimental procedure: tetrahedron, octahedron, dodecahedron, and icosahedron. For each particle shape, four sizes were tested, with characteristic lengths of 3.0 mm, 2.5 mm, 2.0 mm, and 1.5 mm. Density of all these particles was set to $\rho = 1185$ kg/m^3, consistent with the experimental conditions and uniform across all particle groups. Simulations demonstrated that, similar to spherical particles, particle size significantly influenced the settling behavior for all polyhedral shapes. To capture the complete settling process and ensure all particles had fully settled, the total simulation time was extended to $t = 20$ seconds. This extended duration allowed for the observation of the final deposition patterns and provided a clear comparison of settling times across different shapes and sizes. The behavior of the particles in this case is also in line with expectations. This consistent size-dependent settling pattern was observed across all tested shapes. While particle size was a dominant factor in settling behavior, the shape of the particles also played a significant role. Different polyhedral shapes exhibited varying drag coefficients and hydrodynamic interactions with the fluid flow, leading to differences in settling velocities even among particles of the same size.

Based on the results of the numerical model, particle trajectoriesare extracted from the results of the numerical model. These trajectories were compared with the experimental data to validate the accuracy and reliability of the numerical simulations. Figure 6.5 presents a detailed comparison between the experimentally measured trajectories for $d_p = 3.0$ mm spherical particles (represented by light pale color), the corresponding mean trajectories derived from experimental data (dark blue lines), and the trajectories simulated by the numerical model (red dashed lines). Visual comparison in Figure 6.5 highlights several key observations. Numerical model demonstrates a high degree of agreement with the experimental results for spherical particles. Simulated trajectories follow the experimentally observed paths, indicating that the model accurately captures the key dynamics of particle movement within the flow field. Dark blue lines representing the mean experimental trajectories provide a benchmark for assessing the model's accuracy. The red dashed lines, which represent the simulated trajectories, overlap significantly with the mean trajectories, further validating the model's precision. Close match between simulated and experimental trajectories for spherical particles indicates that the numerical model is capable for predicting particle transport in similar conditions. This reliability is important in order to extend model setup to more complex scenarios involving non-spherical particles. The accurate simulation of spherical particle trajectories represents another validation for the

effectiveness of the drag models implemented in the numerical simulations.

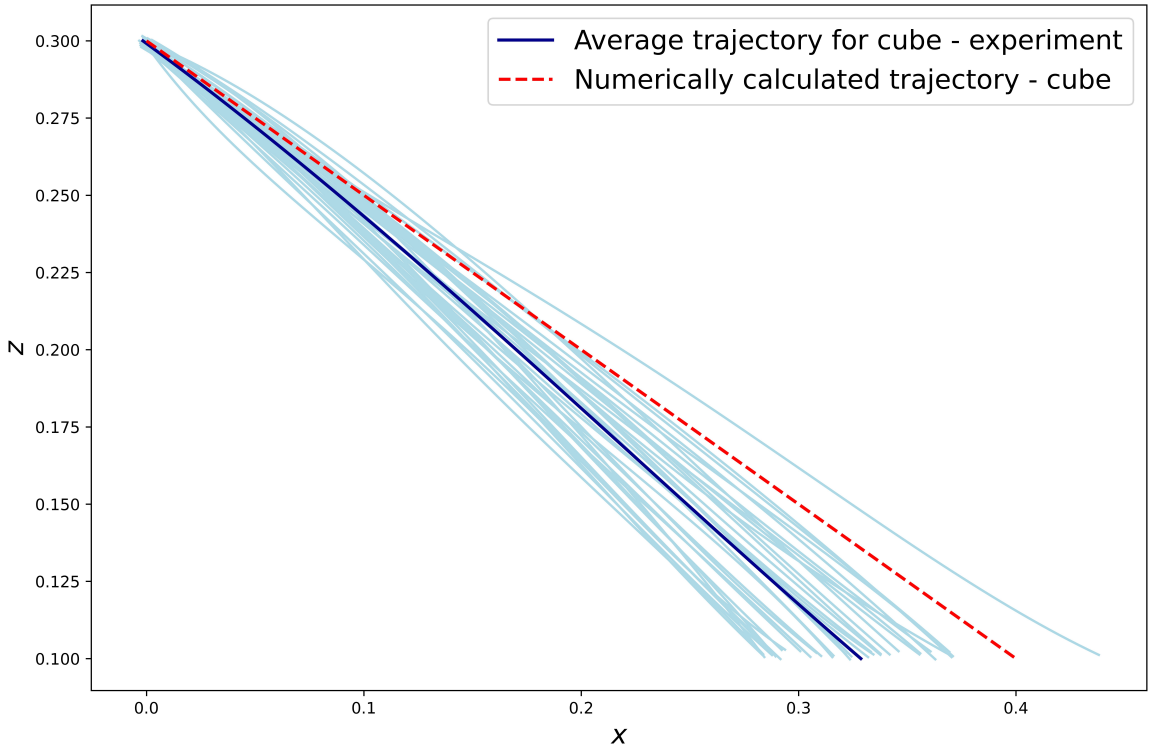

Figure 6.9: Graphical representation of MP particle trajectories for cube shape particles. Graph shows experimentally measured trajectories (light blue color), averaged experimental trajectories (dark blue) and numerically calculated trajectories (red dotted line).

For non-spherical particles, the comparison between simulation and experimental results reveals larger deviations. These discrepancies highlight the complexities involved in accurately modeling the behavior of irregularly shaped particles. Numerical simulations often predict longer trajectories for non-spherical particles than those observed in the experiments. Primary reason for these deviations can be attributed to the limitations of the *icoUncoupledKinematicParcelFoam* solver. One of these reasons is the way in which the shape of spherical bodies is given. Shape characteristics of non-spherical particles are defined in the model using the sphericity index, denoted as ϕ. In this study, a proposal for correcting the sphericity index is presented to improve the alignment between numerical simulation results and experimentally measured data. To adjust the sphericity index and enhance the accuracy of the model, a correction formula is proposed as follows:

$$\phi_{corr} = \phi^k. \tag{6.25}$$

In this equation, ϕ_{corr} represents the corrected value of the sphericity index, and k is the correction exponent. The iterative process of multiple numerical simulations yielded the optimal value for the correction exponent to be $k = 0.8$. Example of correction of sphericity index in numerical model for cube-shaped particles is given below.

```
constantProperties
{
    rho0            1185;
    youngsModulus   3e9;
    poissonsRatio   0.35;
}
subModels
{
    particleForces
    {
        nonSphereDrag
        {
            phi 0.842;
        }
        gravity;
    }
}
```

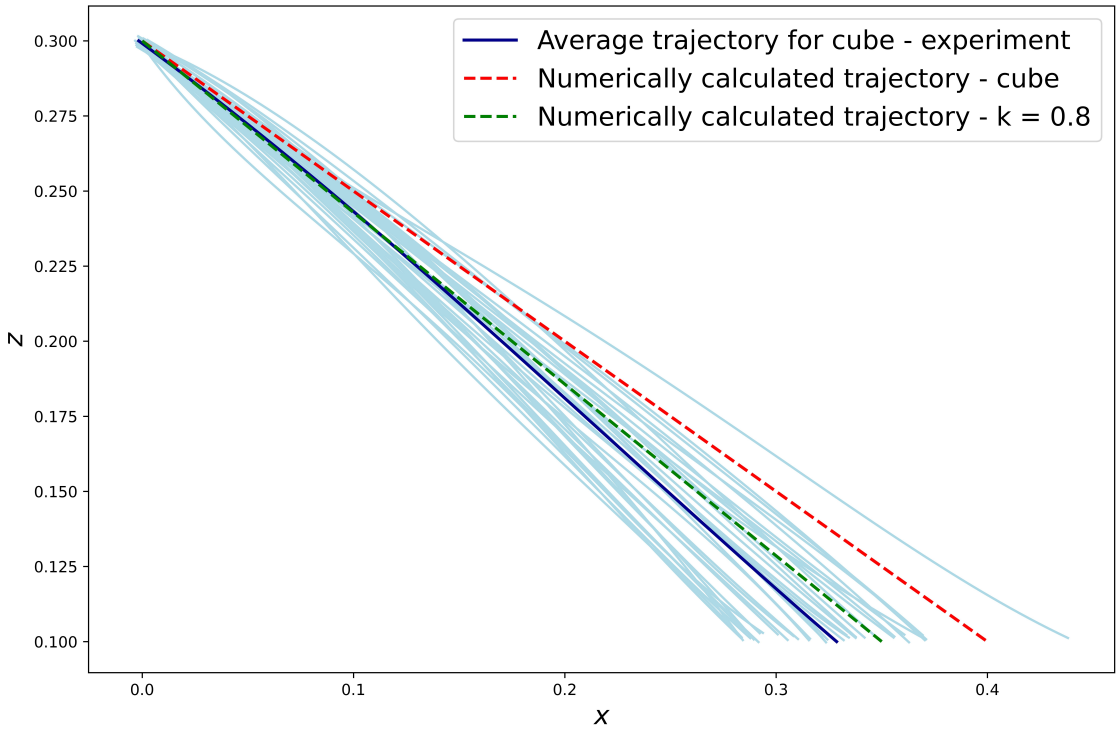

Figure 6.10: Comparison of average measured trajectory for cubic particle d_p = 3 mm (blue), initial numerical model result (dashed red), and corrected model result (dashed green).

Figure 6.10 illustrates the comparison of trajectories for a cubic particle with a diameter of d_p = 3 mm. The blue line represents the average measured trajectory from the experiments, the dashed red line shows the initial result from the numerical model, and the dashed green line presents the result from the model with the implemented sphericity index correction.

The model with the corrected sphericity index (ϕ_{corr}) describes the experimental results significantly better than the initial model. The corrected model's trajectories align more closely with the experimental data, indicating that the adjustment effectively accounts for the discrepancies observed in the initial simulations. By incorporating the corrected sphericity index, the numerical model's predictive capability can be improved. This adjustment allows for more accurate simulations of particle transport and deposition, particularly for non-spherical particles. Figure 6.11 and 6.12 demonstrates results for dodecahedron, icosahedron, octahedron and tetrahedron particles. The results show that for the corrected values of sphericity index, the numerically obtained trajectories agree better with the experimental values.

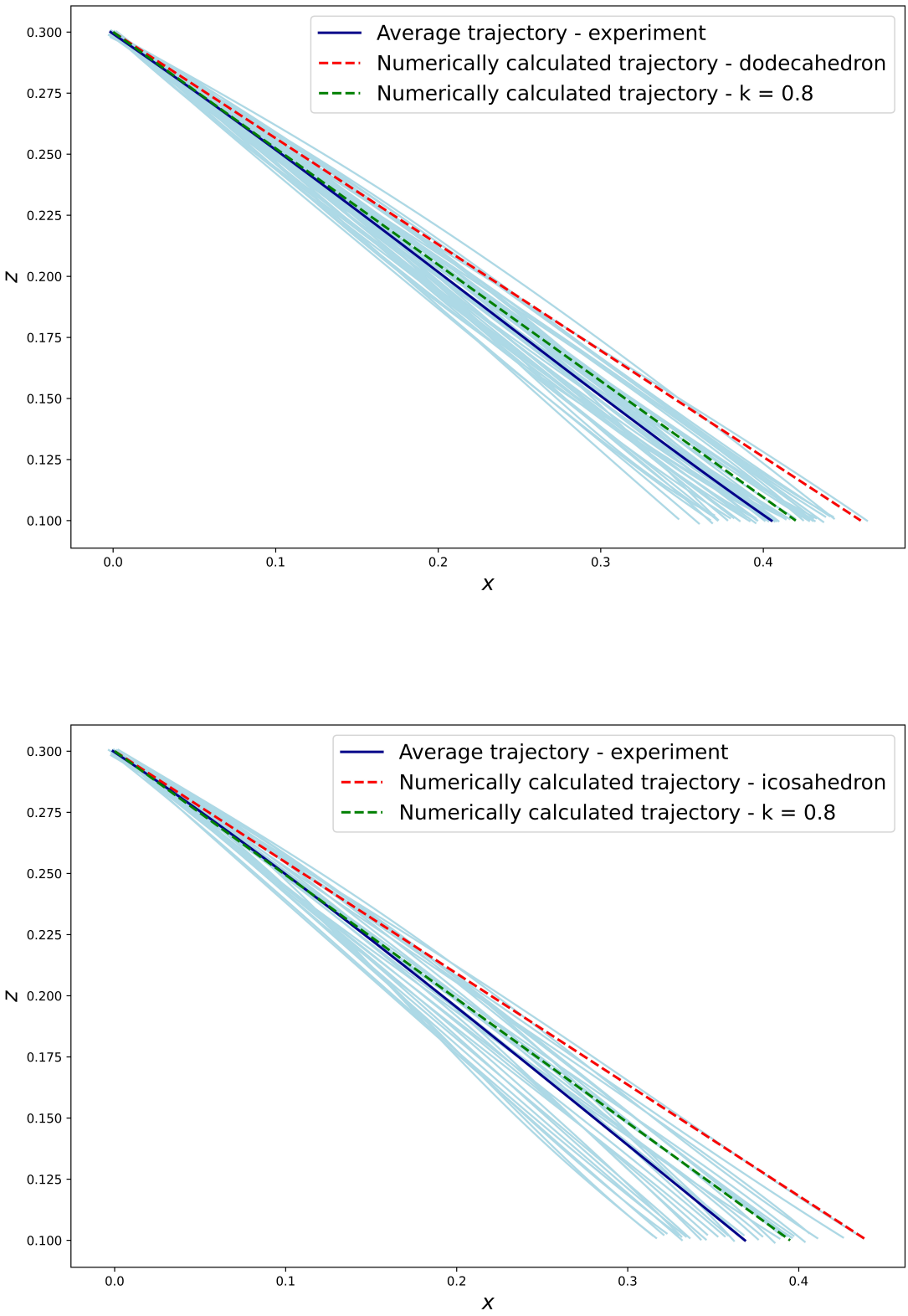

Figure 6.11: Comparison of average measured trajectory for dodecahedron (upper graph) and icosahedron (lower graph) particle $d_p = 3$ mm (blue), initial numerical model result (dashed red), and corrected model result (dashed green).

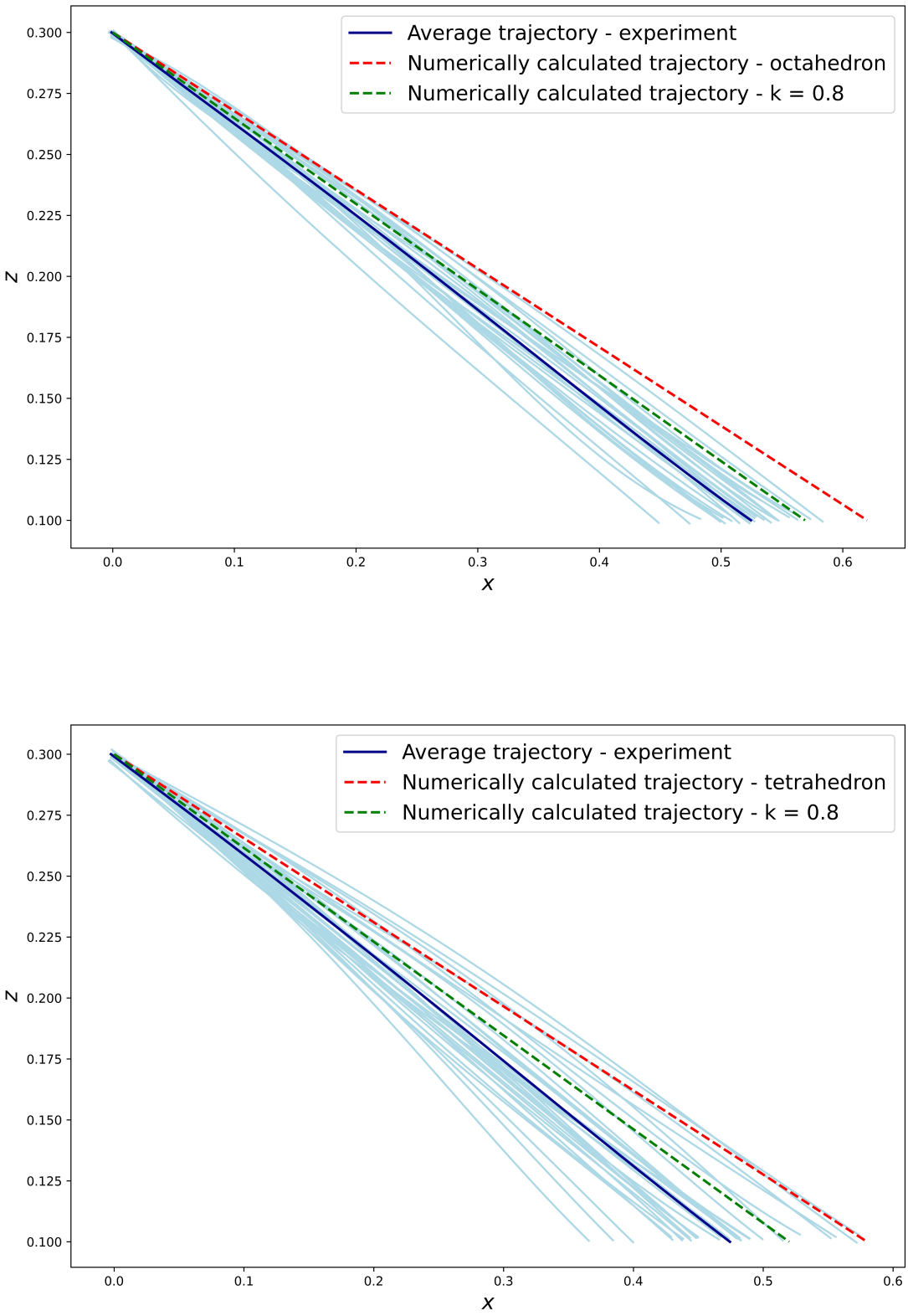

Figure 6.12: Comparison of average measured trajectory for octahedron (upper graph) and tetrahedron (lower graph) particle d_p = 3 mm (blue), initial numerical model result (dashed red), and corrected model result (dashed green).

The conducted numerical simulation demonstrated the potential of using the OpenFOAM software package for simulating the transport of microplastic (MP) particles, given the knowledge of flow conditions within the observed domain. In the simulation of spherical particles, the results showed good agreement with the experimental measurements. However, for simulations involving non-spherical particles, an additional correction for the shape coefficient is necessary to achieve accurate results with the OpenFOAM $nonSphereDrag$ model. This correction ensures that the drag forces and settling behaviors of non-spherical particles are represented with greater accuracy, thereby improving the reliability of the simulations.

By simulating particle transport, numerical models can identify critical zones where MP particles are likely to accumulate. This can be important information for environmental monitoring and management, as it helps pinpoint areas that may require targeted cleanup efforts. The use of numerical simulations significantly reduces the need for extensive and time-consuming experimental measurements. This efficiency allows researchers to conduct preliminary studies and hypothesis testing more rapidly and cost-effectively. With the known current field, the model can be adapted and applied to different water systems. This versatility makes it applicable to study MP pollution in diverse aquatic environments, from rivers and lakes to coastal and marine systems. Future research could focus on examining the interactions between MP particles themselves. Investigating these interactions could provide deeper insights into the aggregation and dispersion behaviors of MP in the aquatic environment. Additionally, comparing the capabilities of numerical simulations with experimental measurements of MP interactions could further validate and refine the model, upgrading its predictive accuracy and applicability.

7 Conclusion

The research presented in this thesis addresses the emergent environmental concern of MP pollution through a comprehensive experimental-numerical analysis of the transport of MP within aquatic systems. In the given resreach, by merging the experimental approach with state-of-the-art numerical simulations, relevant indications are provided regarding MP particle behavior: focusing on particle shape and hydrodynamic conditions. In other words, the key focus is the deeper understanding of the MP particle dynamics on drag coefficients and their transport mechanisms within water bodies under different flow conditions. This study was conducted in two main phases: experimental analysis and numerical simulations, each complementing the other to further improve understanding of MP behavior in aquatic environments.

The experiments were executed in a controlled environment using the hydraulic flume, which allowed for accurate measurement of water flow parameters and MP particle behavior. By using a high-speed video camera and applying OpenCV particle tracking techniques, detailed data on the velocity fields and trajectories of MP was provided. The high-precision 3D printer allowed for control of the geometry of particles and thus made a more detailed analysis of their kinematics possible. One of the main objectives was to quantify the drag forces acting on MP particles of different shapes in flowing water. The present study, therefore, considered Platonic solids - tetrahedron, cube, octahedron, dodecahedron, and icosahedron-representing a range from highly angular to a near - spherical particle shape-while detailed shape parameterization was carried out to also account for the more irregular geometries naturally occurring. Experimental results for spherical MP particles were compared against models well-known from the literature. This step of validation demonstrated the correctness of the experimental setup, and the methodology was extended further to other non-spherical shapes. In the process, shape-specific drag models were developed.

The numerical model was developed in continuation to the experimental work, where OpenFOAM software simulated MP particle transport, using flow conditions measured in the experimental flume. The numerical model was further validated against the experimental data for spherical particles with very good agreements. For non-spherical particles, model showed greater differentiation in the results in comparison to experiment. Thus, shape corrections for non-spherical particles were included in the model by tuning the sphericity index parameter to be representative of an irregular geometry. This adaptation allowed a more accurate simulation

of MP behavior under real conditions. Important part in this respect was the hybrid approach, where experimental measurements supported numerical simulations. During this process, numerical modeling could take advantage of the empirical data generated during these experiments for more accurate predictions of MP transport.

Application of the above combination of experimental-numerical approach resulted in the following conclusions: the experimental investigation provided a unique database of c_d-Re values for various MP shapes, serving as a reference for further investigations in both environmental and engineering perspectives, enabling more realistic modeling of MP transport within rivers, lakes, and marine systems. New drag model enables the estimation of the drag coefficient c_d with regard to the flow conditions represented by the Reynolds number, but also the geometrical characteristics of the particle represented by the corresponding shape parameter. The application of shape parameterization enables the application of this model to a wide range of MP particles in the environment. This is an important characteristic of the model due to the wide range of forms of MP in aquatic environments. Additionally, the experimental methodology used for the production of MP particles, as well as the setup for tests in flowing water, represents an upgrade compared to existing experimental methods. The use of OpenCV software for computer vision enables detailed tracking of the trajectory of each particle and the calculation and comparison of the drag coefficient c_d and Reynolds number per deposition depth. By experimentally testing various geometric shapes and applying multiple shape parameters, this study proposed a model that provides ability concerning particle drag force for MP with non-spherical shapes. Further, the study successfully combines experimental and numerical methodologies in analyzing MP transport. The integration of experimental data with numerical modeling represents a new approach in the study of MP transport. While many studies rely solely on numerical models or experimental data, this research combined both methods to develop a hybrid framework capable of simulating a wide range of real-world conditions. The synergy between empirical results and numerical simulations significantly improves the reliability and predictive power of the results. Finally, the findings from this research can be beneficiary in regards to environmental monitoring and clean-up efforts. Knowing where MP accumulate in water bodies may enable better targeted interventions.

Further research can be carried out in direction on how MP interacts with other forms of contamination, such as chemicals, heavy metals, or biological organisms. Understanding these interactions is important to assess the full environmental impact of MP. Furthermore, future de-

veloped models should also be applied under real conditions, like rivers, coasts, and estuaries, for further validation of the findings and to enable the study of more complex, large-scale MP transport phenomena. Additionally, further research could significantly benefit from exploring broader flow regimes. The current study primarily focuses on Re ranges where flow conditions are either laminar or transitioning to turbulence. However, many aquatic environments, especially those influenced by tidal forces, storm events, or strong river currents, exhibit highly turbulent conditions that were not fully explored in this work. Expanding the scope of research to include a wider range of Re values would offer a more comprehensive understanding of MP behavior in diverse real-world settings. Finally, MP particles are becoming increasingly common in aquatic environments, and their impact on marine organisms and ecosystems requires further study. The transport models developed during the present work could be used in combination with biological models in further studies, for the prediction of interaction between MP and aquatic species and ecosystems.

References

[1] Cfd - online - turbulence properties. Available online: https://https://www.cfd-online.com/Tools/turbulence.php. Accessed: 2023-07-05.

[2] OECD(2022). Available online: https://www.oecd.org/environment/global-plastic-waste-set-to-almost-triple-by-2060.htm. Accessed: 2022-05-12.

[3] Noelia Abascal-Zorrilla, Nicolas Huybrechts, Sylvain Orseau, Vincent Vantrepotte, Edward Anthony, and Antoine Gardel. Numerical investigation of the sediment load exchange between a coastal mud bank and its neighbouring estuary. *Water*, 16(20), 2024.

[4] Okpeafoh S. Agimelen, Peter Hamilton, Ian Haley, Alison Nordon, Massimiliano Vasile, Jan Sefcik, and Anthony J. Mulholland. Estimation of particle size distribution and aspect ratio of non-spherical particles from chord length distribution, 2014.

[5] Zeynep Akdogan and Basak Guven. Microplastics in the environment: A critical review of current understanding and identification of future research needs. *Environmental Pollution*, 254:113011, 2019.

[6] A. Alfaro-Nunez, D. Astorga, and L. Caceres-Farias. Microplastic pollution in seawater and marine organisms across the tropical eastern pacific and galápagos. *Sci Rep*, 12(3502), 2022.

[7] Asifa Ashrafy, Afroza Akter Liza, Md Nazrul Islam, Md Morsaline Billah, Shaikh Tareq Arafat, Md Moshiur Rahman, and Sheikh Mustafizur Rahman. Microplastics pollution: A brief review of its source and abundance in different aquatic ecosystems. *Journal of Hazardous Materials Advances*, 9:100215, 2023.

[8] Gholamhossein Bagheri and Costanza Bonadonna. On the drag of freely falling non-spherical particles. *Powder Technology*, 301:526–544, 2016.

[9] A. Ballent, S. Pando, A. Purser, M. F. Juliano, and L. Thomsen. Modelled transport of benthic marine microplastic pollution in the nazaré canyon. *Biogeosciences*, 10(12):7957–7970, 2013.

[10] Alfred Barnard Basset. Iii. on the motion of a sphere in a viscous liquid. *Philosophical Transactions of the Royal Society of London.(A.)*, (179):43–63, 1888.

[11] G. K. Batchelor. *An Introduction to Fluid Dynamics*. Cambridge Mathematical Library. Cambridge University Press, 2000.

[12] M. Bigdeli, A. Mohammadian, and A. Pilechi. Lagrangian modeling of marine microplastics fate and transport: The state of the science. *Journal of Marine Science and Engineering*, 2022.

[13] Mostafa Bigdeli, Abdolmajid Mohammadian, and Abolghasem Pilechi. A laboratory dataset on transport and deposition of spherical and cylindrical large microplastics for validation of numerical models. *Journal of Marine Science and Engineering*, 12(6), 2024.

[14] Cyrille Bonamy, Julien Chauchat, Zhen Cheng, Tim Nagel, and Tian-Jian Hsu. sedfoam, a openfoam solver for sediment transport. In *12th OpenFoam Workshop*, July 2017.

[15] Y.L. Chen and L. Zeng. A holistic model for microplastic dispersion in a free-surface wetland flow. *Journal of Cleaner Production*, 449:141806, 2024.

[16] R.P. Chhabra, L. Agarwal, and N.K. Sinha. Drag on non-spherical particles: an evaluation of available methods. *Powder Technology*, 101(3):288–295, 1999.

[17] R. Clift and W. H. Gauvin. Motion of entrained particles in gas streams. *The Canadian Journal of Chemical Engineering*, 49(4):439–448, 1971.

[18] R. Clift and W. H. Gauvin. Motion of entrained particles in gas streams. *The Canadian Journal of Chemical Engineering*, 49(4):439–448, 1971.

[19] Arthur Thomas Corey, Maurice L Albertson, Jess Lafayette Fults, Ralph L Rollins, Robert Alexander Gardner, Bruno Klinger, Robert O Bock, et al. Influence of shape on the fall velocity of sand grains. 1949.

[20] C.T. Crowe, J.D. Schwarzkopf, M. Sommerfeld, and Y. Tsuji. *Multiphase Flows with Droplets and Particles, Second Edition*. Taylor & Francis, 2011.

[21] Pierfrancesco Dellino, Daniela Mele, Rosanna Bonasia, Giuseppe Braia, Luigi La Volpe, and Roberto Sulpizio. The analysis of the influence of pumice shape on its terminal velocity. *Geophysical Research Letters*, 32(21), 2005.

[22] William E. Dietrich. Settling velocity of natural particles. *Water Resources Research*, 18(6):1615–1626, 1982.

[23] Fabio Dioguardi, Daniela Mele, and Pierfrancesco Dellino. A new one-equation model of fluid drag for irregularly shaped particles valid over a wide range of reynolds number: Aerodynamic drag of irregular particles. *Journal of Geophysical Research: Solid Earth*, 123, 12 2017.

[24] Morrison A. Faith. *An Introduction to Fluid Mechanics*. CAMBRIDGE UNIVERSITY PRESS, 2013.

[25] Zhi-Gang Feng and Efstathios E Michaelides. Drag coefficients of viscous spheres at intermediate and high reynolds numbers. *J. Fluids Eng.*, 123(4):841–849, 2001.

[26] OpenFOAM Foundation. Openfoam v2012 for windows 10, 2024. Accessed: 2024-08-27.

[27] Gary H. Ganser. A rational approach to drag prediction of spherical and nonspherical particles. *Powder Technology*, 77(2):143–152, 1993.

[28] Marcelo García. *Sedimentation engineering: processes, management, modeling, and practice*, volume 110. 01 2002.

[29] Franziska Greifzu, Christoph Kratzsch, Thomas Forgber, Friederike Lindner, and Rüdiger Schwarze. Assessment of particle-tracking models for dispersed particle-laden flows implemented in openfoam and ansys fluent. *Engineering Applications of Computational Fluid Mechanics*, 10(1):30–43, 2016.

[30] Mingqi Guo, Roohollah Noori, and Soroush Abolfathi. Microplastics in freshwater systems: Dynamic behaviour and transport processes. *Resources, Conservation and Recycling*, 205:107578, 2024.

[31] Thomas Hagemeier, Dominique Thévenin, and Thomas Richter. Settling of spherical particles in the transitional regime. *International Journal of Multiphase Flow*, 138:103589, 2021.

[32] BD Hardesty, J Harari, A Isobe, and L Lebreton. Using numerical model simulations to improve the understanding of micro-plastic distribution and pathways in the marine environment. *Frontiers in Marine Science*, 2017.

[33] Miloslav Hartman, Otakar Trnka, and Karel Svoboda. Free settling of nonspherical particles. *Industrial & Engineering Chemistry Research*, 33(8):1979–1983, 1994.

[34] R. Henniger, L. Kleiser, and E. Meiburg. Direct numerical simulations of particle transport in a model estuary. *Journal of Turbulence*, 11(45):1–28, 2010.

[35] Toni Holjević, Siniša Družeta, Luka Grbčić, and Marta Alvir. Empirical shape-based estimation of settling microplastic particles drag coefficient. *Journal of Marine Science and Engineering*, 11(11), 2023.

[36] Toni Holjević, Vanja Travaš, Siniša Družeta, and Danko Holjević. Experimental assessment of drag coefficient for quasi-radially-symmetric microplastic particles sinking in water stream. *Journal of Marine Science and Engineering*, 11(3), 2023.

[37] Alice A. Horton and Simon J. Dixon. Microplastics: An introduction to environmental transport processes. *WIREs Water*, 5(2):e1268, 2018.

[38] Chaoqun Ji, Jinfeng Zhang, Guangwei Liu, Qinghe Zhang, and Xiaoteng Shen. A settling velocity formula for irregular shaped microplastic fragments based on new shape factor: Influence of secondary motions. *Science of The Total Environment*, 955:176857, 2024.

[39] SK Karanfilian and TJ Kotas. Drag on a sphere in unsteady motion in a liquid at rest. *Journal of Fluid Mechanics*, 87(1):85–96, 1978.

[40] Liliya Khatmullina and Irina Chubarenko. Transport of marine microplastic particles: why is it so difficult to predict? 1. *Anthropocene Coasts*, 2:293–305, 09 2019.

[41] Liliya Khatmullina and Igor Isachenko. Settling velocity of microplastic particles of regular shapes. *Marine Pollution Bulletin*, 114(2):871–880, 2017.

[42] A. A. Koelmans, M. Siegfried, E. Besseling, and C. Kroeze. Export of microplastics from land to sea: A modelling approach. *Water Research*, 2017.

[43] Merel Kooi and Albert A. Koelmans. Simplifying microplastic via continuous probability distributions for size, shape, and density. *Environmental Science & Technology Letters*, 6(9):551–557, 2019.

[44] Nicole Kowalski, Aurelia M. Reichardt, and Joanna J. Waniek. Sinking rates of microplastics and potential implications of their alteration by physical, biological, and chemical factors. *Marine Pollution Bulletin*, 109(1):310–319, 2016.

[45] P.K. Kundu, I.M. Cohen, and D.R. Dowling. *Fluid Mechanics*. Science Direct e-books. Elsevier Science, 2012.

[46] Jingyi Li, Huihui Liu, and J. Paul Chen. Microplastics in freshwater systems: A review on occurrence, environmental effects, and methods for microplastics detection. *Water Research*, 137:362–374, 2018.

[47] Wei Liu, Twan van Hooff, Yuting An, Simon Hu, and Chun Chen. Modeling transient particle transport in transient indoor airflow by fast fluid dynamics with the markov chain method. *Building and Environment*, 186:107323, 2020.

[48] Magdalena Malankowska, Carlos Echaide-Gorriz, and Joaquin Coronas. Microplastics in marine environment: a review on sources, classification, and potential remediation by membrane technology. *Environ. Sci.: Water Res. Technol.*, 7:243–258, 2021.

[49] Martin R. Maxey and James J. Riley. Equation of motion for a small rigid sphere in a nonuniform flow. *The Physics of Fluids*, 26(4):883–889, 04 1983.

[50] A. S. Mountford. Eulerian modeling of the three-dimensional distribution of seven popular microplastic types in the global ocean. *Journal of Geophysical Research: Oceans*, 2019.

[51] F ODAR. Verification of the proposed equation for calculation of the forces on a sphere accelerating in a viscous fluid(determination of forces exerted by viscous fluid on sphere accelerating under gravity). 1966.

[52] CW Oseen. Neuere methoden und ergebnisse in der hydrodynamik, akad. *Verlagsgesellschaft, Leipzig*, 1927.

[53] T. Pfeiffer, A. Costa, and G. Macedonio. A model for the numerical simulation of tephra fall deposits. *Journal of Volcanology and Geothermal Research*, 140(4):273–294, 2005.

[54] Federico Pizzi, Mona Rahmani, Joan Grau, Francesco Capuano, and Lluís Jofre. Microparticle dynamics in upper-ocean turbulence: Dataset for analysis, modeling and prediction. *Data in Brief*, 56:110850, 2024.

[55] Maurice Cary Powers. A new roundness scale for sedimentary particles. *Journal of Sedimentary Research*, 23(2):117–119, 1953.

[56] Robert C Ramsdell, Sape A Miedema, and Arno M Talmon. Hydraulic transport of sand/shell mixtures. In *International Conference on Offshore Mechanics and Arctic Engineering*, volume 44380, pages 533–547, 2011.

[57] L. SCHILLER. A drag coefficient correlation. *Zeit. Ver. Deutsch. Ing.*, 77:318–320, 1933.

[58] YD Sobral, TF Oliveira, and FR Cunha. On the unsteady forces during the motion of a sedimenting particle. *Powder Technology*, 178(2):129–141, 2007.

[59] George Gabriel Stokes et al. On the effect of the internal friction of fluids on the motion of pendulums. 1851.

[60] B. Sumer and Jorgen Fredsoe. *The Mechanics of Scour in the Marine Environment*, volume 17. 04 2002.

[61] Hiraku Tanoiri, Haruka Nakano, Hisayuki Arakawa, Ricardo Shohei Hattori, and Masashi Yokota. Inclusion of shape parameters increases the accuracy of 3d models for microplastics mass quantification. *Marine Pollution Bulletin*, 171:112749, 2021.

[62] Vanja Travas, Lado Kranjcevic, Sinisa Druzeta, Toni Holjevic, Ivana Lucin, Marta Alvir, Luka Grbcic, and Ante Sikirica. Model gibanja čestica mikroplastike u nehomogenom i laminarnom polju brzine. *Hrvatske vode*, 29(117):201–213, 2021.

[63] P. Uzun and S. Farazande. Mathematical modeling of microplastic abundance, distribution, and transport in water environments: A review. *Chemosphere*, 2022.

[64] Michiel Van Melkebeke, Colin Janssen, and Steven De Meester. Characteristics and sinking behavior of typical microplastics including the potential effect of biofouling: Implications for remediation. *Environmental Science and Technology*, XXXX, 06 2020.

[65] Hakon Wadell. Sphericity and roundness of rock particles. *The Journal of Geology*, 41:310 – 331, 1933.

[66] Kryss Waldschlaeger and Holger Schüttrumpf. Effects of particle properties on the settling and rise velocities of microplastics in freshwater under laboratory conditions. *Environmental Science and Technology*, 53, 01 2019.

[67] Zhen Wang, Ming Dou, Pengju Ren, Bin Sun, Ruipeng Jia, and Yuze Zhou. Settling velocity of irregularly shaped microplastics under steady and dynamic flow conditions. *Environmental Science and Pollution Research*, 28:1–17, 11 2021.

[68] Weiming Wu, Wolfgang Rodi, and Thomas Wenka. 3d numerical modeling of flow and sediment transport in open channels. *Journal of Hydraulic Engineering*, 126(1):4–15, 2000.

[69] Zhengming Xu, Xianzhi Song, Gensheng Li, Zhaoyu Pang, and Zhaopeng Zhu. Settling behavior of non-spherical particles in power-law fluids: Experimental study and model development. *Particuology*, 46:30–39, 2019.

[70] Zijian Yu, Ge Yang, and Wenming Zhang. A new model for the terminal settling velocity of microplastics. *Marine Pollution Bulletin*, 176:113449, 2022.

[71] Song Zhiyao, Wu Tingting, Xu Fumin, and Li Ruijie. A simple formula for predicting settling velocity of sediment particles. *Water Science and Engineering*, 126, 03 2008.

[72] Shuang Zhou, Genguang Zhang, Xiaoyang Xu, and Chengming He. Experiments on the drag coefficient of a sphere with a variable velocity. *Water Supply*, 23, 04 2023.

List of figures

List of tables